

RUHR  
UNIVERSITÄT  
BOCHUM

RUB

# Plasma-Surface Synergism for Nitrogen Fixation

Dissertation

zur  
Erlangung des Grades  
„Doktor der Naturwissenschaften“

an der Fakultät für Physik und Astronomie  
der Ruhr-Universität Bochum

von  
**Steijn Vervloedt**  
aus Veldhoven

Bochum 2025



**1st Reviewer:**

**2nd Reviewer:**

**Date of defence:**

Prof. Dr. Achim von Keudell

Prof. Dr. Ir. Jean-Pierre H. van Helden

*to be announced*

# List of Abbreviations

<b>AC</b>	Alternating Current
<b>CCP</b>	Capacitively Coupled Plasma
<b>DBD</b>	Dielectric Barrier Discharge
<b>DC</b>	Direct Current
<b>DFT</b>	Density Function Theory
<b>DRIFTS</b>	Diffuse Reflectance Infrared Fourier Transform Spectroscopy
<b>DSR</b>	direct steam reforming
<b>EEDF</b>	Electron Energy Distribution Function
<b>EELS</b>	Electron Energy Loss Spectroscopy
<b>ER</b>	Eley-Rideal
<b>EY</b>	Energy yield
<b>FNS</b>	First Negative System of N <sub>2</sub>
<b>FTIR</b>	Fourier-Transform Infrared Spectroscopy
<b>FWHM</b>	full width at half maximum
<b>HB</b>	Haber-Bosch
<b>ICCD</b>	Intensified Charge-Coupled Device
<b>(M)IR</b>	(Mid-)Infrared
<b>IRRAS</b>	Infrared Reflection Absorption Spectroscopy
<b>LH</b>	Langmuir-Hinselwood
<b>LIF</b>	Light-Induced Fluorescence
<b>MCT</b>	Mercury Cadmium Telluride
<b>OES</b>	Optical Emission Spectroscopy
<b>ppm</b>	parts per million
<b>QCL</b>	Quantum Cascade Laser
<b>RF</b>	Radio Frequency
<b>SPS</b>	Second Positive System of N <sub>2</sub>
<b>VOC</b>	Volatile organic component
<b>ZDP</b>	Zero Distance Point
<b>XPS</b>	X-ray photoelectron spectroscopy
<b>μAPPJ</b>	micro atmospheric pressure plasma jet

# List of Molecules

$\text{CH}_4$	Methane
$\text{CO}$	Carbon monoxide
$\text{CO}(\text{NH}_2)_2$	Urea
$\text{CO}_2$	Carbon dioxide
$\text{Fe}_2\text{O}_3$	Iron(III) oxide
$\text{FeOOH}$	Iron oxyhydroxide
$\text{H}_2$	Hydrogen
$\text{H}_2\text{O}$	Water
$\text{HNO}_3$	Nitric acid
$\text{He}$	Helium
$\text{N}_2$	Nitrogen
$\text{NH}_3$	Ammonia
$\text{NH}_4\text{NO}_3$	Ammonium nitrate
$\text{NO}$	Nitric oxide
$\text{N}_2\text{O}$	Nitrous oxide
$\text{NO}_2$	Nitrogen dioxide
$\text{NO}_2^-$	Nitrite
$\text{NO}_3^-$	Nitrate
$-(\text{NO})_{1,2}$	Mono-, di-nitrosyl
$\text{O}_2$	Oxygen



# Contents

<b>List of Abbreviations</b>	<b>IV</b>
<b>List of Molecules</b>	<b>V</b>
<b>1 Introduction</b>	<b>1</b>
1.1 Context and Motivation . . . . .	1
1.2 Research questions . . . . .	5
1.3 Outline . . . . .	5
<b>2 Fundamentals</b>	<b>7</b>
2.1 Plasma Physics . . . . .	7
2.1.1 Capacitively Coupled RF Discharge . . . . .	7
2.1.2 Plasma Chemistry . . . . .	10
2.2 Infrared Absorption Spectroscopy . . . . .	15
2.2.1 Principles of Fourier-Transform IR Spectrometry . . . . .	15
2.2.2 Gas-Phase IR Absorption Spectra . . . . .	19
2.2.3 Infrared Reflection Absorption Spectroscopy . . . . .	21
2.3 Optical Emission Spectroscopy . . . . .	26
<b>3 Methodology</b>	<b>29</b>
3.1 Atmospheric Plug-Flow RF Plasma . . . . .	29
3.1.1 Power Measurements . . . . .	32
3.1.2 Ex-Situ FTIR Absorption Spectroscopy . . . . .	33
3.2 Low-Pressure Open RF Plasma . . . . .	35
3.2.1 IR Reflection Absorption Spectroscopy . . . . .	37
3.2.2 Pretreatment of Samples . . . . .	40
<b>4 Ammonia Synthesis in an Atmospheric RF Discharge</b>	<b>41</b>
4.1 Discharge Dynamics . . . . .	42
4.2 NH <sub>3</sub> Density Measurements . . . . .	46
4.3 Kinetic Model . . . . .	50
4.4 Discussion . . . . .	56
<b>5 Nitrogen Fixation in a Plasma-Exposed Surface Interface</b>	<b>59</b>
5.1 NO <sub>x</sub> Formation by N <sub>2</sub> +O <sub>2</sub> Plasma . . . . .	59
5.1.1 Pretreatment . . . . .	59
5.1.2 Identification of Reflection Spectra in 1:1 N <sub>2</sub> :O <sub>2</sub> . . . . .	62

---

5.1.3	Chemical Looping: $O_2 \longrightarrow N_2$ Cycle . . . . .	67
5.1.4	Parameter Study . . . . .	68
5.2	$NH_3$ Synthesis in $N_2+H_2$ Plasma . . . . .	71
5.2.1	Pretreatment . . . . .	71
5.2.2	Identification of Reflection Spectra in 1:3 $N_2:H_2$ . . . . .	72
5.3	Discussion . . . . .	76
<b>6</b>	<b>Conclusion and Outlook</b>	<b>79</b>
6.1	Conclusion . . . . .	79
6.2	Outlook . . . . .	80
<b>A</b>	<b>Chemistry set He/<math>N_2</math>/<math>H_2</math> plasma</b>	<b>82</b>
	<b>Bibliography</b>	<b>85</b>
	<b>Acknowledgements</b>	<b>99</b>

# Chapter 1

## Introduction

### 1.1 Context and Motivation

There is a broad consensus among scientists that climate change must be addressed immediately. The wide use of renewable energies can make our society more climate friendly. However, several hurdles have yet to be overcome.

Switching from a fossil fuel to a hydrogen ( $\text{H}_2$ ) economy will effectively cut carbon dioxide ( $\text{CO}_2$ ) emissions from several segments of our society [1]. Hydrogen can replace fossil fuels for transportation. This is especially true for the heavy-duty transportation (e.g. the maritime sector), where the low volumetric energy density is not of concern [2]. Beyond transportation, hydrogen is already widely used in industry. It is a reactant for ammonia and hydrocarbon production. In addition, it can make existing processes carbon neutral. For instance, iron ore can be reduced with  $\text{H}_2$  instead of coke [3]. This eliminates  $\text{CO}_2$  emission by producing water ( $\text{H}_2\text{O}$ ) instead.

#### $\text{N}_2$ fixation

Ammonia ( $\text{NH}_3$ ) could prove to be an effective energy-storage compound. It has distinct advantages over hydrogen: it does not need high-pressures to remain in liquid form, and it has a higher hydrogen and energy density than liquid  $\text{H}_2$ . This makes  $\text{NH}_3$  more suitable for both energy storage and long-distance energy transport [4]. For instance, Dunn et al. describe a thermochemical energy storage system based on  $\text{NH}_3$  [5]. The composition of the reservoir can be alternated between  $\text{NH}_3$  and  $\text{N}_2/\text{H}_2$ : the exothermic reaction  $\text{N}_2 + 3\text{H}_2 \longrightarrow 2\text{NH}_3$  releases energy, and the endothermic  $\text{NH}_3$  decomposition stores excess energy. The decomposition can be readily performed at elevated temperatures. Alternatively, plasmas can effectively dissociate  $\text{NH}_3$  using electricity, where full conversion to  $\text{H}_2$  is reported in literature [6].

In addition, nitrogen fixation is already a major segment of the chemical industry. This can be seen in the fact that 1.6% of the global energy consumption is spent on  $\text{NH}_3$  production, which mostly enters the artificial fertiliser production [7, 8]. Ammonium nitrate ( $\text{NH}_4\text{NO}_3$ ) and urea ( $\text{CO}(\text{NH}_2)_2$ ) are the most used forms of such fertilisers [9].

Ammonia is currently produced from  $\text{N}_2$  and  $\text{H}_2$  using the Haber-Bosch (HB) process. The overall process consists of (i) hydrogen production and (ii) ammonia production. Hydrogen is obtained from direct steam reforming (DSR) of methane ( $\text{CH}_4$ ):

$\text{CH}_4 + 2\text{H}_2\text{O} \longrightarrow \text{CO}_2 + 4\text{H}_2$  [8]. A high energy efficiency is obtained by using the heat released from the exothermic  $\text{NH}_3$  synthesis for the endothermic  $\text{H}_2$  production. This results in an energy cost close to the theoretical minimum of the overall reaction. Thus, it is very hard to compete with HB energy-wise.

The problem with HB are the  $\text{CO}_2$  emissions. This process alone is responsible for 1 to 2% of global emissions. Most of the  $\text{CO}_2$  is emitted as direct result of DSR, where it accounts for two-thirds of the emissions. Alternative processes for DSR could alleviate these emissions and make HB more climate friendly.

Methane pyrolysis or  $\text{H}_2\text{O}$  splitting are good alternatives to generate  $\text{H}_2$  without  $\text{CO}_2$  emissions. Pyrolysis produces solid carbon that has economic value, unlike  $\text{CO}_2$ . This makes the incorporation of  $\text{CH}_4$  pyrolysis already economically viable under some conditions [10]. However, it cannot be considered as a green process as it relies on fossil fuels. Water splitting by electrolysis is a green process, when the electricity from renewable sources is used [11]. It does not require any fossil fuels and can make use of the abundance of  $\text{H}_2\text{O}$ . Unfortunately, this technology still suffers from stability and durability issues, and high material and electricity costs.

However, interchanging DSR with pyrolysis or electrolysis does not adjust HB for the energy grid driven by renewable energy sources. HB is optimised for the centralised energy economy of today. Renewables will most likely produce energy very diffusely around the country. Solar panels should be installed on roofs, where ample space is available. Wind parks need to be strategically placed to minimise their impact on nature and people. They will decentralise the energy grid which pushes the need to decentralise the production of value-added chemicals as well [12]. In contrast, the high energy efficiency of HB is partially attributed to scaling up the reactor, since the energy efficiency scales with the size of the reactor [8]. Moreover, the fluctuation in the renewable energy supply brings another issue into consideration. Classical HB required continuous operation at high pressure and temperature that cannot easily be switched on or off. Thus, alternatives for the formation of  $\text{NH}_3$  from nitrogen and hydrogen need to be explored as well.

Therefore, the investigation for alternatives to produce ammonia is an interesting field of study. The new processes need to solve the issue of  $\text{CO}_2$  emissions as well as dealing with the decentralisation and varying energy supply.

### Plasma-based $\text{N}_2$ fixation

Plasmas are a good alternative to make our economy climate-friendly. They create a very chemically active environment that can overcome the strong binding energy of  $\text{N}_2$ . They can be easily switched on and off, since they rely on electricity and operate at moderate pressures and temperature. Many experiments are performed at smaller scales and show promising results, e.g. the earlier mentioned  $\text{NH}_3$  plasma-based decomposition [6]. Therefore, plasma-based gas conversion can complement the energy grid envisioned for the future.

Plasma-based pilot projects are already operational. For instance, a microwave methane pyrolysis test plant is operational in Austria [13]. It is connected to a 1 MW solar photovoltaic plant. The produced  $\text{H}_2$  is used as energy storage and can supply households with heating and electricity. The carbon black is sold for soil enhancement purposes [14]. A similar business model can be applied for nitrogen fixation.

In addition, plasmas could be combined with other techniques such as electrolysis. Sharma et al. combined a  $N_2$  plasma with an electrochemical cell that produces  $H_2$  [15]. The activated nitrogen species react with hydrogen at the platinum anode of an electrochemical cell. Although their plasma was operated at low pressure, it showed that plasmas can be coupled to electrolysis. These processes could complement each other to mitigate their respective disadvantages, instead of competing with each other.

Nonetheless, it is very difficult for plasma-based technologies to compete with HB, since HB has very high energy efficiencies as mentioned before. Alternatively, in the production of nitrogen-based fertilisers, the need for ammonia might be reduced by exploring alternative chemical pathways.

An  $N_2/O_2$  plasma can directly produce nitrogen dioxide ( $NO_2$ ), similar to the Birkeland-Eyde process [16]. This could be an alternative pathway to produce nitric acid ( $HNO_3$ ), which is an important reactant for  $NH_4NO_3$  production [17]. Currently,  $HNO_3$  is produced by the Ostwald process using  $NH_3$  from HB. The Ostwald process oxidises ammonia to  $HNO_3$  in two steps: by reacting  $NH_3$  with  $O_2$  to  $NO_2$ , and  $NO_2$  with  $H_2O$  to  $HNO_3$ . The first step can be cut when using plasma-based nitrogen oxidation. This reduces the need for ammonia and thereby that for fossil fuels as well. Thus, plasma-based nitrogen oxidation is an interesting field of research.

### State-of-the-art plasma-based $N_2$ fixation

Many different plasma reactors have been explored for  $NH_3$  synthesis [18]. Dielectric barrier discharges (DBD) emerged with the highest yield and energy efficiency [19]. Thus, they constitute as the most suitable plasma reactor. The short lifetime of the filamentary discharges are characterised by high electric fields [20]. This makes them ideal for nitrogen splitting, while limiting the destruction of ammonia. Also, the close proximity of the plasma to the surface stimulates the hydrogenation of nitrogen atoms over the surface. Surface reactions are proposed to play a vital role in ammonia formation. Therefore, many studies investigated the impact of various surfaces on the ammonia formation [21–23]. This is typically referred to as plasma catalysis. Catalytic materials could synergise with plasmas to open-up chemically more favourable pathways [24].

However, the proposed significant improvement by combining plasmas with catalysis has yet to be experimentally verified. It is challenging to understand the precise effect a catalyst has on  $NH_3$  synthesis due to the complex nature of DBD plasmas. The ignition is strongly related to the charge build up of previous cycles [20], which is material dependent. Hence, some studies found a strong relation between the catalyst material and the plasma dynamics [23, 25]. Consequently, it is difficult to identify which process stimulates ammonia synthesis, e.g. the plasma performance or the actual catalytic reactions on the surface. To study potential catalytic reactions, the plasma operation should be separated from the surface composition. The results of such an experiment are discussed in chapter 4.  $NH_3$  synthesis is studied in a  $He/N_2/H_2$  radio frequency (RF) discharge. The gas breakdown of this discharge is not related to the surface-related effects, such as charge storage as seen with DBDs. The impact of the surface on the chemistry is optimised by increasing the surface-to-volume ratio. A small amount of  $N_2$  and  $H_2$  is admixed to a helium gas stream such that the discharge behaves as a typical and well-studied helium plasma, which greatly simplifies the plasma

chemistry.

The plasma dynamics in the gas phase are well understood by now. The kinetics of pure  $N_2$  plasmas are studied in great detail by combining detailed emission spectra with kinetic models to map-out the electron impact reactions with nitrogen [26–28]. The  $N_2/H_2$  and  $N_2/O_2$  plasma gas kinetics are well understood [29–33]. Thus, literature presents a clear picture of  $NH_3$  and  $NO_x$  formation in the gas phase.

### Plasma-Surface interactions

However, the surface-plasma interactions are not well understood. Current models incorporate surface reactions from heterogeneous catalysis. There, stable molecules are applied to a well defined surface at elevated temperatures. This is completely different for plasma-exposed surfaces. Plasmas introduce radicals and electronically and vibrationally excited species to the surface. These are suggested to lower or completely remove reaction barriers [24, 34]. But, they lower or remove the barriers for reverse reactions as well [35]. This is problematic as it counters the suggested positive impact of a plasma on the surface chemistry. Therefore, a clear and concise description of the plasma-induced surface chemistry should be obtained.

Other applications such as the semiconductor industry also provide a valid reason for studying the impact of  $N_2/H_2$  plasma exposure on a metallic substrate. High quality metal films can be produced by treating a metallic precursor with a  $NH_3$  or  $N_2/H_2$  plasma. Vos et al. found that the  $NH_x$  radicals are essential in removing the precursor from cobalt to produce a high quality thin cobalt film [36]. It gives us another reason to study the  $N_2/H_2$  chemistry.

The surface chemistry can be experimentally studied with infrared reflection absorption spectroscopy (IRRAS) [37, 38]. It is a versatile and non-intrusive diagnostic to measure the surface composition. Various vibrational modes of atoms and molecules are probed with the IR-light that is reflected on the surface.

The oxidation of nitrogen is a well studied process with ample literature sources [39–43]. The detailed and well documented spectral positions of various nitrogen oxides makes it an ideal system to be studied in a plasma system. The adsorption of nitric oxide (NO) on an iron surface forms mono-nitrosyl Fe-(NO), di-nitrosyl Fe-(NO)<sub>2</sub>, and NO<sup>+</sup> [39]. If oxygen is added before or during NO adsorption, then nitrates are readily formed [39, 40]. These measurements were all performed at low pressure and at different temperatures, i.e. the surface only interacted with stable molecules. In contrast, this is much different for surface under plasma exposure. The great multitude of different radicals will react with the surface that is much faster than the stable molecules. Therefore, it is interesting to study how comparable the nitrogen oxidation on a plasma exposed surface is to thermal oxidation.

## 1.2 Research questions

The main topic of this thesis is to study how surfaces impact the plasma-based nitrogen fixation. This falls under the umbrella of plasma catalysis, where plasmas are combined with catalysts to enhance conversion and selectivity. The topic is pursued by two complementary research goals.

- *Identify the impact of a catalytic coating on  $\text{NH}_3$  formation.*

This goal focusses on investigating the impact of the plasma catalytic conversion of  $\text{N}_2$  and  $\text{H}_2$  to  $\text{NH}_3$ . Experiments are compared to a chemistry model to understand the underlying mechanisms governing  $\text{NH}_3$  synthesis. The following research questions are posed to tackle this problem:

1. What are the key mechanisms and limiting reactions for  $\text{NH}_3$  synthesis?
2. How does the catalytic coating affect the  $\text{NH}_3$  synthesis?

- *Characterise nitrogen fixation at a plasma-surface interface.*

The surface chemistry under plasma exposure is poorly understood, unlike the well-studied composition under thermal equilibrium. The surface composition is studied *operando* with IRRAS during operation with  $\text{N}_2+\text{O}_2$  and  $\text{N}_2+\text{H}_2$  plasmas. A consistent and reproducible measurement procedure must be developed, before nitrogen fixation can be studied. The experiments should be carefully compared with literature when answering the following questions:

1. Which surface-bound species are formed as a result of direct plasma exposure?
2. How are these adsorbed species formed?

Answering these questions will help in achieving the two research goals that enable to improve the description of the chemistry in a plasma-catalytic reactor.

## 1.3 Outline

The most relevant aspects of plasma physics will be presented in chapter 2. A theoretical background on IR absorption and optical emission spectroscopy is given as well. This sets the stage to present the two experimental setups in chapter 3. These setups are designed to tackle the research goals, and are presented separately. The layout and measurement procedure of each setup are described.

Ammonia synthesis in an atmospheric helium RF discharge with a small admixture of  $\text{N}_2$  and  $\text{H}_2$  is investigated in chapter 4. The discharge parameters are examined first by means of optical emission spectroscopy and the power-to-voltage curves. Second, the ammonia synthesis experiments are presented.  $\text{NH}_3$  production as a function of gas mixture and discharge power is discussed. The impact of plasma catalysis is studied by comparing uncoated with surface-coated experiments. Third, these results are combined with a chemistry model to explore the underlying reactions that are responsible

for  $\text{NH}_3$  formation. This chapter ends with a discussion on the impact of the surface morphology on the  $\text{NH}_3$  synthesis process.

The surface composition is directly investigated using IRRAS in chapter 5. The nitrogen oxidation on a substrate under plasma exposure is examined in a  $\text{N}_2/\text{O}_2$  gas mixture. The spectral components in the mid-IR (MIR) regime are identified and compared to literature. The gas ratio variation informs us about the relation between the gaseous plasma products and the substrate composition. In addition,  $\text{NH}_3$  production over the surface is studied in a  $\text{N}_2/\text{H}_2$  gas mixture following the methods used in the  $\text{N}_2/\text{O}_2$  experiments. Finally, the results are compared with literature.

The thesis ends with a conclusion and an outlook in chapter 6. The aforementioned research goals are addressed using the results from the two results chapters. Afterwards, possible future research endeavours are proposed based on the outcomes of this thesis.

# Chapter 2

## Fundamentals

The experiments presented in this thesis focussed on unravelling mechanisms in a plasma-catalytic system. First, the most important aspects of the discharge type used in this thesis are discussed, e.g. the plasma chemistry. Afterwards, the fundamentals behind the optical diagnostics used in the experiments are discussed. This is divided in two parts: IR absorption spectroscopy on the gas and surface phase and optical emission spectroscopy.

### 2.1 Plasma Physics

Capacitively coupled plasmas (CCP) are widely applied in both industry and academic studies. Two different plasmas are used in this thesis, but both are based on the CCP design. In chapter 4, an atmospheric RF helium plasma is used to investigate  $\text{NH}_3$  synthesis. In chapter 5, a more classical CCP at 8 mbar is used to investigate the plasma-surface interface. In the upcoming subsections, the most important aspects for both plasmas are discussed.

#### 2.1.1 Capacitively Coupled RF Discharge

The plasma frequency of electrons and ions set the timescale at which these species respond to the electric field [44]. They follow equation 2.1, which is derived for single ionisation (only  $\text{A} + \text{e} \longrightarrow \text{A}^+ + 2\text{e}$ ). It depends on the electron density  $n_e$ , ion density  $n_i$ , electron mass  $m_e$ , ion mass  $M_i$ , and physical constants such as the electron charge  $e$  and the vacuum permittivity  $\epsilon_0$ .

$$\omega_{pe}^2 = \frac{e^2 n_e}{\epsilon_0 m_e}, \quad \omega_{pi}^2 = \frac{e^2 n_i}{\epsilon_0 M_i} \quad (2.1)$$

Capacitively coupled plasmas are driven by an alternating current (AC) voltage. The driving frequency  $\omega$  is higher than the ion plasma frequency but smaller than the electron plasma frequency. Thus, ions respond to the time-averaged electric potential whereas the electrons respond instantaneously.

The following simplifications are considered to gain understanding in the complexity of the plasma: 1) the parallel placed electrodes are assumed to be much larger than the gas gap distance so that effects near the edges of the electrodes may be omitted;

2) the electron density in the plasma sheath is set to zero. This holds if the electron temperature is lower than the voltage drop over the sheath, so that the electrons are contained inside the plasma; 3) the ion density is constant across the entire gas gap. These simplifications give us the homogeneous model that is used to derive the components of the equivalent electrical circuit. Dropping the third simplification is useful when estimating scaling laws of the current density, heating mechanisms, and sheath thickness with the absorbed power by the plasma.

### Equivalent electrical circuit

The impedance of the plasma bulk  $Z_p$  is derived from the response of the electrons to the applied electric field [44]. The response of the electrons to the driving voltage signal has an inductive and ohmic response. They are characterised by the induction  $L_p = 1/C_0\omega_{pe}^2$  and ohmic resistance  $R_p = \nu_m L_p$ . The electron-neutral collision frequency  $\nu_m$  dictates the momentum transfer from the accelerated electrons to the background gas and increases with pressure. The capacitance of the gas gap  $C_0 = \epsilon_0 A/d$  is parallel to RL-branch. This yields the equivalent circuit of the plasma bulk illustrated in figure 2.1.

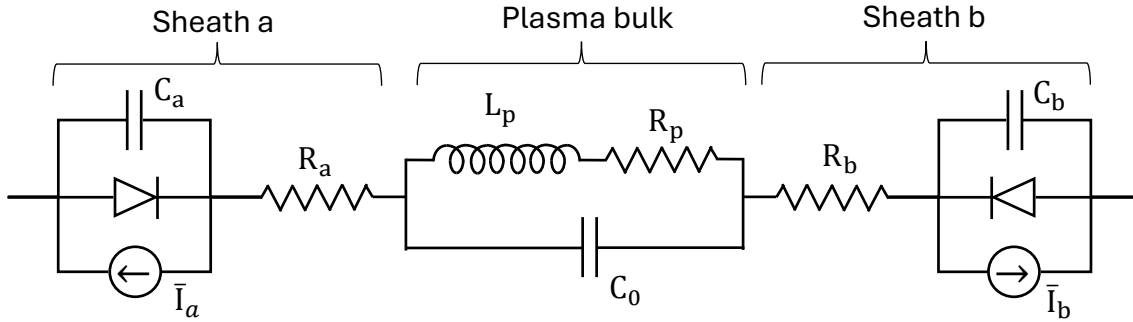


Figure 2.1: The equivalent electrical circuit of a capacitively coupled plasma.

The plasma sheaths  $a$  and  $b$  are characterised by the capacitances  $C_a$  and  $C_b$  for sheath thickness  $s_a$  and  $s_b$ , ion flux towards the walls, and the electron flux towards the plasma. The sheath thicknesses oscillate in time following the driving voltage. The ion flux to the walls results in secondary electron emission that produces the electron flux back to the plasma. This is indicated using the diode-symbol. Stochastic heating introduces the resistances  $R_a$  and  $R_b$ . It originates from the electrons reflecting from the oscillating electric field. These values are a function of the amplitude of the driving voltage, which is expressed as the root-mean square voltage  $V_{rms}$ . The scaling laws can be approximated using the inhomogeneous model, when the third simplification is omitted.

The plasma power  $P_p$  is calculated from the time averaged energy absorption per RF cycle times the driving frequency  $f_{RF}=13.56$  MHz as described in equation 2.2. The current running through the plasma is related to the applied voltage following the total impedance the plasma bulk and sheaths:  $Z_{tot} = |Z_{tot}|e^{-i\varphi}$ .

$$\begin{aligned}
V_{RF}(t) &= \sqrt{2}V_{rms} \cos(2\pi f_{rf}t) \\
I_{RF}(t) &= V_{RF}/Z_{tot} = \sqrt{2}V_{rms}|Z_{tot}| \cos(2\pi f_{rf}t - \varphi) \\
P_p(t) &= f_{RF} \int_0^{1/f_{rf}} V_{RF}(t)I_{RF}(t)dt = |Z_{tot}|V_{rms}^2 \cos \varphi
\end{aligned} \tag{2.2}$$

The ohmic heating is negligible compared to stochastic heating at lower pressures, hence both parts of the plasma must be considered. When the plasma density is low, the phase difference  $\varphi$  approximates  $\pi/2$ . The resistive components from the ohmic and stochastic heating will lower  $\varphi$  such that the power becomes non-zero.

### Gas breakdown

The breakdown for a direct current (DC) plasma is described by the Paschen curve [44]. Ions bombarding the cathode generate secondary electrons serve as seed electrons. These electrons accelerate and cause ionisation in the gas gap when moving towards the anode. To sustain the discharge, the electrons should cause sufficient ionisation such that the ion flux towards the cathode creates enough secondary electrons. For a given gas mixture and cathode material, the breakdown voltage is only a function of the pressure times electrode distance  $pd$ .

The physics is more complex when discussing an AC discharge [45, 46]. The oscillating electric field does not energise the electrons enough that ionisation can occur. Rather, the electrons should gain sufficient kinetic energy perpendicular to the direction of the electric field to ionise the neutrals. This is often referred to as random energy, since it is acquired by elastic collisions with neutrals. The discharge will be sustained once enough electrons are generated to overcome the losses at the walls. This yields the ignition condition:  $\nu_i = D_e/\Lambda^2$ . The ionisation frequency  $\nu_i$  equals the electron diffusion to the walls, which is characterised by the electron diffusion constant  $D_e$  and characteristic diffusion length  $\Lambda$ .

The breakdown voltage is characterised by two parameters:  $p\Lambda$  and  $p\lambda$ . The former is very similar to the  $pd$  parameter seen in the DC case. The latter considers the frequency of the electric field, where  $\lambda$  is the corresponding wavelength. In the MHz-range, Park et al. found that the breakdown voltage rapidly increases below 8 MHz for an helium plasma at near-atmospheric pressure [47].

### Secondary electron emission

The secondary electron emission coefficient  $\gamma_{se}$  lowers the required breakdown voltage. It lowers the net electron flux towards the walls, which improves the confinement of the electrons to the discharge. To sustain the discharge, a given amount of ionisation needs to occur. When  $\gamma_{se}$  increases, the electron temperature (or reduced electric field) can be lowered.

An ion impinging on the surface neutralises with an electron of the solid [44]. The neutralisation can produce an electronically excited particle. This state can relax and release a photon, which is called recombination radiation. Alternatively, the impinging ion is neutralised and excess energy is given to a secondary electron that escapes the

surface. This is called Auger emission. It occurs when the freed electron moves in the right direction and the ionisation potential of the incoming ion  $\varepsilon_i$  is greater than twice the work function  $\varepsilon_\phi$ , such that the neutralisation released enough energy to emit a secondary electron.

Auger neutralisation is independent of the kinetic energy, thus it is referred to as potential electron emission as well [48]. It is dominant for ions with a kinetic energy up to 500 eV. Above this energy, kinetic electron emission contributes as well to the overall  $\gamma_{se}$ , but such energies are rarely obtained in our case.

Secondary electrons can also be generated by impinging metastable atoms [49]. An electron can be emitted if the potential energy stored in the electronic excitation  $\varepsilon_m$  of the metastable is greater than the work function. The energy threshold ( $\varepsilon_m > \varepsilon_\phi$ ) is lower than for Auger emission, where  $\varepsilon_i > 2\varepsilon_\phi$ . This process likely dominates over Auger emission for atmospheric helium discharges, since the helium metastable density is typically an order of magnitude higher than the helium ions [50].

Although metals have a lower work function than metal oxides,  $\gamma_{se}$  is higher for the latter [51–53]. The work function determines the escape probability of secondary electrons, but the electron generation and transport towards the surface must be considered as well. Fewer electrons are available in a metal oxide. The energy dissipated to the surface creates more energetic electrons on average. Also, the electron-electron collisions are less prone to dissipate the energy of the freed electrons back into the surface. Thus, the  $\gamma_{se}$  is higher for most metal oxides (i.e. dielectrics) than for pure metals.

### 2.1.2 Plasma Chemistry

The continuity equation describes the particle density  $n_M$  in  $\text{m}^{-3}$  in time and space following the particle flux  $n_M \vec{v}_M$  and the net production term  $R_M$ . It produces the particle balance equation 2.3 that is needed to describe the plasma chemistry,

$$\frac{\partial n_M}{\partial t} + \nabla \cdot (n_M \vec{v}_M) = R_M \quad (2.3)$$

The reactions in the gas phase are either two- or three-body reactions. The rate coefficient for these reactions is in  $\text{m}^{-3} \text{s}^{-1}$  and  $\text{m}^{-6} \text{s}^{-1}$ , respectively. The latter is progressively more important with increasing pressure.

The surface density  $S_M$  in  $\text{m}^{-2}$  of an adsorbed species  $M$  is derived from such an equation. However, it does not propagate through the reactor as there is no significant particle flux on the surface in the direction of the gas flow. Thus, the continuity equation 2.3 simplifies to,

$$\frac{\partial S_M}{\partial t} = R_{surf,M}(x, t) \quad (2.4)$$

### Electron Excitation

Electron impact reactions are the driving force of the plasma chemistry. Elastic collisions lead directly to gas heating. This process is described by the short-range polarisation scattering of charged particles with neutrals, i.e. elastic collisions of electrons with the cold background gas. The cross section depends on the relative polarisation.

This coefficient is very low for helium, compared to other atoms and molecules. Therefore, electrons can travel much further in a pure helium atmosphere than in other gas mixtures.

Inelastic collisions are key in creating the non-equilibrium of which plasmas are renown for. The rate coefficient  $k_e$  in  $\text{cm}^{-3}\text{s}^{-1}$  of an electron inelastically colliding with a particle is calculated from the electron energy distribution function (EEDF)  $f(\varepsilon)$  and the cross-section  $\sigma(\varepsilon)$ , see equation 2.5. The cross section is unique for every reaction and is obtained from the LxCat database [54–56].

$$k_{e-\text{impact}} = \int_0^{\infty} \sigma(\varepsilon)f(\varepsilon)d\varepsilon \quad (2.5)$$

The normalised power absorption  $P_{abs}$  towards the available channels in an atmospheric helium plasma are presented in figure 2.2a. The EEDF is calculated with the LokiB Boltzmann solver [57, 58] for an atmospheric helium RF plasma with  $T_{gas}=300\text{ K}$  and  $n_e=10^{11}\text{ cm}^{-3}$ . These conditions describe the discharge of chapter 4 as well as similar discharges, e.g. COST-jet [59, 60].

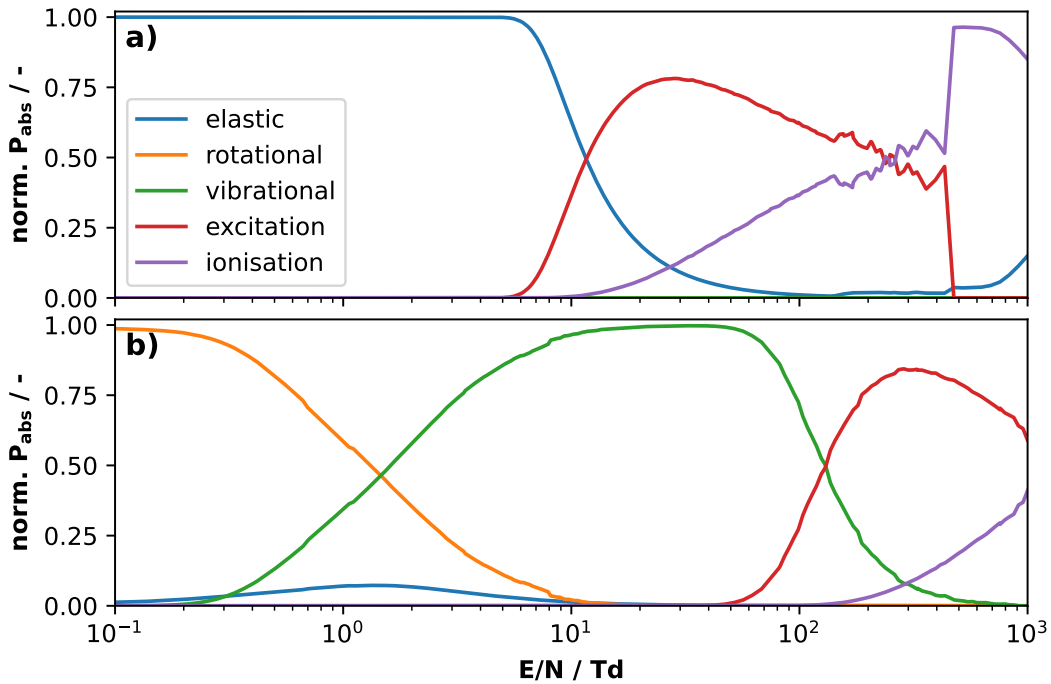


Figure 2.2: The normalised power absorption for different channels of an atmospheric He (a) and  $\text{N}_2$  (b) RF plasma as function of  $E/N$  calculated with LokiB using the IST-LisBon reaction set [54].

Helium can only electronically excite or ionise. These channels have a high energy threshold, where the first electronically excited state is 19.8 eV above the ground state. A reduced electric field higher than 10 Td is needed to shift the main electron power loss channel from elastic to electronic excitation for an atmospheric plasma in figure 2.2a. The energy threshold is much higher than with other noble gases and molecules. It pushes the discharge towards higher  $E/N$  values and lower electron densities. Any

minor impurity will have a significant impact on the electron power deposition, because every other species requires less energy than helium to electronically (or otherwise) excite [61].

Nitrogen is a diatomic molecule that can rotate and vibrate. This increases the number of channels in which electrons can deposit energy through inelastic collisions. The normalised power absorption per channel for an atmospheric  $N_2$  RF plasma is plotted in figure 2.2b, which uses the same conditions as the helium discharge of figure 2.2a. Note that these conditions are not realistic for an atmospheric  $N_2$  discharge. The gas temperature will certainly be higher than 300 K. The rotational mode readily equilibrates with the gas temperature, which leads to significant gas heating. This also applies to the vibrational mode, but to a lesser extent. Nonetheless, it presents a conclusive overview on how the power absorption of a molecule differs from a noble gas plasma.

## Surface reactions

Surface reactions play an important role in plasma catalytic reactions. Fragmentation, sputtering, and implantation require high kinetic energies of at least 10, 100, and 1000 eV, respectively [44]. Such high energies are more effectively achieved by ions at sub-pascal pressures. The mean-free path is higher such that ions can gain sufficient kinetic energy when applying a bias voltage on the surface.

Surfaces, i.e. substrates, can be physically cleaned using sputtering. It requires heavy ions to stimulate effective momentum transfer to the surface. Argon ions are widely used since it is readily available and its atomic number is close to the typical target atoms, e.g. nickel and copper [52]. It has the advantage over chemical cleaning that no new chemical bonds are formed.

Low-energy processes such as adsorption and desorption are more relevant for plasma-catalysis [44]. The adsorption and binding through the van der Waals force results in physisorption. This is a weak binding configuration. Chemisorption is the process where species form chemical bonds with the surface, which results in a much higher binding energy. Desorption requires the species to overcome the binding energy. Chemisorbed species also need to overcome an activation energy barrier as well.

Physisorption may be neglected in our case. The binding energy for physisorbed species is much lower than of chemisorbed species. The weak-binding energies of physisorption is too low to contain the species to the surfaces for temperatures above 300 K [30]. This condition is readily met when the surface is exposed to a plasma. Therefore, in the upcoming discussion, only chemisorption and desorption of chemisorbed states will be discussed.

The surface chemistry is presented using the Eley-Rideal (ER) and Langmuir-Hinselwood (LH) mechanisms [62]. The former is used to describe the interaction of volumetric species with a surface-bound species. The LH mechanism describes how two reactants adsorb and react with each other over the surface.

The ER reaction rate  $K_{ER}$  in  $s^{-1}$  is derived from the interaction time of a gas phase species with the surface, see equation 2.6 [31, 44]. It considers the diffusion to the walls  $\Lambda^2/D$  and the loss rate at the wall. The latter depends on the volume-to-surface ratio  $V/A$ , mean-velocity towards the surface  $\bar{v}$ , and the sticking coefficient  $\gamma$ . This coefficient describes the chance of the incoming particle to adsorb on the surface.

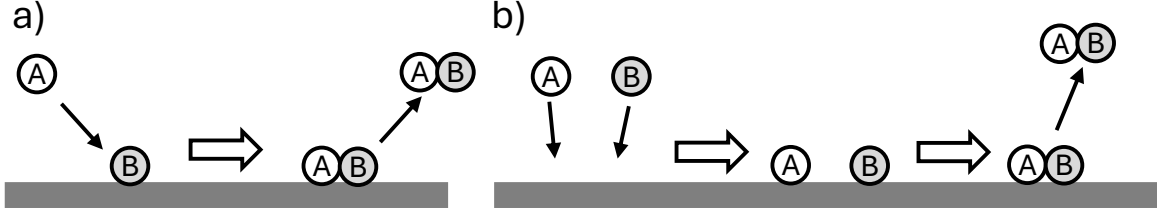


Figure 2.3: A sketch of the Eley-Rideal (a) and Langmuir-Hinselwood (b) mechanism.

$$K_{ER} = \left[ \frac{\Lambda^2}{D} + \frac{V}{A} \frac{2(2-\gamma)}{\gamma \bar{v}} \right]^{-1} \quad (2.6)$$

The particle balance for the gas and surface phase for a general adsorption reaction  $A + B_s \longrightarrow AB_s$  are given in equation 2.7. The volume-to-surface ratio must again be considered through the factor  $\zeta \equiv \frac{V}{S_{tot}A}$  in  $\text{m}^{-2}$ . The surface coverage  $\theta_M$  is the ratio of  $S_M$  and the total surface site densities  $S_{tot} = 10^{15} \text{ cm}^{-2}$  [31].

$$\begin{aligned} \frac{dn_A}{dt} &= -K_{ads}\theta_B n_A \\ \frac{d\theta_{AB}}{dt} &= \zeta K_{ads}\theta_B n_A = -\frac{d\theta_B}{dt} \end{aligned} \quad (2.7)$$

Dissociative adsorption of a molecule can similarly be included, by splitting the process in two parts: 1) the molecule is adsorbed; 2) it dissociates to two adsorbed species. It typically requires two empty sites:  $AB + 2S_f \longrightarrow A_s + B_s$ , where  $S_f$  represents a free surface-site with a surface coverage  $\theta_f$ .

$$\frac{d\theta_A}{dt} = \frac{d\theta_B}{dt} = \zeta K_{diss.ads.} \theta_f^2 n_{AB} \quad (2.8)$$

The LH reaction rate  $K_{LH}$  of equation 2.9 is often described using Arrhenius equation, using a surface diffusion frequency  $\nu$  of  $1 \times 10^{15} \text{ s}^{-1}$ , the reaction activation barrier  $E_a$  and diffusion energy barrier  $E_d$  [31]. The latter depends on the properties of the surface.

$$K_{LH} = \frac{\nu}{4} \exp\left(-\frac{E_a + E_d}{k_b T_{surface}}\right) \quad (2.9)$$

For instance,  $A_s + B_s \longrightarrow AB_s + S_f$  frees up a surface site and has a rate,

$$\frac{\partial \theta_{AB}}{\partial t} = K_{LH} \theta_A \theta_B \quad (2.10)$$

These reactions give a total overview of chemical impact a surface may have on the overall plasma chemistry. On a dielectric surface, ER-reactions typically dominate since the diffusion energy barrier is high [32]. This energy barrier is lower on metallic surfaces, thus LH-reactions are more important on metals.

## Global model

The plasma chemistry requires a great number of reactions. This is especially true when considering gas flows with multiple molecular gases, e.g.  $N_2$  with  $H_2$ . A global model is often used for the plasma chemistry. The spatial gradients are omitted to simplify the calculations. This allows for including a great number of species and reactions into the model for a limited computation time [63]. For instance, He et al. modelled a  $He/N_2/O_2$  considering 138 species and 11799 reactions [64].

The continuity equation is solved for steady-state condition. The particle flux is simplified to one dimension with a fixed speed  $v$ :  $\vec{v}_M = v\hat{x}$  with unit vector in the  $x$ -direction  $\hat{x}$ . This results in a *plug flow* system of equation 2.11, where the residence time  $t_{res} = x/v$  is used. Such an ordinary differential equation can easily be solved by common solvers.

$$\frac{\partial n_M}{\partial t_{res}} = R_M(x) \quad (2.11)$$

Including the surface reactions is not straightforward. First, the differential equation of the gas and surface phase reactions becomes a stiff problem. The surface reaction rates are much smaller than that of the gas phase, thus corresponding time scales are quite different. This introduces instabilities in the solution. It can be fixed by using a Radau method that is designed to control the error [65].

Second, the steady-state solution for the surface composition of equation 2.4 dictates that the composition is in equilibrium with the gas phase at position  $x$ , i.e.  $t_{res}$ . If the model is solved using an empty surface, then there is a net particle flux towards the surface. This is not realistic. Rather, the model must have a zero net particle flux to the surface, i.e.  $R_{surf,M}(x, t) = 0$ .

The steady-state solution for  $S_M$  can be obtained analytically or numerically. An analytical solution gives a set of surface coverages that are a function of the volumetric densities. Such a solution is readily found for simplistic systems, i.e. with a limited amount of species and reactions. For an extended list of reactions and species obtaining such a solution is not as straightforward. It is more practical to obtain the solution numerically. For instance, the model can be run iteratively until  $\frac{\partial S_i}{\partial t_{res}} = 0$  is achieved. The simplest method would be to neglect the  $t_{res}$  dimension, i.e. an homogeneous surface composition along the gas flow. The surface composition will be updated each iteration and the difference at  $t_{res} = 0$  and  $t_{res,max}$  serves as a check for a net particle flux. This is done for the kinetic model used in section 4.3. Alternatively, one could check if the net particle flux is zero at each segment  $t_{res,i} + \delta t_{res}$ . This is computationally more cumbersome, but considers spatial gradients in the surface composition as result of gradients in the volumetric densities.

Finally, the main downside of a global model is the lack of spatial dimensions. The EEDF and  $n_e$  are not constant between the electrodes. This may also apply along the gas stream, because a changing gas mixture will affect the EEDF. Experiment and modelling shows that the electric field greatly varies between the electrodes of a micro atmospheric pressure plasma jet ( $\mu$ APPJ) [66–68]. The rate coefficient for electron impact reactions do not linearly scale with  $E/N$ , but rather exponentially. Therefore, assuming a spatial average introduces discrepancies of those rates compared to reality. This introduces an ambiguity in the electron-impact reactions.

## 2.2 Infrared Absorption Spectroscopy

The gas phase density and surface coverage of molecules can be measured using a Fourier Transform Infrared (FTIR) spectrometer. It generates a wide spectrum in the MIR region of the electromagnetic spectrum. Vibrational transitions that induce a shift in the dipole momentum can be observed. In the gas phase, this means that non-homonuclear diatomic, triatomic, and more complex molecules can be observed. On the surface, homonuclear molecules can be observed as well, because the symmetry breaks once they are bound to a surface. Therefore, the FTIR spectrometer is a versatile and widely applicable technique for our purposes.

### 2.2.1 Principles of Fourier-Transform IR Spectrometry

In this thesis, the Vertex 70v spectrometer of Bruker is used. The accompanying OPUS software is well designed to acquire and process measured interferogram, to produce the spectrum. (Yet, the multitude of options in their menu may repel first time users from even trying to understand it all.) This subsection will attempt to give an overview on how the spectrum is obtained (with the hope of assisting first-time users to acquire the perfect spectrum).

The spectrometer creates a broad spectrum of MIR light by heating up an U-shaped silicon carbide piece. The light is spectrally resolved using a Michelson interferometer, see figure 2.4. An interference signal, i.e. interferogram, is created by interfering two light beams with a phase shift introduced by an optical path difference (OPD). This is controlled by splitting the incoming light beam and reflecting it on a stationary and movable mirror. The interferogram is obtained as function of the retardation of the movable mirror. It moves in an oscillating manner. The *scanner velocity*  $v$  sets the speed of the acquisition that is presented as a frequency  $f$  in Hz and it is related to the speed of the mirror as  $v = f/2\tilde{\nu}_{HeNe}$  [69]. The wavenumber of the helium-neon laser  $\tilde{\nu}_{HeNe}=15\,798.8\text{ cm}^{-1}$  is used to measure the OPD. The scan speed is set according to the detector used during the experiment, e.g. 40 kHz for the typically used mercury cadmium telluride (MCT) detector. In the end, the spectrum is obtained by applying a discrete fourier transformation on the measured interferogram [70].

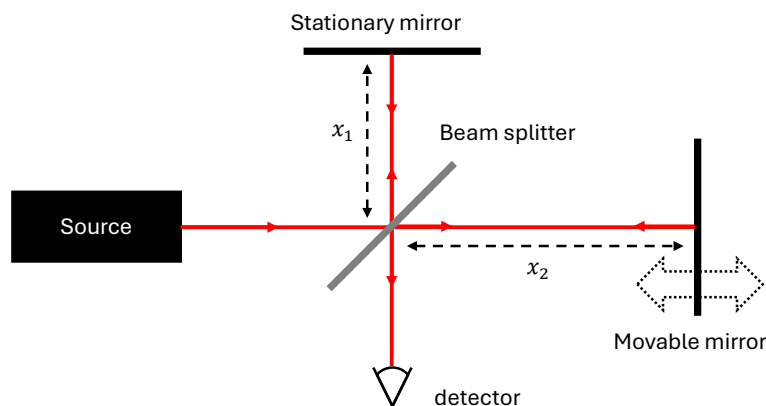


Figure 2.4: A sketch of a typical Michelson interferometer.

The interferogram  $I$  is a function of the optical path difference  $\delta$  and the wavenumber  $\tilde{\nu}$ . The optical path difference  $\delta = 2n(x_2 - x_1)$  is a function of the distances between the beam splitter and the mirrors  $x_{1,2}$  and refractive index  $n$  of the medium between the optical elements. Equation 2.12 gives the relation for a monochromatic light source with  $\tilde{\nu}_0$ , where signal intensity  $B(\tilde{\nu}_0)$  is the combination of the light intensity, responsivity of the detector, and spectral properties of the optical components, e.g. beam splitter.

$$I(\delta) = \frac{1}{2}B(\tilde{\nu}_0)[1 + \cos(2\pi\tilde{\nu}_0\delta)] \quad (2.12)$$

The frequency is obtained by counting the number of maxima  $N$  over a change in optical path  $\Delta\delta = \delta_{max} - \delta_{min}$  as  $\tilde{\nu} = N/\Delta\delta$ . Following this relation, two frequencies can be distinguished from each other if the number of detected maxima differs by at least 1 over  $\Delta\delta$ , i.e.  $|N_i - N_j| > 1$ . Thus, the spectral resolution is set by total optical path difference as  $\Delta\tilde{\nu} = 1/\Delta\delta$  [70]. The maximum spectral resolution is  $0.2 \text{ cm}^{-1}$  for the Vertex 70v spectrometer, which translates to a  $\Delta\delta$  of 5.0 cm.

Furthermore, the interferogram is padded with zeros on the edges. It smoothens the spectrum by artificially increasing  $\Delta\delta$ . This is better than a typical polynomial-based interpolation function. It is controlled by the *zerofilling factor* that is defined as the ratio between the zero-filled and the original interferogram.

The displacement of the movable mirror is measured using a He-Ne laser with  $\tilde{\nu}_{HeNe}$ . This sets the maximum detectable wavenumber to  $7901 \text{ cm}^{-1}$ , when considering the Nyquist-Shannon sampling theorem on avoiding aliasing [69]. The upper wavenumber limit, i.e. *wanted high frequency limit*, can be lowered to reduce the data file size in the OPUS software. Yet, the software will adjust the real upper limit accordingly. Therefore, one must be careful to avoid aliasing. Generally, it is safe to reduce the upper limit to  $5266.27 \text{ cm}^{-1}$ , since the spectrum's intensity is negligible above this frequency.

The interferogram consists of a DC- and a AC-term. The latter contains the spectral information, therefore the DC-term is omitted during the analysis. The relation for the AC-term for a broadband light source is given in equation 2.13 [71], where the following formulas are given in the complex domain with  $I = \text{Re}\{\tilde{I}\}$ . This relation considers the phase dispersion  $\theta(\tilde{\nu})$  that is inherent to any measured interferogram. The goal of the upcoming analysis is to get the best approximation of the actual spectrum  $B(\tilde{\nu})$ .

$$\tilde{I}(\delta) = \int_{\tilde{\nu}} B(\sigma)e^{i\theta(\tilde{\nu})}e^{2\pi i\tilde{\nu}\delta}d\tilde{\nu} \quad (2.13)$$

The spectrum is obtained through a Fourier transformation that is presented in equation 2.14. The apodisation  $A(\delta)$  is a temporal weighting function that affects the instrumental line shape  $\psi_{instr}(\sigma - \tilde{\nu})$ . The mere fact of measuring a finite size interferogram introduced a boxcar *apodiation function*. This results in  $\psi_{instr}(x) = \text{sinc}(x)$  that is unsuitable for spectral analysis. The spectral leakage to the neighbouring regions is greatly reduced when using a third order Blankman-Harris apodisation function. Also, the resulting instrumental line shape is well approximated as a Gaussian, which is often encountered and used in optical spectroscopy [72].

$$\begin{aligned}
F(\tilde{\nu}) &= \int_{\delta} A(\delta) \tilde{I}(\delta) e^{-2\pi i \tilde{\nu} \delta} d\delta \\
&= \int_{\sigma} B(\sigma) e^{i\theta(\sigma)} \int_{\delta} A(\delta) e^{-2\pi i (\tilde{\nu} - \sigma) \delta} d\delta d\sigma \\
&= \int_{\sigma} B(\sigma) e^{i\theta(\sigma)} \psi_{instr}(\tilde{\nu} - \sigma) d\sigma = F'(\tilde{\nu}) * L(\tilde{\nu})
\end{aligned} \tag{2.14}$$

The impact of apodisation on the instrumental line shape is visualised in figure 2.5. A synthetic spectrum is calculated using Planck's radiation law for a body at 1000 K with a single narrow Gaussian peak at  $2000 \text{ cm}^{-1}$  that has a full width at half maximum (FWHM) of  $0.1 \text{ cm}^{-1}$ . This spectrum is transformed to an interferogram following equation 2.13 using a  $1.0 \text{ cm}^{-1}$  spectral resolution and a  $10\,000 \text{ cm}^{-1}$  acquisition frequency. The resulting interferogram is plotted with a boxcar and the Blackmann-Harris apodisation functions in figure 2.5b. Note that the side lobes of the interferogram are not well seen since the full interferogram is shown. The spectra resulting from the interferogram with either the boxcar or Blackman-Harris function are shown in figure 2.5c; together with the original spectrum of figure 2.5a. The *boxcar*-spectrum yields the expected *sinc*( $x$ )-function that affects the spectrum even after  $20 \text{ cm}^{-1}$ . In contrast, the instrumental line shape resulting from the *Blackmann-Harris* function only affects the spectrum within  $\Delta\tilde{\nu} = \pm 3 \text{ cm}^{-1}$ . Thus, applying the Blackman-Harris apodisation function effectively limit the spectral leakage.

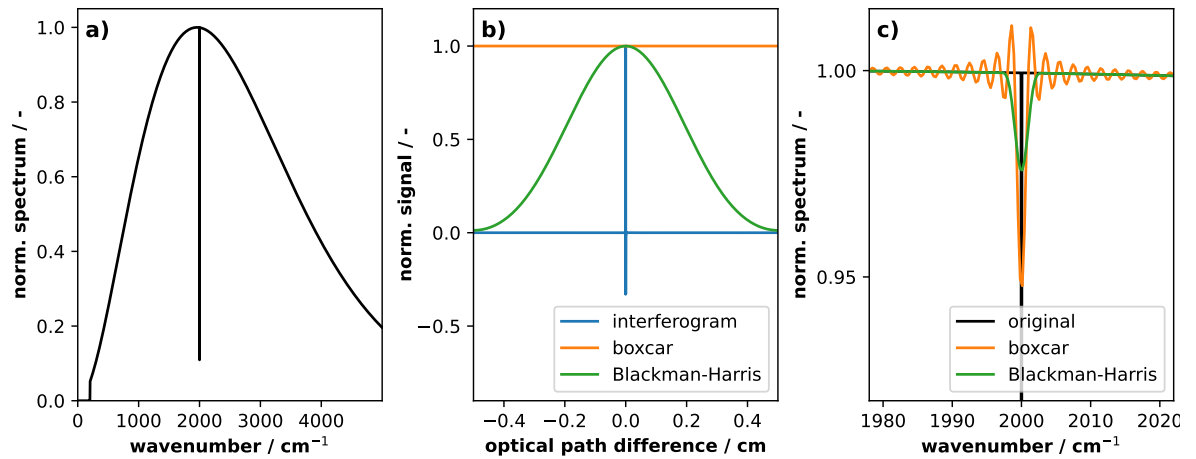


Figure 2.5: Transformation of a synthetic spectrum (a) that is translated to a double-sided interferogram (b) and converted to the apparent spectrum (c).

Another point concerning the instrumental line shape is the beam divergence. Its effect can be understood by considering a diverging beam that passes through the interferometer. The light with a divergence angle  $\theta$  will experience a different path length than the light at the center:  $\delta' = \delta / \cos \theta$ . The wavenumber axis of the corresponding spectrum will, therefore, be scaled as  $\tilde{\nu}' = \tilde{\nu} \cos \theta$ . The measured spectrum will be a combination of both spectra resulting in an apparent shift and a non-Gaussian like instrumental line shape. This can be prevented by ensuring that either the aperture

of the spectrometer or the spectral resolution is not too high as described by Davies et al. [73].

The phase dispersion is corrected using the Mertz theorem, which is referred to as the *phase correction mode* in the OPUS software [74]. This theorem assumes that the dispersion only has broad spectral properties. It can be approximated using a low resolution spectrum, where the resolution is set by the *phase resolution*. The spectrum is calculated from a small part  $\pm\delta_0$  from the interferogram to obtain a coarse spectrum  $P(\tilde{\nu})$ , see equation 2.15. This interferogram is zero padded such that  $P(\tilde{\nu})$  has the same data length as  $F(\tilde{\nu})$ . Under the assumption that the instrumental function is a Kronecker delta function, i.e. an ideal device, the spectrum can be recovered following equation 2.16.

$$P(\tilde{\nu}) = \int_{\delta=-\delta_0}^{+\delta_0} A(\delta)\tilde{I}(\delta)e^{-2\pi i\tilde{\nu}\delta}d\delta \approx |P(\tilde{\nu})|e^{i\theta(\tilde{\nu})} \quad (2.15)$$

$$B(\tilde{\nu}) \approx \text{Re}\{F(\tilde{\nu})e^{-i\theta(\tilde{\nu})}\} = |F(\tilde{\nu})|\cos[\phi(\tilde{\nu}) - \theta(\tilde{\nu})] \quad (2.16)$$

The effect of the phase correction is visualised for a measured single-sided interferogram in figure 2.6a. The apodisation function is the third Blackmann-Harris function. The phase dispersion introduces an ambiguity in the position of the zero-point-distance (ZPD), i.e.  $\delta = 0$ . Therefore, the measurement starts before the ZPD to ensure that this high intensity point is fully measured. A ramp is applied to the apodisation function from about  $-0.2$  to  $0.2 \text{ cm}^{-1}$  to minimise asymmetries (that are introduced by the ambiguity) to impact the spectrum [71].

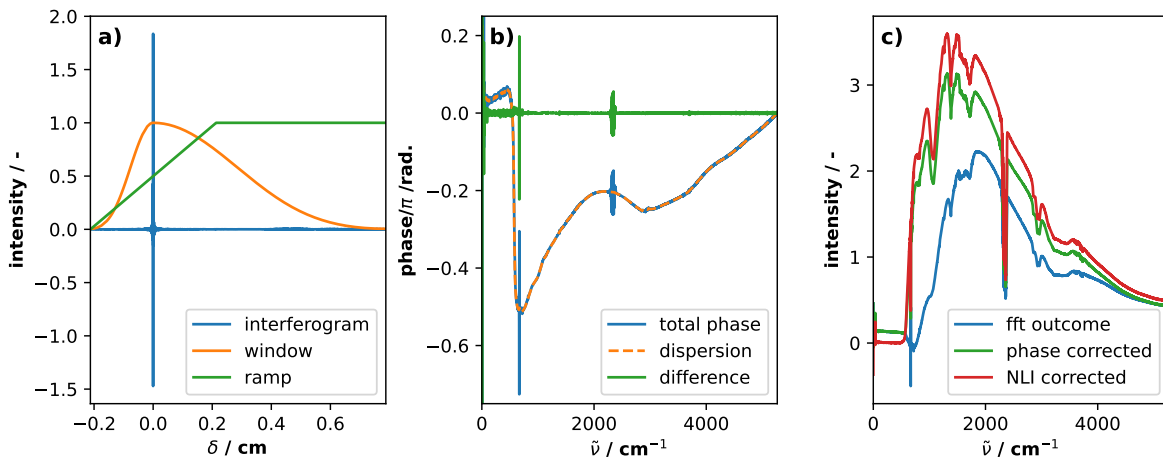


Figure 2.6: A measured single-sided interferogram (a), the resulting phase spectra (b), and the uncorrected, phase corrected, and non-linearity corrected spectra (b).

The phase spectrum is corrected for the dispersion following equation 2.16. The total phase  $\phi$  and dispersion phase  $\theta$  spectra are plotted in figure 2.6b. The dispersion-phase spectrum only shows broad spectral features. The difference between the total and dispersion phase spectra is used to calculate the apparent spectrum, which is shown in subfigure c.

If the dispersion is not properly corrected for, then negative values in the spectrum or asymmetric line shapes may be observed. The former is observed in the uncorrected

spectrum, which is negative around  $670\text{ cm}^{-1}$ . Once the dispersion is removed, the negative values disappear, see the *phase corrected* spectrum in subfigure c.

The spectra in subfigure 2.6c have non-zero values below the cutoff frequency of  $550\text{ cm}^{-1}$ . This arises from the non-linear response of the MCT detector that is not considered yet [75, 76]. The measured interferogram is corrected following equation 2.17. The coefficients  $\alpha$  and  $\beta$  can be estimated from the previously estimated spectra [75]. The final result is plotted as *NLI corrected*.

$$I_{actual}(\delta) \approx I_{corr}(\delta) = \alpha (I_{measured}(\delta) + \beta I_{measured}^2(\delta)) \quad (2.17)$$

In the end, spectra can be reliably acquired over a wide spectral range. The analysis of these spectra in the gas and surface phase absorption spectra will be discussed in the next subsections.

### 2.2.2 Gas-Phase IR Absorption Spectra

Gas phase densities are often measured using absorption spectroscopy. The density is estimated from the comparison of measured and synthetic spectra. The line-of-sight diagnostic is applied from the THz to the ultraviolet regime. In the MIR regime  $400\text{--}4000\text{ cm}^{-1}$ , the rotational-vibrational transitions of the electronic ground state of non-symmetric molecules are probed. This makes the MIR regime suitable for measuring the density of the corresponding species.

The results are often presented as transmittance spectra  $T$  as function of the wavenumber  $\tilde{\nu}$  in  $\text{cm}^{-1}$ . Following equation 2.18, the transmittance is obtained from the ratio of the measured spectrum  $B(\tilde{\nu})$  and the background spectrum  $B_0(\tilde{\nu})$ . This ratio is related to the absorption coefficient  $\kappa$  and absorption path length  $L$  using the Beer-Lambert law[70],

$$T(\tilde{\nu}) = \frac{B(\tilde{\nu})}{B_0(\tilde{\nu})} = e^{-\kappa(\tilde{\nu})L} \quad (2.18)$$

The spectral information of the transitions are encapsulated in  $\kappa$ , see equation 2.19. It depends on the density  $n_M$  in  $\text{cm}^{-3}$  of observed species  $M$  and the summation over the linestrength  $S_{M,ik}$  and the line profile  $\psi_{M,ij}$  over all rotational-vibrational transitions  $|i\rangle \rightarrow |j\rangle$ .

$$\kappa(\tilde{\nu}) = \sum_M n_M \sum_{ij} S_{M,ij} \psi_{M,ij}(\tilde{\nu}) \quad (2.19)$$

The line strength considers the strength of the transition, as the name suggests. When the translational, rotational, and vibrational degrees of freedom are in equilibrium, then its description can be simplified to equation 2.20 [77]. Here,  $I_a$  is the natural abundance of the specific isotopologue,  $A_{ij}$  is the Einstein coefficient for spontaneous emission,  $\tilde{\nu}_{ij}$  is the central wavenumber of the transition,  $g_j$  is the degeneracy of the upper-state  $|j\rangle$ ,  $Q(T)$  is the partition function at gas temperature  $T$ ,  $E_i$  is the energy-level of the lower-state  $|i\rangle$  in  $\text{cm}^{-1}$ , and  $c_2$  is the physical constant  $hc/k_B \approx 1.44\text{ cm K}$ .

$$S_{ij} = \frac{I_a A_{ij}}{8\pi c \tilde{\nu}_{ij}^2} \frac{g_j}{Q(T)} e^{-c_2 E_i/T} (1 - e^{-c_2 \tilde{\nu}_{ij}/T}) \quad (2.20)$$

The lineshape is a convolution of Doppler and pressure broadening under the conditions studied in this thesis. In addition, a pressure shift  $\Delta\tilde{\nu}_p$  is introduced that is calculated considering the collisions with itself and the main colliding species (helium or air in this thesis). This yields the Voigt lineshape of equation 2.21. The HITRAN database provides all the required constants for these relations [78].

$$\psi_{ij}(\tilde{\nu}) = Voigt(\tilde{\nu}, \tilde{\nu}_{ij} - \Delta\tilde{\nu}_p, \sigma_{doppler,ij}, \gamma_{pressure,ij}) \quad (2.21)$$

The instrumental broadening is applied on the total transmittance spectrum, following equation 2.14. In a well designed experiment, the reference spectrum  $B_0$  does not show sharp spectral features. The observed reference spectrum  $B_{obs,0}$  then equals to the actual spectrum  $B_{act,0}$ :  $B_{obs,0} = B_{act,0} * G \approx B_{act,0}$ . This greatly simplifies the calculations required to obtain a synthetic measured transmittance spectrum as equation 2.22.

$$T_{obs}(\tilde{\nu}) \approx T_{act}(\tilde{\nu}) * G(\tilde{\nu}, \sigma_{instr}) \quad (2.22)$$

A proper comparison of measured and synthetic spectra typically requires a good description of the baseline. Alternatively, the derivative of the spectrum can be compared to that of the measured spectrum. Broad features, such as baseline fluctuations, will have a low  $\partial T/\partial\tilde{\nu}$  whereas the rotational-vibrational lineshapes usually are sharp, i.e. a high  $\partial T/\partial\tilde{\nu}$ . These features can easily be distinguished in a typical optimising algorithm. However, the uncertainty of resulting densities will be higher compared to fitting  $T(\tilde{\nu})$  itself since numerical derivatives are inherently noisy.

### Limitations and alternatives

The spectral resolution of a FTIR spectrometer is limited by the maximum retardation of the movable mirror of the interferometer. This movement also limits the time resolution. A typical spectrum that will be shown in this thesis requires 30 to 60 seconds. The triggering of the spectrometer permits that the time resolution can be lowered to sub-ms, when measuring a repetitive signal [79]. However, such measurements require several hours per measurement campaign, since the acquisition of a single interferogram is distributed over several plasma cycles.

In contrast, Quantum Cascade Lasers (QCLs) can reach nanosecond time resolution in a fraction of the acquisition time [80, 81]. They are also characterised by a very low instrumental broadening, which is set by the response of the detector. However, QCLs have a limited spectral window, e.g. a single-mode laser can only scan over  $1 \text{ cm}^{-1}$ . Therefore, it is not well suited to measure a wide variety of species. In addition, the spectral resolution is less crucial for the measurements presented in this thesis. A high spectral resolution is not required if the rotational-vibrational density distributions are well described, which is true once these degrees of freedom equilibrate. Also, the processes in this study are not characterised by a high repetition frequency, thus acquiring a high time resolution is not feasible.

Absorption spectroscopy itself has three limiting factors. Firstly, only transitions that induce a net change in the dipole moment can be detected. In the MIR, where vibrational transitions are probed, this means that only asymmetric vibrations are observed. Homonuclear diatomic molecules can, therefore, not be observed. Such

species can be observed when triggering an electronic transition by changing to the NIR or visible part of the spectrum. It comes at the cost of a weaker line strength that lowers the sensitivity of the measurement. This can be overcome by increasing the absorption path length as we will discuss later.

Dipole-inactive stretch modes can be observed with Raman spectroscopy, since the signal depends on the polarisability tensor [82]. Homonuclear diatomic molecules such as O<sub>2</sub> and N<sub>2</sub> can be measured with this technique. For instance, Grofulović et al. measured the densities of CO<sub>2</sub>, CO, N<sub>2</sub>, and O<sub>2</sub> simultaneously in a low pressure glow discharge [83]. It shows good agreement with FTIR absorption spectroscopy [84]. Therefore, it is considered as a reliable diagnostic that complements absorption spectroscopy.

Secondly, absorption spectroscopy is a line-integrated method. Density gradients along the light path are averaged out, i.e. they are not observed. It is crucial that such gradients are minimised in the experiments. This can be done by probing only the positive column of a low pressure DC glow discharge, which is known for being spatially homogeneous [79, 85].

Alternatively, Raman spectroscopy or (two photon) laser-induced fluorescence (LIF) can measure local densities, e.g. see [86]. The scattered and fluorescence light are typically acquired perpendicular to the laser light, thus the densities can be measured along the direction of the laser propagation. LIF requires a de-excitation model to describe the observed fluorescence. This, together with the calibration factor, are the main source of uncertainty. For instance, Budde et al. simultaneously measured CO with two-photon LIF and OH with LIF and calibrated their measurements using an absolute CO measurement on a known mixture [87]. This introduced a systematic error of 60%, which is not uncommon for two-photon LIF [88]. Nonetheless, LIF techniques can reproduce relative trends very accurately.

Thirdly, the sensitivity relies on the absorption path length. The sensitivity can be increased by using a multipass cell. For instance, Sadiék et al. apply a white cell around a plasma source such that the absorption path length is increased four fold [89]. Alternatively, this can also be done ex-situ. A multipass cell can be installed in the sample compartment of a FTIR spectrometer [90, 91]. Such ex-situ measurements are better suited for absolute density measurements, since the IR spectra are better defined. Yet, it loses information about the excitation of the species by the plasma that is acquired with typical *operando* measurements, e.g. see [92]. Also, one should consider chemical reactions that may occur during the transport from the plasma to the cell and inside the cell. For instance, in the exhaust of a He/N<sub>2</sub>/O<sub>2</sub> plasma, the plasma products further oxidise the nitrogen oxides, since O<sub>3</sub> reacts with NO to produce NO<sub>2</sub> [90].

### 2.2.3 Infrared Reflection Absorption Spectroscopy

The reflection of electromagnetic radiation is guided by the Fresnel coefficients. The reflection coefficients  $r$  from phase  $j$  to  $k$  for p- and s-polarisation (parallel and perpendicular to the normal of the surface) are [93–95],

$$r_{p,jk} = \frac{\hat{\epsilon}_k \xi_j - \hat{\epsilon}_j \xi_k}{\hat{\epsilon}_k \xi_j + \hat{\epsilon}_j \xi_k}, \quad r_{s,jk} = \frac{\mu_k \xi_j - \mu_j \xi_k}{\mu_k \xi_j + \mu_j \xi_k} \quad (2.23)$$

where  $\hat{\epsilon}_j$  is the complex dielectric constant and  $\mu_j$  the magnetic permeability for phase  $j$ . The relative magnetic permeability is close to unity when discussing high frequency EM-waves such as IR-light, even for iron [96]. Literature prefers to use an angular dependent quantity  $\xi_j = \hat{n}_j \cos \theta_j$  that considers the complex refractive index  $\hat{n}_j = \sqrt{\mu_j \hat{\epsilon}_j} \equiv n_j + ik_j$  and the angle of incident  $\theta_j$  in phase  $j$ . The reflectance  $R$  is the absolute square of the respective reflection coefficient, i.e.  $R = |r|^2$ .

### 3 phase system

The reflection on a metallic substrate can be described as 3-phase system: air, film, and metal. The last phase is assumed to be infinitely thick such that no reflection can occur after the film-metal interface. This condition is met if the metal layer thickness is much larger than the skin depth ( $d_{metal} \gg 1/k_{metal}$ ), so all light is absorbed by the substrate. The total reflection coefficient  $r$  is derived from the summation of all reflection paths inside the phases, see equation 2.24. It relies on the reflection coefficients of the individual interfaces  $r_{12}$  and  $r_{23}$  as well as a phase difference coefficient  $\beta = 2\pi\tilde{\nu}\xi_2 d$ . The absorption inside phase 2 with thickness  $d$  is considered by  $\beta$ .

$$r = \frac{r_{12} + r_{23}e^{2i\beta}}{1 + r_{12}r_{23}e^{2i\beta}} \quad (2.24)$$

An example of a 3-phase system is presented as a function of the angle of incidence in figure 2.7. A carbonyl monolayer (1 nm,  $\hat{n} = 1.5 + i0.2$ ) on an iron substrate ( $\hat{n} = 4.08 + i0.38$ ) in air is considered to be irradiated by a monochromatic light source with  $\tilde{\nu}_0 = 1730 \text{ cm}^{-1}$  [69, 97]. In subfigure a, the reflectance  $R_0$  is plotted as function of the angle of incidence for a clean substrate. The reflectance changes in the order of 0.1% when introducing a carbonyl monolayer in subfigure b, where  $\Delta R = R_0 - R$  is plotted as function of the angle of incidence.

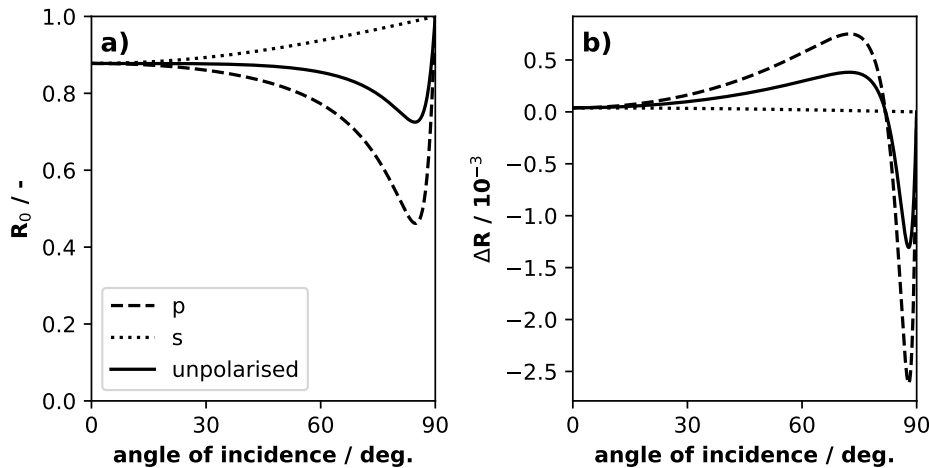


Figure 2.7: The reflection on a clean iron substrate (a) and reflection change when introducing a 1 nm film carbonyl film on the iron substrate (b) at  $1730 \text{ cm}^{-1}$  following equation 2.24.

The angle dependence is important aspect of the overall reflection. A grazing angle typically optimises the sensitivity of the reflectance on metallic substrates. For iron,

the maximum  $\Delta R$  is observed at  $71.8^\circ$ , i.e.  $\theta_{max}$ . The response of the surface quickly diminishes after this angle. It even becomes negative above  $81.5^\circ$ . This is also seen for dielectric substrates as will be presented later. Thus, an angle just below  $\theta_{max}$  is chosen to prevent these contributions.

The polarisation of light is also important when examining the reflection. The s-polarisation has a higher overall reflectance on a metallic substrate compared to p-polarisation. However, only the p-polarised reflectance changes when introducing a thin absorbing film. This is explained using the surface selection rule [69, 98]. A change in the dipole moment parallel to the surface is mirrored in the metal such that the net dipole moment remains zero, hence s-polarised light cannot observe changes in the surface composition. The MIR source is a glow bar in this thesis. The black-body radiation is unpolarised. This increases the overall reflectance compared to only observing the p-polarisation, but lowers the sensitivity of  $\Delta R$  on the absorption by the film.

### N phase system

The reflection on a non-metallic substrate requires to generalise the reflection coefficient to a N-phase system. The matrix of equation 2.25 describes how each phase interacts with the incoming light source [93]. The phase difference coefficient is defined for each phase:  $\beta_j = 2\pi\tilde{\nu}\xi_j d_j$ . The polarisation is considered by  $\eta_j$  as  $\eta_j = \xi_j/\mu_j$  for the p-polarisation and  $\eta_j = \xi_j/\hat{\epsilon}_j$  for s-polarised light. The final matrix elements  $m_{kl}$  are inserted in equation 2.26 to acquire the reflection coefficient. This formulation reproduces equations 2.23 and 2.24 when settings N to 2 and 3, respectively.

$$M = M_2 M_3 \dots M_{N-1}, \quad \text{with} \quad M_j = \begin{bmatrix} \cos \beta_j & \frac{-i}{\eta_j} \sin \beta_j \\ -i\eta_j \sin \beta_j & \cos \beta_j \end{bmatrix} \quad (2.25)$$

$$r = \frac{(m_{11} + m_{12}\eta_N)\eta_1 - (m_{21} + m_{22}\eta_N)}{(m_{11} + m_{12}\eta_N)\eta_1 + (m_{21} + m_{22}\eta_N)} \quad (2.26)$$

The reflectance on a dielectric material can be calculated using this formulation. In figure 2.8, the reflectance on a 1 mm thick iron(III)oxide ( $\text{Fe}_2\text{O}_3$ ) substrate ( $\hat{n} = 2.055 + 0.03i$ ) is presented [97]. This is calculated in a 4 phase system: air-film- $\text{Fe}_2\text{O}_3$ -air. A fourth layer is necessary. The light is not fully absorbed before reaching the backside of the substrate, thus the light reflects on the  $\text{Fe}_3\text{O}_3$ -air interface as well.

$R_0$ ,  $R$ , and  $\Delta R$  are lower on  $\text{Fe}_2\text{O}_3$  than on pure Fe, which lowers the signal-to-noise ratio. The reflection of p-polarised light is zero at the Brewster angle.  $\Delta R$  is negative from  $0^\circ$  to  $90^\circ$ , so the reflectance increases with the formation of the thin film. Also, the s-polarisation mostly contributes to the  $\Delta R$  signal. Thus, mostly stretch modes parallel to the surface are observed instead of the perpendicular orientation on metals. This is especially true at the optimum angle for IRRAS of metallic substrates ( $\sim 70^\circ$ ).

Furthermore, the N-phase formulation is very useful when considering the reflection spectra of a metallic oxide layer formed on top of the metallic substrate. This will be used in figure 2.9 to estimate the impact of an oxidised top layer on the metallic iron substrate.

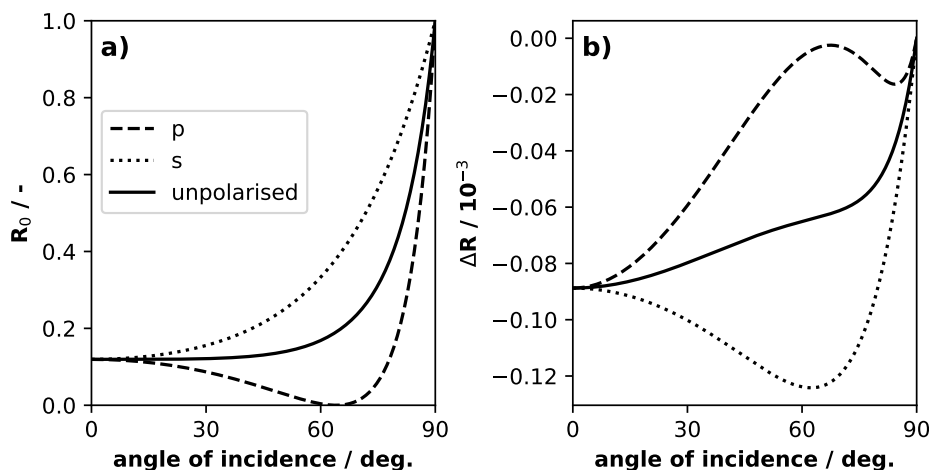


Figure 2.8: The reflection on a clean  $\text{Fe}_2\text{O}_3$  substrate (a) and reflection change when introducing a 1 nm film carbonyl film on the iron substrate (b) at  $1730\text{ cm}^{-1}$  following equation 2.26.

### Reflection spectra

The absorption features of the vibrational transitions are considered in the complex refractive index of the film as presented in equation 2.27. The imaginary part of the refractive index is proportional to  $\kappa$  induced by a molecular vibrational transition, similar as the gas phase. The imaginary part of the refractive index,  $k$ , is often approximated by a Gaussian line shape, e.g. see [99]. It depends on the absorption constant  $\kappa_0$ , full-width-half-maximum (FWHM)  $= \sqrt{8 \ln(2)}\sigma$ , and central wavenumber  $\tilde{\nu}_0$ . The Gaussian-like line shape arises from naturally occurring irregularities of the surface morphology. They perturb the central wavenumber of the band. The real component of the refractive index is obtained using the Kramer-Kronig transformation, where  $n_\infty$  is the refractive index far away from the vibrational transition and  $P$  is the Cauchy principle value [100]. However, such a translation is numerically unstable. Thus,  $n$  is approximated by a Dawson function  $D(x)$  with a scaling factor  $a$  instead.

$$\begin{aligned}
 k(\tilde{\nu}) &= \frac{\kappa(\tilde{\nu})}{4\pi\tilde{\nu}} = \frac{\kappa_0}{32\pi\sqrt{\pi}\tilde{\nu}\sigma} e^{-\frac{\tilde{\nu}-\tilde{\nu}_0}{2\sigma^2}} \\
 n(\tilde{\nu}) &= n_\infty + \frac{2}{\pi} P \int_0^\infty \frac{sk(s)}{s^2 - \tilde{\nu}^2} ds \approx n_\infty + a \cdot D\left(\frac{\tilde{\nu} - \tilde{\nu}_0}{\sqrt{2}\sigma}\right)
 \end{aligned}
 \tag{2.27}$$

Exemplary spectra of a carbonyl film growth on pure Fe, 50 nm  $\text{Fe}_2\text{O}_3$  on Fe, and pure  $\text{Fe}_2\text{O}_3$  substrate (of figure 2.8) are plotted for an angle of incidence of  $70^\circ$  in figure 2.9b. The refractive index components of a carbonyl stretch band are reproduced from figure 13.19 of [69] and plotted in subfigure a.

The interpretation of a reflection spectrum on metallic iron is straightforward, because the sign of  $\Delta R$  is the same as of the film growth. In literature, the reflectance is often presented in terms of the absorbance  $A = -\ln(R/R_0)$ , which has the same sign as  $\Delta R$ . The desorption of surface-bound species will give a negative absorbance and the formation of a positive absorbance band. This is also true for an oxidised iron

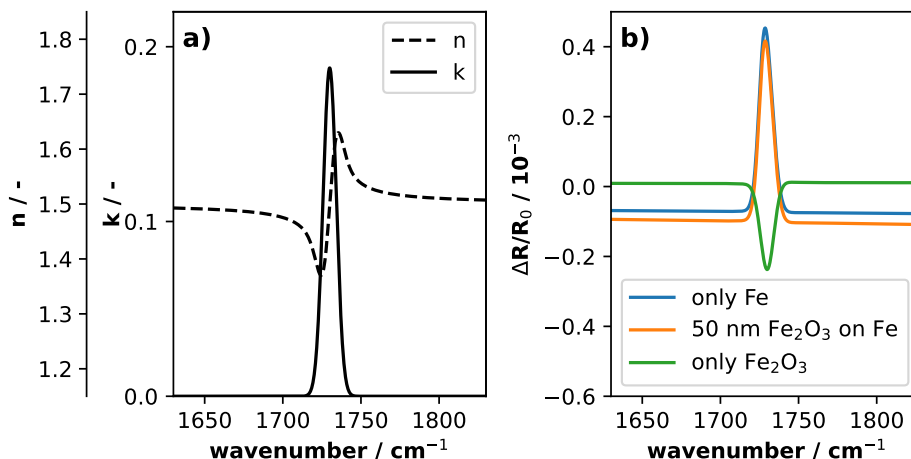


Figure 2.9: The refractive index of a carbonyl thin film (a) and the resulting normalised reflectance contain the signal with and without the carbonyl film for different substrates (b).

toplayer,, where only the baseline is slightly lowered. When reflecting from the  $\text{Fe}_2\text{O}_3$  substrate, the film growth shows an inverted peak. There, the sign of the film growth is opposite to  $A$  and  $\Delta R$ . Thus, one must be careful when analysing such spectra.

### Limitations and alternatives

Reflection absorption spectroscopy only detects changes in the surface composition. Structural ratios (e.g. surface coverages), are obscured by: 1) the reference spectrum may already contain preadsorbed species, 2)  $\kappa$  is affected by the nature of the substrate, 3) only species with a stretch mode that induce a net change in the dipole momentum are visible. These drawbacks can be minimised by carefully controlling the setup, yet this is not always possible. Other diagnostics could be used instead.

Raman spectroscopy can measure IR-inactive stretch modes, as mentioned earlier. It can yield structural ratios as well. For instance, the ratio between crystalline structures can be deduced for silicon [101]. The signal is, however, very weak for smooth metallic surfaces. Surface-enhanced Raman spectroscopy overcomes this issue, by locally enhancing the electric field using metallic nanoparticles [102]. This method requires a careful control of the surface composition and the stability of the nanoparticles, which is not well suited for plasma-surface interaction studies.

Electron energy loss spectroscopy (EELS) is not limited to dipole active or the polarisability tensor as it can observe any adsorbed species [103]. This greatly enlarges to amount of stretch modes that can be observed. It is a good source to acquire spectral positions of stretch modes that may be observed in IRRAS spectra, e.g. for  $\text{NH}_x$  surface groups [104, 105]. The drawback of EELS is that it requires ultra high vacuum ( $<1 \times 10^{-9}$  mbar) conditions. In contrast, typical plasma experiments require moderate pressures of  $>1 \times 10^{-3}$  mbar. Thus, this technique cannot be applied *operando*, unlike optical diagnostics as IRRAS and Raman spectroscopy.

X-ray photoelectron spectroscopy (XPS) is a widely used surface diagnostic. It readily yields structural ratios by comparing the intensity between perturbations in an

electronic structure. For instance, examining the perturbation in the O(1s) spectrum is used to acquire surface coverages of OH and H<sub>2</sub>O on  $\alpha$ -Fe<sub>2</sub>O<sub>3</sub> [106]. Unfortunately, similar to EELS, it requires a ultra high vacuum as well, thus it is not suitable for an *operando* study.

Another point of concern for IR reflection spectra is the overlap of gas phase absorption features. The gas phase contributions can be removed using polarisation-modulation IRRAS (PM-IRRAS) [107–109]. Only p-polarised light contributes to changes in the reflectance on metallic surfaces. This is not the case in the gas phase. The contributions on the surface can be isolated by separately observing p- and s-polarised light. Alternatively, higher-resolution spectra can distinguish the gas phase and surface-bound species as well. The absorption features of the gas phase species are well documented in e.g. the HITRAN database [78]. These contributions should be identified and artificially removed, before continuing with potential surface contributions.

## 2.3 Optical Emission Spectroscopy

Optical emission spectroscopy (OES) is a passive optical diagnostic. Experimentally, it is rather straightforward as the emitted light only needs to be collected and spectrally resolved. An excitation scheme is needed to extrapolate this intensity to the ground state density. Such a scheme drastically complicates the post-processing of emission spectra and is the main drawback of this technique. Nonetheless, it is very useful to characterise the plasma.

The emitted light intensity for a transition from an upper  $|u\rangle$  to a lower state  $|l\rangle$  is described by equation 2.28. The intensity  $I_{l,u}$  is proportional to the spectral response of the system  $R_{sp}(\nu)$ , the captured photon's energy  $h\nu$ , density of the upper level  $N_u$ , and Einstein coefficient for spontaneous emission  $A_l^u$  of the optical transition.

$$I_{l,u} = R_{sp}(\nu)h\nu N_u A_l^u \quad (2.28)$$

The spectral response relates the actual light intensity emitted by the plasma to the measured signal. It considers the solid angle of the collection optics, transmission through the window of the plasma reactor and optical components, reflectance of the mirrors and grating inside the spectrograph, and the sensitivity of the detector. The solid angle describes the portion of light that is captured. It can be maximised by placing the collection optics as close as possible to the source. In a typical OES setup, the light is coupled into the spectrograph using an optical fiber [110, 111]. There, a lens can be used to increase the solid angle of the collected light.

Nitrogen has strong emitting bands between 290 and 420 nm: second positive system (SPS)  $N_2(C^3\Pi_u \rightarrow B^3\Pi_g)$  and first negative system (FNS)  $N_2^+(B^2\Sigma_u^+ \rightarrow X^2\Sigma_g^+)$  [26]. The quantum state of this diatomic molecule  $|n, v, J\rangle$  is characterised by the electronic  $n$ , vibrational  $v$ , and rotational  $J$  levels [112]. The observed emission originates from the transition  $|n', v', J'\rangle \rightarrow |n'', v'', J''\rangle$ . The Einstein coefficient considers the likelihood of the respective optical transition. The Born-Oppenheimer approximation simplifies the description such that the coefficient is proportional to the electronic-vibrational transition moment, Frank-Condon coefficient  $q_{v'v''}$ , and Hönl-London factor [113]. As

a first approximation, the densities of  $N_2(C^3\Pi_u, v)$  and  $N_2^+(B^2\Sigma_u^+, v)$  can be estimated from the intensity of the respective vibrational bands. Equation 2.29 describes the relation of this intensity to the density of the respective electronic-vibrational state for the SPS and FNS systems.

$$\begin{aligned} I_{\text{SPS}}(v' \rightarrow v'') &\propto \nu^4 R_{sp}(\nu) q_{v''}^{v'} [N_2(C, v')] \\ I_{\text{FNS}}(v' \rightarrow v'') &\propto \nu^4 R_{sp}(\nu) q_{v''}^{v'} [N_2^+(B, v')] \end{aligned} \quad (2.29)$$

These bands are useful for characterising the gas temperature and reduced electric field. The gas temperature can be inferred from the rotational distribution of a vibration-electronic excited state. The rotational temperature is equal to the gas temperature when the rotational-translational thermalisation time constant is shorter than the lifetime of the vibrational-electronic excited state [114, 115]. This condition is generally met for  $N_2(C^3\Pi_u)$ .

The reduced electric field can be estimated from the density ratio between  $N_2^+(B^2\Sigma_u^+)$  and  $N_2(C^3\Pi_u)$  [27]. The difference in the energy-threshold for the excitation and ionisation by electron-impact is leveraged to probe the EEDF. This method fails in helium gas mixtures, where Penning ionisation by helium metastables ( $\text{He}^*$ ) overtakes the electron-impact ionisation [61]. Nonetheless,  $N_2(C^3\Pi_u)$  and  $N_2^+(B^2\Sigma_u^+)$  densities are useful to probe the presence of energetic electrons and the  $\text{He}^*$  density, respectively.



# Chapter 3

## Methodology

Plasma-based nitrogen fixation is studied in two different plasma setups. In section 3.1, an atmospheric plug-flow RF plasma setup is presented. This reactor is used to study the formation of  $\text{NH}_3$  in a  $\text{He}/\text{N}_2/\text{H}_2$  gas mixture. The gas flow between the two planar electrodes is described as a *plug flow*, where a one-dimensional gas flow fixes the relation of time and the spatial dimension along the gas flow as  $x = vt$ .

A low-pressure capacitively coupled RF plasma is used to study the composition of a surface that is in direct contact with a plasma, see section 3.2. A different reactor design is used to study the surface composition. A low-pressure capacitively coupled  $\text{N}_2/\text{O}_2/\text{H}_2$  plasma is in direct contact with the substrate under study. This plasma is well understood and studied in literature [44]. Therefore, the research can focus on investigating the surface composition.

### 3.1 Atmospheric Plug-Flow RF Plasma

The gas conversion of a plasma catalytic reactor is studied with an atmospheric RF discharge. This setup is already previously used for *in situ* measurements on  $\text{CO}_2$  dissociation and volatile organic component (VOC) removal [92, 116–118]. Figure 3.1a gives a schematic of the setup. The schematic includes the gas lines and electrical connections. Massflow controllers (MKS) control the gas flow, which is obtained from a 20L He bottle (99.999%, Air Liquide), 20L  $\text{N}_2$  bottle (99.999%, Air Liquide), and a 1L  $\text{H}_2$  can (99.999%, Messer). A vacuum compartment isolates the reactor from the outside. A scroll pump (MVP 055-3, Pfeiffer) maintains a sub-mbar pressure that is monitored with a Pirani gauge (TPR 280, Pfeiffer). The gas composition of the exhaust is measured in a multipass cell (A136/2-LT, Bruker). The cell is installed in the sample compartment of the FTIR spectrometer (Vertex 70v, Bruker) and its temperature controlled to 180 °C.

The reactor is isolated from the environment by the vacuum compartments. This prevents impurities seeping into the gas stream. Ideally, the pressure is below 0.1 mbar. When the pressure gets too high, then a plasma might ignite around the housing. The occurrence of such a parasitic discharge sets the upper limit of the vacuum compartment pressure to roughly 1 mbar.

The reactor is designed to isolate the gas stream inside the reactor from the vacuum compartment, while giving optical access to the plasma. A front view of the

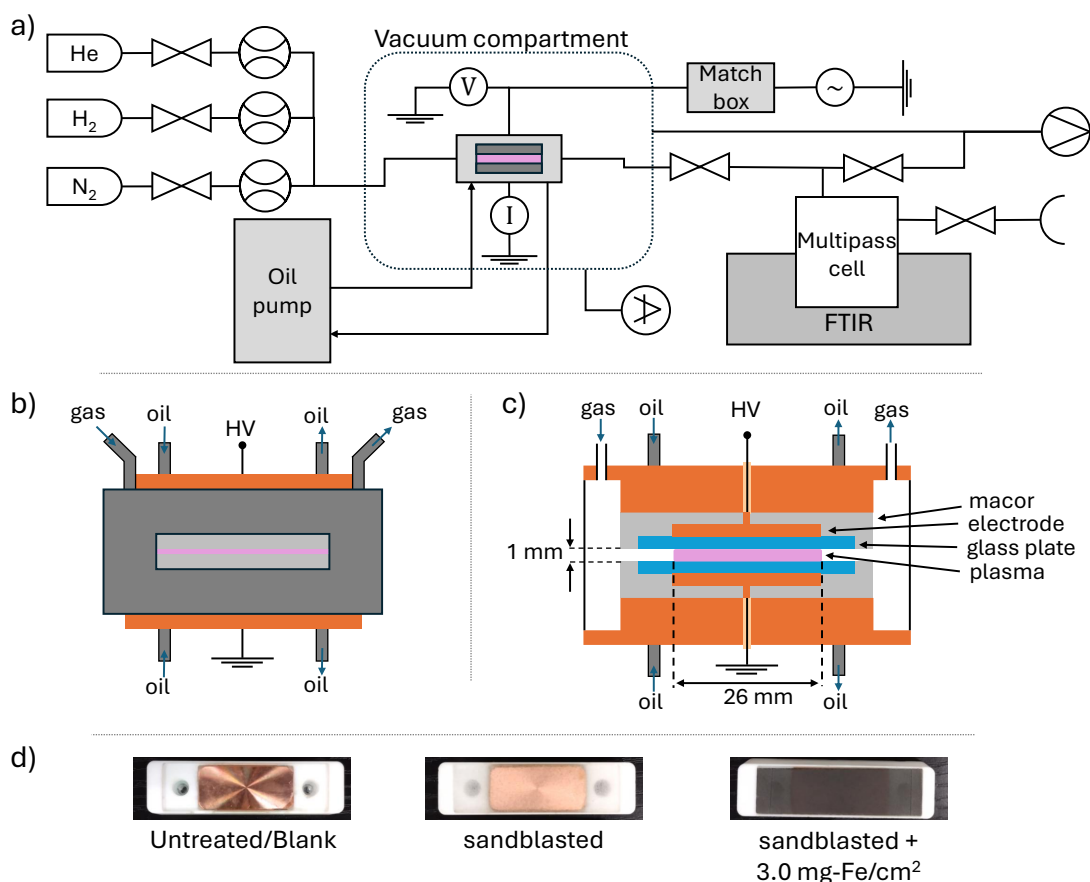


Figure 3.1: A schematic of the experimental setup with an oil based temperature control (a), a sketch of the front view of the reactor (b), a cross-sectional sketch of the front view of the reactor (c), and photos of the glass plate + electrode installed in the macor block for different coatings (d).

reactor is sketched in figure 3.1b. The gas is confined by an aluminium housing that is electrically grounded. The housing incorporates the gas line connections and quartz windows. These windows give optical access to the plasma in the visible part of the electromagnetic spectrum.

The plasma emission is studied with optical emission spectroscopy. The light is captured using an optical fiber (03345-REV.B, CeremOptec) that is placed in front of the reactor. The light is spectrally resolved using a spectrograph (SR-750-B1, Andow) and collected by an intensified charge-couple device (ICCD) camera (ISTAR-SCMOS-14U-E4, Andor). This simplistic setup captures the light emitted from the center of the discharge with a diameter of 4 to 5 mm.

Copper blocks are mounted at the bottom and top of the housing to complete the gas confinement. The electrodes are insulated from these blocks using custom Macor blocks and from the plasma using glass plates. This is visualised in the cross sectional view of subfigure 3.1c. The surface of these glass plates can be modified such that catalytic coating can be applied. Thereby, a catalyst can be introduced without significantly affecting the gas stream. Finally, the plasma is ignited between the glass plates, creating a homogeneous discharge with a volume  $26 \times 13 \times 1$  mm, as indicated by

the magenta rectangle.

The plasma is ignited using a RF generator (RFG100-13, Coaxial Power Systems). The impedance of the system is matched by a manual Impedance Matching network (MMN 50-600 W, Coaxial Power Systems). The voltage drop over the reactor and the current running through the reactor are measured close to the reactor itself, inside the vacuum compartment. This is further discussed in section 3.1.1.

The temperature of the reactor is controlled using an heating system. A silicon based oil (Thermal H20S, Julabo) is heated in a thermostatic bath (RE415S, Lauda). Temperatures up to 200 °C can be reached, which is below the flash and fire point of the fluid. The fluid flows through the aforementioned copper blocks. Thereby, the gas temperature is controlled by controlling the temperature of the housing. The experiments are operated at 20 °C, unless otherwise mentioned.

### Catalytic coating

Different glass plates are used during the experiments. An untreated glass plate, a sandblasted, and a sandblasted plate that is also spray-coated with iron nanoparticles are presented in figure 3.1d. The untreated glass plates are used for the *blank experiment*. In heterogeneous catalysis, such an experiment determines the blank activity of a reactor, whereafter the activity of a catalyst can be determined [35]. In a plasma-catalytic reactor, the blank experiment checks the gas conversion by the plasma alone.

The catalyst is added in the form of nanoparticles. Such particles are known for their high surface area that maximise the catalytic activity. First, the glass plates are sandblasted, see middle glass plate in figure 3.1d. After which the catalytic material is spray coated on the plate [117, 119]. Sandblasting increases the surface roughness that ensures successful adhesion of the catalytic material. Spray coating is a common technique within the field of plasma catalysis. For instance, De Meyer et al. found that spray coating results in a higher NH<sub>3</sub> synthesis rate than wet-impregnation, which is another common coating technique [23].

Three different nano particles are used for the experiments: copper (25 nm diameter, Sigma-Aldrich), iron (35-45 nm diameter, Sigma-Aldrich), and platinum (200 nm diameter, Sigma-Aldrich). These metals effectively scan the binding energy of N to the surface. This is a critical parameter for thermally catalysing NH<sub>3</sub> [34]. Potential differences in NH<sub>3</sub> production will hint at the impact of typical catalytic reactions on the overall conversion.

The activity of a catalyst is directly proportional to the surface area that is exposed to the gas stream [120]. For a planar surface, this is very easy to derive as it equals to width times height. The calculation becomes more complicated for less defined surface such as a nano particle coating. Rather, the maximal specific surface area  $S_m$  is used as an approximation. It is expressed as a surface area enhancement factor  $\vartheta$ , which is the ratio of  $S_m$  over the wall area. Assuming that the nanoparticles are spherical, it is derived following the *loading* of the surface in mg cm<sup>-2</sup>, material density  $\rho_M$  in kg m<sup>-3</sup>, and particle *size* in nm as,

$$\vartheta = \frac{6 \cdot \text{loading}}{\rho_M \cdot \text{size}} \quad . \quad (3.1)$$

For the experiments, the surface is loaded with  $3.0 \text{ mg cm}^{-2}$  copper or iron or  $0.3 \text{ mg cm}^{-2}$  platinum that translates to a  $\vartheta$  of 800, 510-650, and 4.2, respectively. The surface enhancement factor for platinum is low compared to iron and copper. This difference in  $S_{act}$  must be considered when comparing the effectiveness between the catalysts.

### 3.1.1 Power Measurements

The plasma power is an important parameter that is directly related to the plasma density [121]. The voltage and current are measured using an in-house made IV-box that is sketched in figure 3.2a. The high voltage RF signal is applied by a coax cable. The shielding of this wire grounds the housing of the box. The box is placed close to the plasma reactor ( $\sim 5 \text{ cm}$ ), inside the low-pressure compartment, to improve the accuracy of the measurement, e.g. by minimising ohmic losses inside the cables. In figure 3.2b, an equivalent electrical circuit is given. This is useful to relate the measurable  $u_{voltage}$  and  $u_{current}$  to the actual plasma voltage  $u_{plasma}$  and current  $i_{plasma}$ .

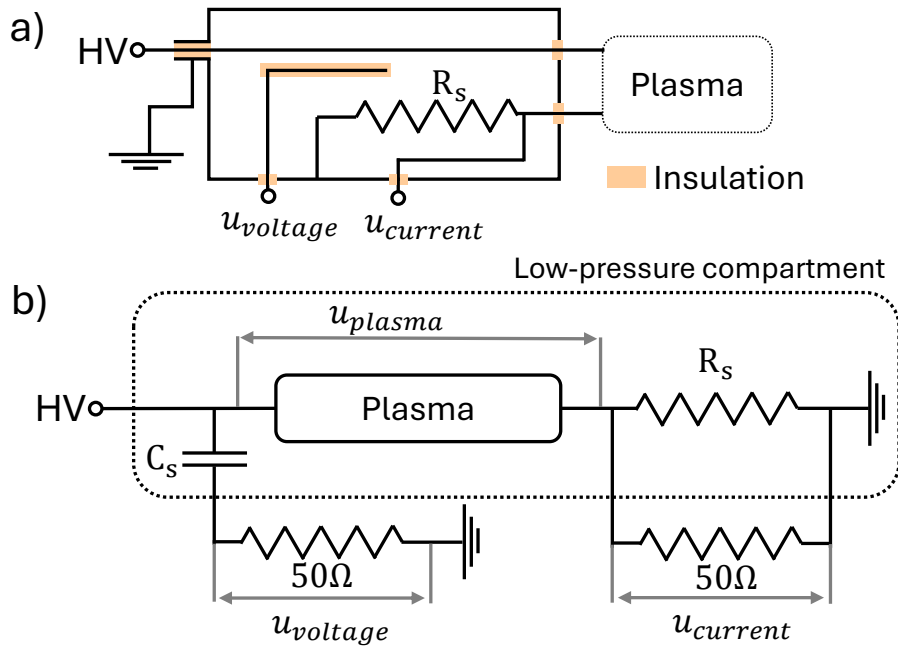


Figure 3.2: A schematic of the IV-box (a) that is used to measure the plasma power and the corresponding electrical circuit (b).

The amplitude of the high voltage applied to the plasma is reduced with a voltage-divider. A capacitor  $C_s$  is placed in series with the termination resistor ( $50 \Omega$ ). The capacitor is created by installing a wire at a fixed distance from the high voltage (HV) wire. This wire is insulated to prevent accidental short-circuiting the circuit. Following the straightforward arithmetic, the relation between  $u_{plasma}$  and  $u_{voltage}$  is obtained.

$$u_{plasma}(t) \approx \frac{1}{\omega R_{term} C_s} e^{-j\pi/2} u_{voltage}(t) \quad (3.2)$$

where  $u_{voltage}(t) = \tilde{u}_v \cos(2\pi f_{RF}t - \varphi_v)$  with the measured amplitude  $\tilde{u}_v$  and phase  $\varphi_v$ . The factor  $\frac{1}{\omega R_{term} C_s}$  is obtained from a calibration measurement. There,  $u_{plasma}$  is directly measured using a high-voltage probe and compared to the measured  $u_{voltage}$  signal.

The current through the plasma  $i_{plasma}$  is derived from measuring the voltage drop  $u_{current}$  over a known resistor  $R_s$  as,

$$i_{plasma}(t) = \left( \frac{1}{R_s} + \frac{1}{50\Omega} \right) u_{current}(t) \quad . \quad (3.3)$$

where  $u_{current} = \tilde{u}_c \cos(2\pi f_{RF}t - \varphi_c)$  with the measured amplitude  $\tilde{u}_c$  and phase  $\varphi_c$ .

The plasma power follows from the time average of the energy consumed per cycle as function of the phase difference  $\Delta\varphi = \varphi_c - \varphi_v$ ,

$$p_{plasma} = \frac{1}{2} \tilde{u}_p \tilde{i}_p \cos\left(\frac{\pi}{2} + \Delta\varphi - \varphi_{ref}\right) \quad . \quad (3.4)$$

The phase difference must also correct for the shift inherent to the setup, i.e. reference phase shift  $\varphi_{ref}$ . This arises mainly from a difference in the cable length of the current and voltage channels.  $\Delta\varphi - \varphi_{ref}$  should be zero when the plasma is off. Hence, before each measurement,  $\varphi_{ref}$  is set to the measured  $\Delta\varphi$ .

A power-sweep provides the necessary data to check if the reference phase shift is correctly estimated. If  $\varphi_{ref}$  is incorrect, then the apparent plasma power will monotonously increase when the plasma is off. Luckily, the observed power slope can be used to obtain the correct  $\varphi_{ref}$ , by varying the reference phase shift until the slope equals zero. The voltage calibration factor can be verified by comparing the power-sweep to that of earlier measurements.

### 3.1.2 Ex-Situ FTIR Absorption Spectroscopy

Ammonia production is studied by admixing a small amount of  $N_2$  and  $H_2$  to a helium gas stream. Only a small amount of ammonia is expected in the gas stream. Molar fractions up to 0.8% are observed in pure atmospheric  $N_2+H_2$  plasmas [22, 25]. Molar fractions as high as 80 ppm can be expected for our experiments, when extrapolating to the helium diluted gas mixtures. Therefore, a highly sensitive technique is needed to observe the plasma produced  $NH_3$ .

The sensitivity of IR absorption spectroscopy is fixed by the optical path length. *In-situ* measurements are limited by the reactor design. This limits the path length to 1 to 2 cm. yielding a lower detection limit of 100 ppm. The expected molar fractions are below this lower limit, thus it is not possible to perform *in-situ* measurements. Instead, the gas composition of the plasma effluent is analysed. The exhaust is connected to a multipass cell. Its path length is increased to 6.4 m so the lower detection is lowered to 0.5 ppm, which is sufficient for our measurements.

#### Identifying plasma products

The gas composition in the multipass cell is analysed using FTIR absorption spectroscopy. Figure 3.3 gives two typical spectra that are obtained during a typical experiment after a) 10 minutes and b) 90 minutes of plasma operation. The MIR spectral

region shows contributions of  $\text{CO}_2$  around  $670\text{ cm}^{-1}$  (bending mode) and  $2350\text{ cm}^{-1}$  (asymmetric stretch mode),  $\text{H}_2\text{O}$  between  $1250$  and  $2050\text{ cm}^{-1}$ , and the plasma products:  $\text{NH}_3$ ,  $\text{N}_2\text{O}$ , and  $\text{CO}$ . The signal of  $\text{CO}_2$  and  $\text{H}_2\text{O}$  originate from the open air path between the spectrometer and multipass cell, since they are naturally present in air. The IR absorption by the plasma products is simulated and plotted in the subfigures with an 0.5% offset.

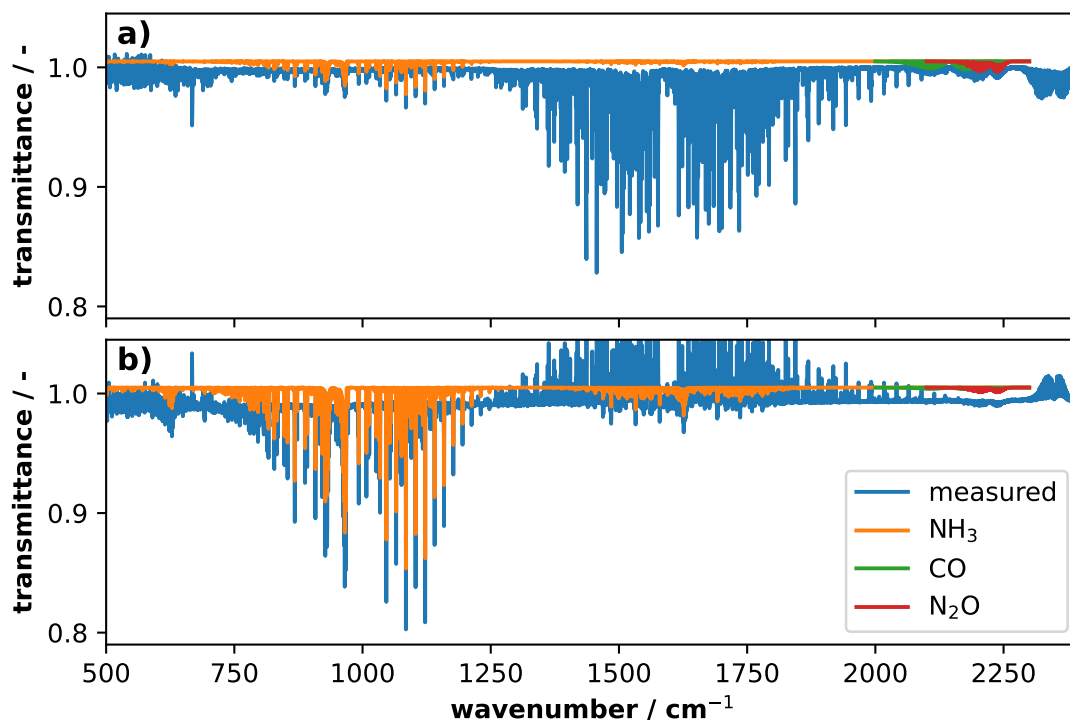


Figure 3.3: A typical FTIR spectrum obtained 20 min (a) and 90 min (b) after igniting the plasma, which is operated at 4 W, with 0.125 sccm  $\text{N}_2$ , 2.375 sccm  $\text{H}_2$ , and 250 sccm He.

The vibrational spectrum of  $\text{CO}$  is the simplest to describe among the plasma products. It is a diatomic molecule, thus it has only one vibrational mode centred around  $2140\text{ cm}^{-1}$ . Nitrous oxide ( $\text{N}_2\text{O}$ ) has two vibrational modes: N-O stretch around  $1350\text{ cm}^{-1}$  and N-N stretch around  $2220\text{ cm}^{-1}$ . The latter is observed during the experiments since it is more IR active and does not overlap with the strong  $\text{H}_2\text{O}$  absorption features. The absorption features of  $\text{CO}$  and  $\text{N}_2\text{O}$  partially overlap. Therefore, the contribution of  $\text{CO}$  is fit from  $2005$  to  $2175\text{ cm}^{-1}$  and  $\text{N}_2\text{O}$  from  $2175$  to  $2253\text{ cm}^{-1}$ .

Ammonia is a pyramidal tetratomic molecule that has four IR active vibrational transitions [122]. In the presented spectral range, vibrational transitions of the symmetric ( $\nu_2$ ) and asymmetric bending ( $\nu_4$ ) modes are observed. Namely,  $\nu_2=2\rightarrow 1$  around  $630\text{ cm}^{-1}$ ,  $\nu_2=1\rightarrow 0$  around  $930$  and  $965\text{ cm}^{-1}$ , and  $\nu_4=1\rightarrow 0$  around  $1630\text{ cm}^{-1}$ . The  $\nu_2=1\rightarrow 0$  is well isolated from the other spectral contributions and it is the most IR active mode. Thus, the ro-vibrational transitions observed between  $800$  and  $1200\text{ cm}^{-1}$  will be used to estimate the  $\text{NH}_3$  concentration.

## Calibration

Gas phase densities are readily obtained with IR absorption spectroscopy, once the path length is known. The path length is calibrated using a known CO<sub>2</sub>/He gas mixture. CO<sub>2</sub> is very active in the MIR spectrum and it is inert, unlike NH<sub>3</sub>. The asymmetric stretch vibration is the most observed band, e.g. see [79, 123]. Yet, this band is saturated under the used conditions. On top of this, CO<sub>2</sub> from the open-air path between the spectrometer and the multipass cell contributes to the spectrum as well. Its fraction in air varies in time such that it interferes with the experiments.

Therefore, the  $\nu_1 + \nu_2$  vibrational stretch around 2075 cm<sup>-1</sup> is used. The ro-vibrational lines are fitted to a synthetic spectrum that gives the molar fraction of CO<sub>2</sub>. A typical spectrum is given in figure 3.4a. The measured spectrum shows a good agreement with the synthetic best-fit spectrum. Sharp lines at 2018, 2040 and 2065 cm<sup>-1</sup> are associated to H<sub>2</sub>O, which originate from the humidity in the open-air optical path as previously mentioned.

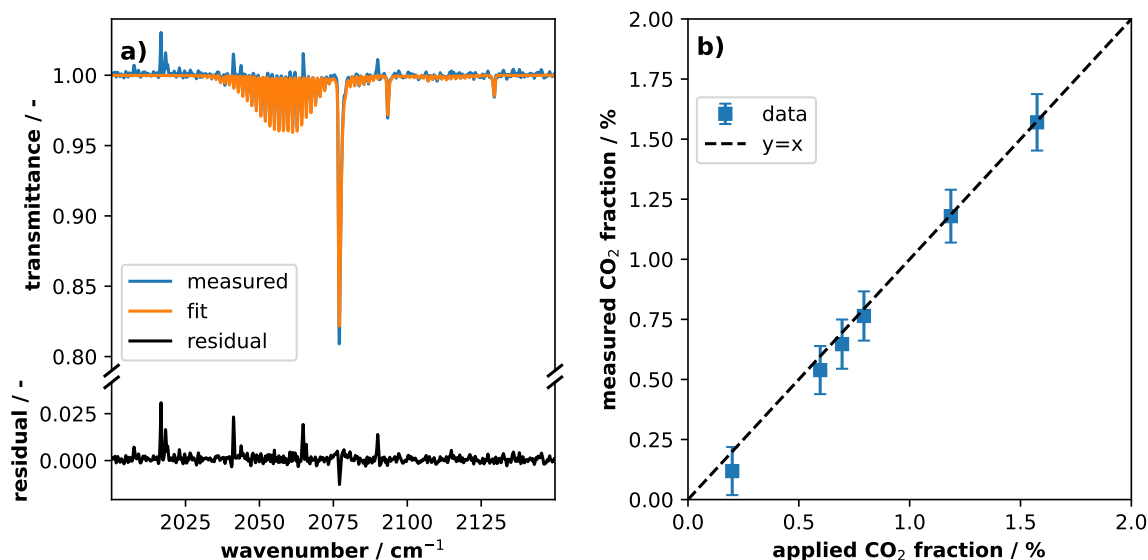


Figure 3.4: A typical FTIR spectrum obtained when applying 0.73% of CO<sub>2</sub> to the gas stream (a) and the measured vs applied molar fraction of CO<sub>2</sub> (b), when controlling the multipass cell temperature to 300 K.

The measured CO<sub>2</sub> molar fraction is plotted as a function of the applied molar fraction in figure 3.4b. The measured fractions are calculated assuming a path length of 6.4 m. The applied fraction is controlled by changing the gas flow ratio of CO<sub>2</sub> to He. The data points lie on the  $y = x$  line, thereby validating that the path length is indeed 6.4 m.

## 3.2 Low-Pressure Open RF Plasma

The surface composition is an important yet not-well studied parameter in plasma catalysis. It can be in *operando* studied using IRRAS. In figure 3.5a, a sketch of

the overall experimental setup is presented. The plasma is operated at 8 mbar in a low-pressure compartment. The pressure of this compartment is monitored using a capacitance gauge (CMR 263, Pfeiffer) and controlled using a manual rotating valve and a scroll pump (MVP 055-3, Pfeiffer). The gas flow is regulated using massflow controllers (1179C series, MKS) using a control-unit (946 Vacuum System Controller, MKS). The gases are obtained from a 50L He bottle (99.999%, Air Liquide), 50L N<sub>2</sub> bottle (99.999%, Air Liquide), 20L O<sub>2</sub> bottle (99.998%, Air Liquide), 20L H<sub>2</sub> bottle (99.999%, Air Liquide), and 10L D<sub>2</sub> bottle (99.9%, Air Liquide).

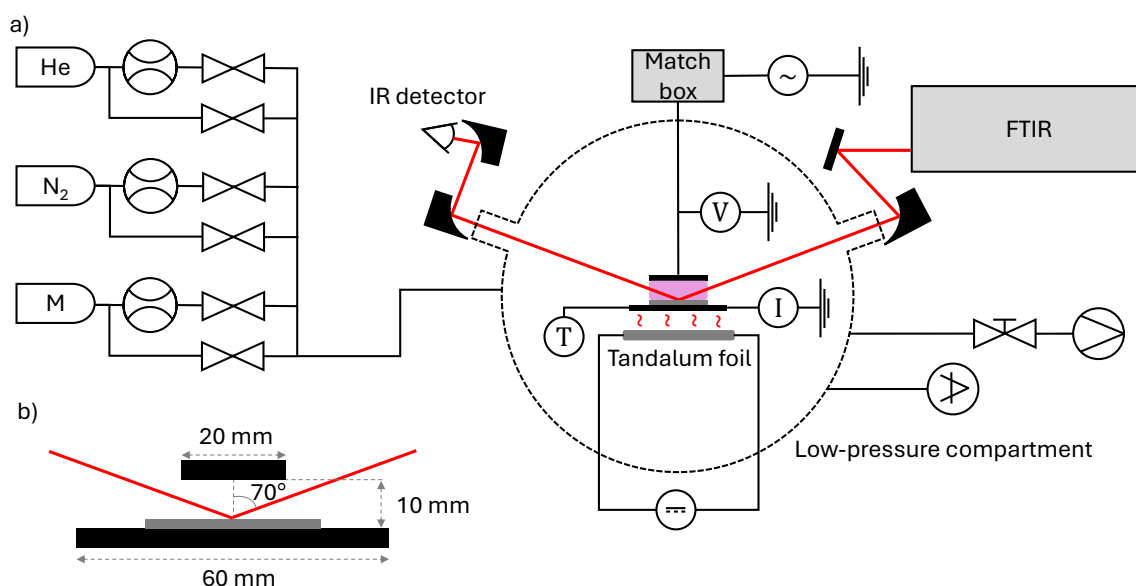


Figure 3.5: A sketch of the setup (a), where  $M=O_2$ ,  $H_2$ , or  $D_2$ . The electrode configuration (b) from the top view.

The IR beam is generated and spectrally resolved using an FTIR spectrometer (Vertex 70v, Bruker). It is guided towards the compartment and focussed on the substrate using gold coated mirrors. Two off-axis gold coated parabolic mirrors (250 mm focal point, II-VI GmbH) are used to focus the light on the substrate. The light is reflected at a 70° angle of incidence to maximise the sensitivity as seen in figure 2.7 in section 2.2.3. The light is collected and detected using an external LN-MCT Mid 24h detector (ID316, Bruker). The open-air paths between the spectrometer, low-pressure compartment, and the detector are isolated using plastic tubes and continuously purged with dry air. This minimises the presence of H<sub>2</sub>O(g) in the MIR spectrum.

The plasma is powered by an RF generator (RFG150-13, Coaxial Power Systems). The impedance is matched with a match box (MMN150-13, Coaxial Power Systems). The plasma power is measured similar to that in the plug-flow reactor. The IV-box of figure 3.2a is used with a minor adjustment. The high voltage wire inside the box is insulated instead of the capacitor-wire, since the box is placed in an atmosphere where the plasma easily ignites. This prevents the ignition of parasitic discharges inside the box. The rest, i.e. acquisition of waveforms and calculating the power, is identical as presented in section 3.1.1.

The low-pressure compartment is custom designed. It is well approximated by a cylinder with height 30 cm and a diameter of 25 cm. In figure 3.6, two snapshots of a

(Inventor) 3D drawing are presented from two different view points. The coordinate system is chosen such that the incoming IR beam moves in the positive x- and y-direction. Arms give optical access to the compartment. A KBr-window is placed in the arms where the IR beam enters and exists the compartment. A quick access door with a glass windows is installed in the front (+y-direction). The top is closed with a CF flange. The gas inlet, outlet, and purge are positioned on the bottom of the reactor. The inlet is in-front of the plasma and the outlet is behind the plasma in the xy-plane, see subfigure 3.6b. The reactor can be purged with ambient air, whereafter the front window-door can be opened to gain access to the reactor.

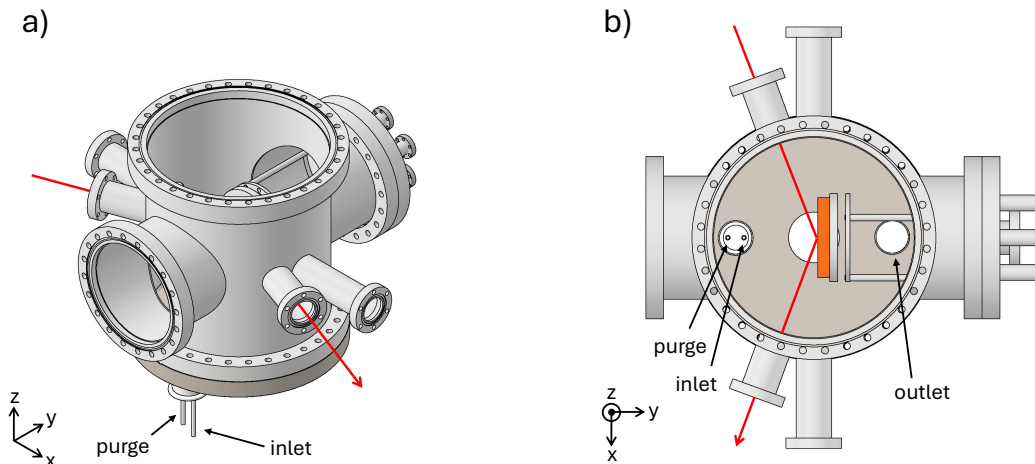


Figure 3.6: Snapshot of the lateral side of the reactor from an isometric (front-top-right) viewpoint<sup>1</sup> (a) and top viewpoint (b). The IR beam is included in red.

An open-plasma configuration gives optical access to the plasma and the substrate under study. The copper electrodes are placed 10 mm apart from each other using custom Macor blocks. The substrate is placed on the grounded electrode. The temperature is monitored using a thermocouple, which is mounted on the grounded electrode, and controlled by the thermal radiation originating from a Tantalum foil.

The plasma volume is much smaller than the vessel, so the plasma is well isolated from the housing, by at least 10 cm. Therefore, it is unlikely that the plasma directly interacts with the housing. In addition, plasma products can freely diffuse into the non-plasma part of the vessel. The total optical path length is approximately 42.6 cm including 2.1 cm of the plasma regime. This is sufficiently long to detect gas species with a density in the order of  $10^{13}\text{cm}^{-3}$ . Thus, gas phase absorption features inside the reactor must be considered as well as absorption on the surface .

### 3.2.1 IR Reflection Absorption Spectroscopy

Reflection absorption spectroscopy relies on a reflective surface from which the light specularly reflects. The changes in the reflectance  $R = I/I_{ref}$  are presented as the *absorbance*  $A = -\ln(I/I_{ref})$ . The measured spectrum  $I$  is normalised by a reference spectrum  $I_{ref}$  taken prior to the experiment. In this way, a positive absorbance signal

<sup>1</sup>Snapshots are taken from the Inventor 3D-drawing made by Kai Fiegler.

generally indicates the formation of either a surface group or gaseous species, a negative indicates the removal or disappearance.

Similar to typical FTIR absorption spectroscopy, the spectra contain absorption features of gas phase species as well. Since the observed absorption features are very small, the fitting procedure may be simplified. The observed spectrum  $R_{obs}$  is compared to a synthetic reference spectrum  $R_{ref}$  that is calculated using the HITRAN database for a given reference density  $n_{ref}$ . Following the Beer-Lambert law, the intensity of the overall spectrum can be changed following equation 3.5 to obtain the observed spectrum  $R_{obs}$ . This gives the actual density  $n_{act}$ .

$$R_{obs}(\tilde{\nu}) = R_{ref}(\tilde{\nu})^{n_{act}/n_{ref}} \quad (3.5)$$

Changes in the surface composition are expected to yield only small changes in the absorbance. The signal-to-noise ratio must be minimised such that an absorbance signal of 0.01% can be observed. This is achieved by using a 24h stable MCT detector. This detector can be cooled continuously for days that contributes to a stable signal. In addition, the spectral resolution is lowered to  $2 \text{ cm}^{-1}$ . This averages the spectrum in the spectral domain. It also allows for acquiring more spectra withing a given time span, since the acquisition time per spectrum is shortened. Some spectral features inherent to the detection method persist. They must be either experimentally or digitally removed.

### Icing peak

When cooling the MCT detector from room temperature, a broad peak around 3000 to 3600  $\text{cm}^{-1}$  may appear over time. In figure 3.7a, a spectrum is plotted that shows such a peak. This spectral features must be avoided when experimenting with  $\text{NH}_x$  formation on the surface, as it overlaps with the reported stretch modes of these intermediates around 3300  $\text{cm}^{-1}$  [104]. The intensity of this feature is integrated and plotted in time in subfigure 3.7b. The trend shows a time constant of 53 min, thus several hours are needed before the signal stabilises.

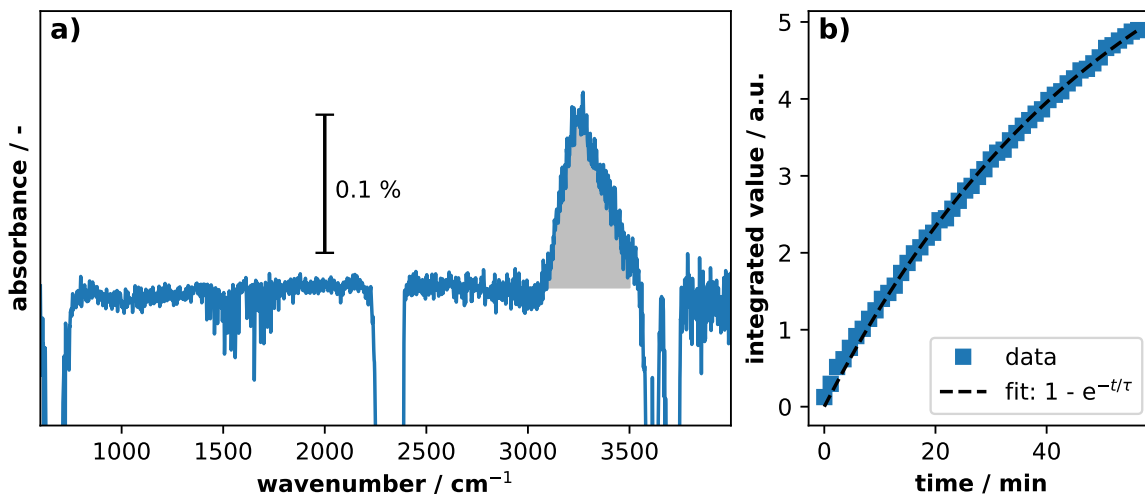


Figure 3.7: A spectrum (a) obtained 1 minute after the reference spectrum. The integrated part of the peak is highlighted by grey and the value is plotted in time (b).

Its impact is related to the humidity of the air inside the lab. The humidity of the air near the MCT sensor freezes and forms a thin ice layer directly on the detector. Generally, this spectral contribution can be avoided by cooling the detector a day (or more) in advance. In other words, the “icing” peak has time to stabilise before the experiments are performed.

### Pre-processing spectra

The spectra are digitally processed before they are analysed. The IR beam passes through a purged air path, which connects the FTIR spectrometer to the low-pressure vessel and the vessel to the IR detector, see figure 3.5. Air naturally contains small amounts of  $\text{H}_2\text{O}$  and  $\text{CO}_2$  that are very IR active. Their absorption features are digitally removed using reference spectra. This is illustrated in figure 3.8.

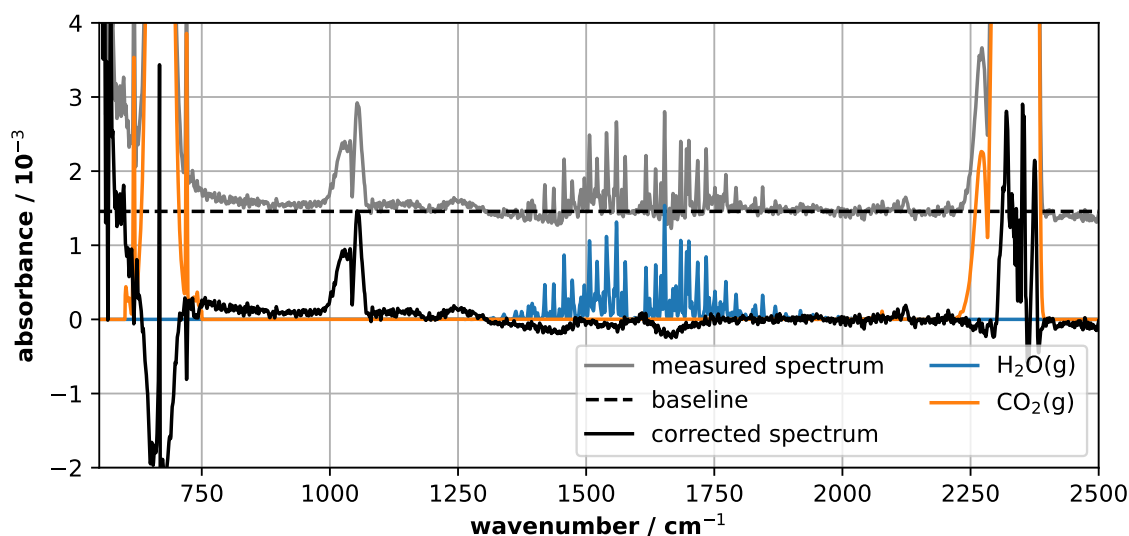


Figure 3.8: The adjustments made to the measured spectrum obtained when igniting a  $\text{O}_2$  plasma.

The *measured spectrum* is first corrected for a baseline shift. A 0th-order polynomial is fitted to the “empty” parts of the spectrum, see *baseline*. Higher order polynomials ( $> 1$ ) must be avoided as they might introduce broad features that can be mistaken for absorption features associated to the substrate. A synthetic spectrum of  $\text{H}_2\text{O}(\text{g})$  is calculated using the HITRAN database, where the code of the  $\text{NH}_3$  *plug flow* measurements is used. The sharp ro-vibrational lines of  $\text{H}_2\text{O}$  are very distinct in the spectrum, unlike the broad surface associated bands. Therefore, by examining the spectral derivative to the wavenumber  $\partial A/\partial \tilde{\nu}$ ,  $\text{H}_2\text{O}(\text{g})$  feature is readily identified in, fitted to, and removed from the measured spectrum.

Similarly, the absorption features of  $\text{CO}_2(\text{g})$  are removed. It is difficult to calculate a synthetic spectrum that accurately describes the observed features. The density of  $\text{CO}_2(\text{g})$  is not reduced in the open-air path length, unlike that of  $\text{H}_2\text{O}(\text{g})$  by using dry air. The signal is seen in both the reference and measured spectrum. Thus, the approximation for the instrumental line shape of equation 2.22 of subsection 2.2.1 does not

hold. This introduces non-linear effects. Instead, a measured  $\text{CO}_2(\text{g})$  spectrum is used. The absorption by  $\text{CO}_2(\text{g})$  is minimised to a certain degree. This is sufficient to isolate a  $\text{Fe}_2\text{O}_3$  absorption band located around  $720\text{ cm}^{-1}$  and  $\text{N}_2\text{O}(\text{g})$  around  $2220\text{ cm}^{-1}$ .

Finally, after considering these spectral artefacts, IRRAS spectra can be obtained where changes can be attributed to changes on the substrate or gas phase of the vessel.

### 3.2.2 Pretreatment of Samples

IRRAS is a relative technique that only observes changes of the surface composition. The reflection spectra are a complex convolution of absorption features, which is difficult to analyse. The unique ro-vibrational structures common for gas phase species disappears once a molecule adsorbs, since it loses its rotational degree of freedom. Also, the central wavenumber of a vibrational transition shifts as a result of the binding to the surface, because the intermolecular binding energy changes [124]. This results in non-unique absorption features for surface groups.

On top of this, impurities on the surface and gas phase might introduce unexpected surface groups. A pristine metallic foil always contains carbon-impurities on top. This arises from chemical cleaning agents or reactions of  $\text{CO}_2$  and  $\text{H}_2\text{O}$  once in contact with air. The presence of hydrocarbons is especially important when studying  $\text{NO}_x$  formation, since it quenches adsorbed  $\text{NO}_x$  species [39, 40]. Hence, their presence must be avoided.

Therefore, it is important to pretreat the substrates in a consistent manner. The main goal of the pretreatment is to remove the impurities, such as hydrocarbons and carbonyl species, to simplify the surface chemistry and the interpretation of the IRRAS spectra. A plasma is ignited in a helium-rich gas stream with a 10% admixture of  $\text{O}_2$  or  $\text{H}_2$ . This plasma cleans at moderate conditions. Helium is added to increase the throughput of the reactor, by enhancing the removal of the impurities in the gas phase from the vessel. Also, it helps to ignite the plasma at moderate conditions, i.e. low heating. Oxygen and hydrogen are added to introduce a chemical cleaning agent through their radicals, e.g.  $\text{O}$  and  $\text{H}$ . The outcome of these pretreatment steps are discussed in the chapter 5 for each type of measurements.

# Chapter 4

## Ammonia Synthesis in an Atmospheric RF Discharge

Plasma catalysis is often studied using DBDs since catalyst can be easily introduced to the reactor. However, any enhancements in the  $\text{NH}_3$  production cannot directly be associated to plasma catalytic synergisms, since the plasma behaviour is strongly related to the surface morphology, e.g. see [25]. Therefore, another reactor configuration is used to separate the plasma operation from the surface morphology.

In this chapter,  $\text{NH}_3$  synthesis is studied in a capacitively coupled RF discharge in a  $\text{He}/\text{N}_2/\text{H}_2$  gas mixture at atmospheric pressure. This discharge is designed to simplify the plasma chemistry and maximise the impact of surface reactions on the overall chemistry. The helium rich gas stream ensures that the discharge ignites diffusely along the electrode and allows the gas gap to be reduced, which stimulates surface collisions of reactive species. This reactor is previously successfully used to study n-butane oxidation and  $\text{CO}_2$  dissociation [92, 116–118].

The experiments are combined with a global model to obtain a clear picture on the involved chemistry. The discharge dynamics are characterised by examining the power-to-voltage relation and with optical emission spectroscopy for the emission bands of  $\text{N}_2$ . The ammonia production is experimentally characterised by analysing the effluent of the discharge and performing a parameter scan. The results are compared to a global *plug flow* model of the chemistry. The outcome will inform us which processes are responsible for ammonia synthesis and the impact of a catalytic coating on the process.

The discharge conditions are controlled through varying the discharge power, reactor temperature  $T_{\text{reactor}}$ , and the  $\text{He}/\text{N}_2/\text{H}_2$  gas mixture. The latter is quantified using the  $\text{H}_2$ -to- $\text{N}_2$  gas flow ratio, expressed as  $f_{\text{H}_2} = \text{H}_2 / (\text{N}_2 + \text{H}_2)$ , i.e. the ratio of the  $\text{H}_2$  flow over the flowrate of  $\text{N}_2 + \text{H}_2$ . The  $\text{N}_2 + \text{H}_2$  admixture to the helium gas flow is similarly expressed as  $c_{\text{admix}} = (\text{N}_2 + \text{H}_2) / \text{He}$ , where the helium flow is kept at 250 sccm.

---

The contents of this chapter are based on the work previously published as Vervloedt and von Keudell Plasma Sources Science Technology 33 (2024) 045005 [91]

## 4.1 Discharge Dynamics

The discharge dynamics dictate the chemistry inside the reactor. For instance, energetic electrons are needed to dissociate stable nitrogen molecules, which have an energy threshold of 9.76 eV [125]. A higher electron density or reduced electric field  $E/N$  will increase the dissociation rate, thereby enhancing  $\text{NH}_3$  production. Conversely, the electron impact dissociation of  $\text{NH}_3$  increases as well. Hence, the plasma parameters must be carefully chosen to maximise the former and minimise the latter.

In this section, the discharge is characterised by examining the discharge power as function of the applied voltage and the emission spectra of nitrogen. The scaling laws of the electron dynamics are derived from these observations that are used for the kinetic model in section 4.3.

### Power-voltage curves

The discharge mode can be deduced from the relation of the discharge power to the applied root-mean-squared (rms) voltage [60, 121, 126]. Initially, the discharge ignites homogeneously along the discharge gap, which is referred to as the diffuse mode. When the discharge transfers to the constricted mode, the power will drastically increase [67]. This transition is typically observed at higher voltages in the COST-jet. In the plug flow reactor, the glass plates effectively prevent this transition. Instead, arcing is only observed once the glass plates break from the thermal stress induced by the plasma.

In figure 4.1a, the plasma-voltage curves are plotted for a pure helium discharge and for different  $\text{H}_2$ -to- $\text{N}_2$  gas ratios at  $c_{admix} = 1\%$ . The helium discharge is used to benchmark our reactor against the COST-jet [59]. The helium discharge ignites at 160 V. The discharge power increases linearly up to 250 V and quadratically for higher voltages. This is similar to the COST-jet, where it is attributed to the change in the discharge mode from  $\alpha$  to  $\gamma$  mode. The difference in our measurements is less apparent. This is likely due to the presence of the dielectric barrier, which suppresses mode transitions [126].

Introducing  $\text{H}_2$ ,  $\text{N}_2$ , or a  $\text{N}_2+\text{H}_2$  mixture to the gas stream introduces an overall positive voltage shift. Higher voltages are required to attain the same plasma power when changing from a pure helium plasma to  $f_{\text{H}_2}=100\%$  and  $c_{admix}=1\%$ . The same holds when gradually interchanging  $\text{H}_2$  with  $\text{N}_2$ . The slope of the curve does not show significant changes, thus no discharge transition is induced with including either  $\text{N}_2$  or  $\text{H}_2$ . The increase in the voltage is attributed to differences in the breakdown voltage of helium and hydrogen, and hydrogen and nitrogen. Therefore, introducing  $\text{H}_2$  and  $\text{N}_2$  to the plasma does not alter the discharge mode.

In figure 4.1b, the surface composition is changed for  $f_{\text{H}_2} = 95\%$  and  $c_{admix} = 1\%$ . This gas mixture is often used in the  $\text{NH}_3$  measurements. The glass plate is sandblasted and coated with iron, copper, and platinum nano particles. The potential impact of sandblasting is tested as well. The untreated glass plate is labelled as *blank*, since it serves as the non-catalytic reference condition. Changing the *blank* plate to a sandblasted and or coated plate shows no differences in the offset and the slope of the power-to-voltage curve. Therefore, the surface morphology does not significantly affect the discharge mode, thereby  $E/N$ .

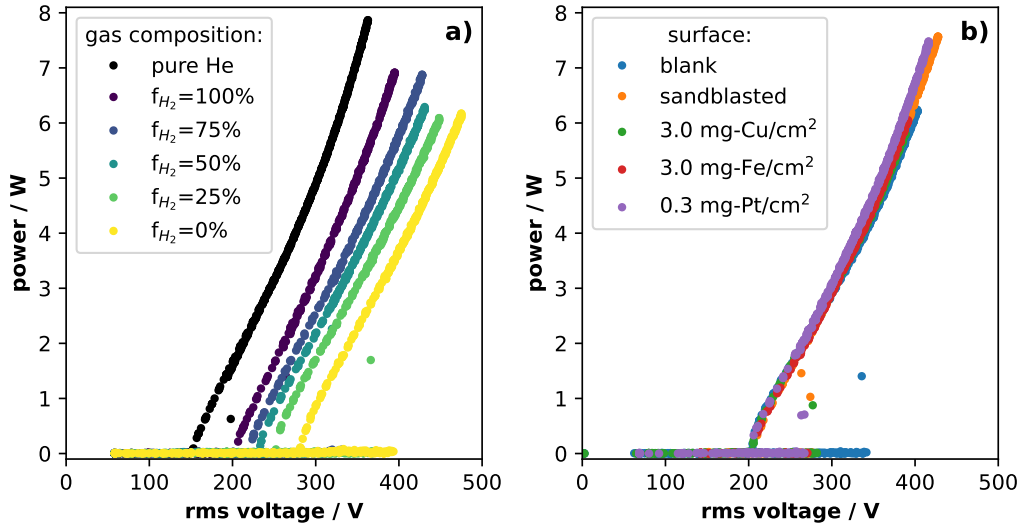


Figure 4.1: The power sweep plotted as the plasma power as function of the applied rms voltage at  $c_{admix}=1\%$  for varying  $f_{H_2}$  with the untreated glass plate (a) and for different surfaces for  $f_{H_2}=95\%$  (b).

These results show that both the gas mixture and surface composition do not affect the discharge mode. However, this does not directly translate to the discharge. Thus, in the next section, optical emission spectroscopy is employed to study potential differences in the excitation scheme of molecular nitrogen.

## N<sub>2</sub> emission

Molecular nitrogen is known for its strong emitting molecular bands. In our plasma, the second positive system (SPS)  $N_2(C^3\Pi_u \rightarrow B^3\Pi_g)$  and first negative system (FNS)  $N_2^+(B^2\Sigma_u^+ \rightarrow X^1\Sigma_g^+)$  are readily observable. The intensities of these bands are directly proportional to  $N_2(C)$  and  $N_2^+(B)$  densities, respectively. These densities are useful for characterising the plasma dynamics as is mentioned in section 2.3.

The excitation pathway of these excited states requires a careful consideration. A straightforward corona model quickly fails in the used discharge. However, the abundance of helium allows for some simplifications. The nitrogen admixture is kept to 1% and the atmospheric pressure quenches electronically excited species. Thereby, pooling reactions that produce  $N_2(C)$  are diminished. For this reason, the production of  $N_2(C^3\Pi_u)$  can solely be attributed to electron impact excitation reactions, where  $N_2$  is electronically excited from the ground state  $N_2(X)$  by electron impact. This requires relatively high energies of 11.0 eV [26, 127]. Thus, only electrons in the high-energy tail of the energy distribution are responsible for the production of  $N_2(C)$ . Conversely, this reasoning does not apply for  $N_2^+(B^2\Sigma_u^+)$ . Especially in helium rich gas mixtures, such as the applied gas mixture,  $N_2^+(B)$  is mainly produced through Penning ionisation by  $He^*$  [128, 129]. Therefore,  $N_2(C)$  and  $N_2^+(B)$  densities are respectively indicative to the presence of high-energy electrons and of  $He^*$ .

In figure 4.2, a typical emission spectrum is plotted that is obtained during the blank experiment for  $f_{H_2}=0\%$ ,  $c_{admix}=1\%$ , and power is 4 W. The band-head of the

vibrational transitions are labelled using the emission band (SPS or FNS) and the vibrational transition, where the transition from the upper to the lower vibrational level is given. For instance, the electronic-vibrational transition  $N_2(C^3\Pi_u, v = 0) \rightarrow N_2(B^3\Pi_g, v = 2)$  is observed at 380.6 nm and is labelled as SPS  $0 \rightarrow 2$ . The maximum intensities of each vibrational band are used to estimate the respective state.

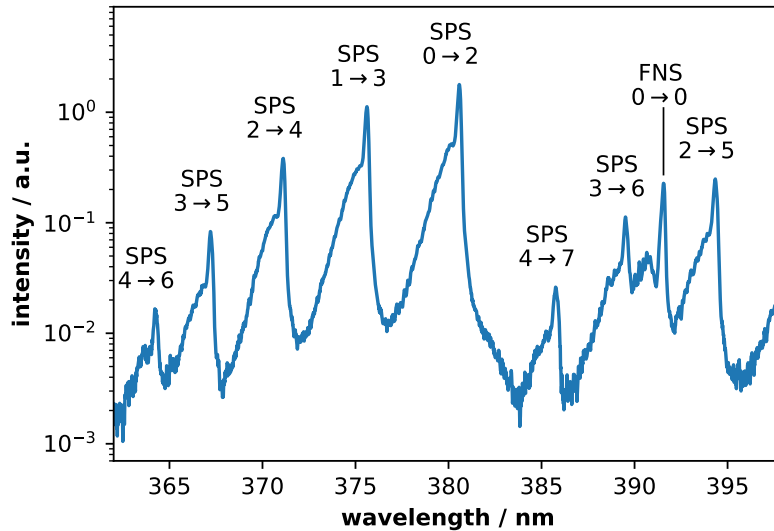


Figure 4.2: A typical emission spectrum obtained with the blank glass plate with  $f_{H_2}=0\%$ ,  $c_{admix}=1\%$ , and discharge power of 4 W.

The spectrum shows the emission of  $N_2(C, v)$  for vibrational levels  $v \leq 4$ . The density of  $N_2(C)$  is estimated from the summation of the  $\Delta v = v'' - v' = 2$  band of  $v'' = 0-4$ , which is seen from 362 to 382 nm. The densities of these vibrational levels is estimated from the maximum value of the respective band head. At 390.0 nm, the FNS is observed for the  $0 \rightarrow 0$  vibrational transition. This band overlaps with the neighbouring vibrational bands of SPS. It is the only observed vibrational transition, hence the  $N_2^+(B)$  density is estimated only from this vibrational transition. Thereby,

$$[N_2(C)] = \sum_{v=0}^4 [N_2(C, v)] \quad , \quad [N_2^+(B)] = [N_2^+(B, v=0)] \quad (4.1)$$

In figure 4.3, the  $N_2(C^3\Pi_u)$  and  $N_2^+(B^2\Sigma_u^+)$  fractions are plotted with increasing plasma power for different  $f_{H_2}$  at  $c_{admix}=1\%$ . Both the untreated and the Fe-coated glass plate are used. These densities are normalised to the total  $N_2$  admixture. A linear best fit is plotted for each gas mixture and glass plate. They are used as a guide for the eye to show the relation between these density ratios and the plasma power. No absolute calibration of the spectrograph was performed, thus only the changes as a result of changing the power, gas mixture, and surface coating are discussed.

Both densities increase linearly with the applied power. This follows the assumption that the power scales linearly with the electron density while electron energy distribution remains unaffected [130]. Therefore, the power scan will be modelled by linearly varying the electron density and keeping  $E/N$  constant in section 4.3.

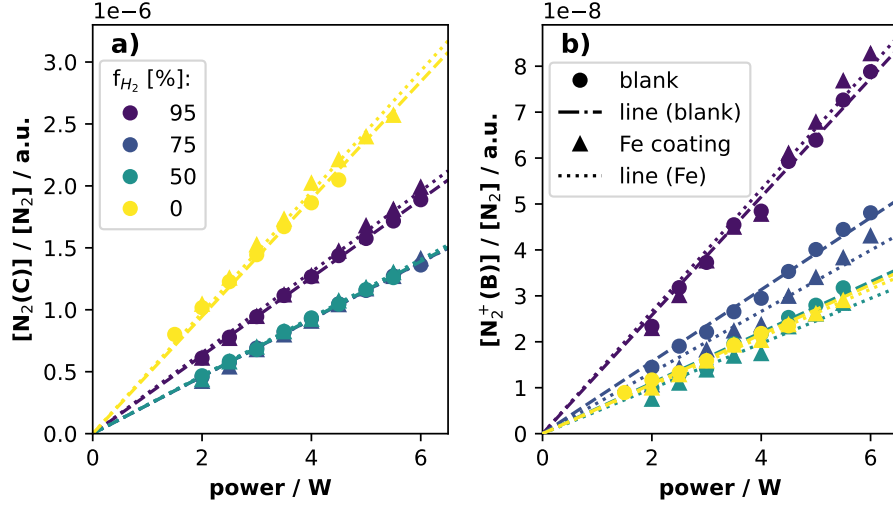


Figure 4.3: The normalised  $N_2(C^3\Pi_u)$  (a) and  $N_2^+(B^2\Sigma_u^+)$  (b) densities as function of the plasma power for different  $f_{H_2}$  values for  $c_{admix}=1\%$ .

The trend between  $[N_2(C)]/[N_2]$  and  $f_{H_2}$  shows two contributions. First, the decrease from  $f_{H_2}=0\%$  to  $75\%$  is attributed to a higher collisional relaxation rate of  $N_2(C)$  with  $H_2$  compared to  $N_2$  [131]. This is inherent in the system of observing the SPS and not related to the electron dynamics itself. Second, the increase from  $f_{H_2}=75\%$  to  $95\%$  is due to an increase in the presence of high-energy electrons, which agrees with EEDF calculations in [32] and will be mentioned later in section 4.3. This observation is important for the kinetic modelling as it indicates that mean electron energy increases with increasing  $f_{H_2}$ .

$[N_2^+(B)]/[N_2]$  increases with increasing  $f_{H_2}$ . This follows the typical relation of  $[He^*]$  with the  $N_2$  admixture [132]. This shows that the  $He^*$  density decreases with increasing  $N_2$  admixture to the gas flow.

The introduction of the Fe-coated glass plate introduces only minimal changes in the densities ratios. Differences are well within the uncertainty margin. Previously, the power-to-voltage curve did not change as well when changing the surface compositions. Therefore, the discharge dynamics do not significantly rely on the state of the surface. This will be used in the kinetic modelling by limiting potential differences in the electron density and EEDF between the blank and catalytic measurements.

To summarise, the following observation will be considered for the kinetic model: 1) the power linearly increases with electron density and  $E/N$  remains constant. 2)  $f_{H_2}$  affects the mean electron energy, which likely occurs due to a changing EEDF. 3) Introducing a catalyst does not significantly alter the discharge dynamics. This can be controlled in the model by constraining the electron density and  $E/N$  for the catalytic surface to that of the *blank experiment*.

## 4.2 NH<sub>3</sub> Density Measurements

The NH<sub>3</sub> concentration is obtained by measuring the gas composition of the effluent using multipass FTIR spectroscopy. It is expressed as the molar fraction in parts per million (ppm). The synthesis is characterised by measuring the fraction as function of the gas mixture and power. This is referred to as a *parameter scan*.

Ammonia readily physisorbs and desorbs from surfaces at room conditions, which is very similar to H<sub>2</sub>O. The observed NH<sub>3</sub> molar fraction, up to 40 ppm, are in the same order of magnitude as the capacity of the surfaces inside the multipass cell to store NH<sub>3</sub>. Thus, the interplay between the gas phase and the surface is significant and must be considered during data acquisition.

### Data acquisition

A typical NH<sub>3</sub> spectrum is shown in figure 4.4a, where the *measured*, *best fit* and *residual* spectra are plotted. The spectra are obtained with a multipass cell temperature  $T_{cell}$  of 180 °C. Slight changes in the baseline are already corrected for in the *measured* spectrum by fitting a second-order polynomial to 2450 to 2600 cm<sup>-1</sup>. This part of the spectrum shows no absorption features and is used as an indication for baseline fluctuations over time. The *best fit* is obtained following the fitting routine described in section 2.2.2 and describes the *measured* spectrum well. Minor differences are attributed to improper correction of the instrumental phase that arise when the phase resolution is too high as mentioned in section 2.2.1. Yet, this discrepancy has no impact on the resulting molar fractions.

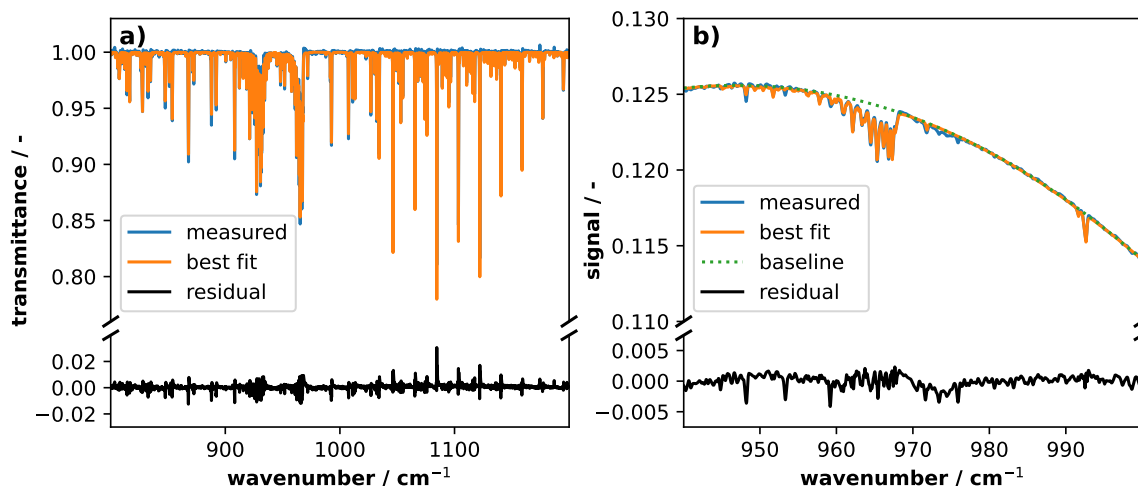


Figure 4.4: A typical measured ro-vibrational NH<sub>3</sub> spectrum together with the best-fit simulated spectrum and the residual of the best fit spectrum that is obtained at  $f_{H_2}=95\%$ ,  $c_{admix}=1\%$ , power of 4 W, and  $T_{cell}=180\text{ °C}$ (a). The reference spectrum is obtained before plasma ignition and contains NH<sub>3</sub> as well (b).

Additionally, the reference spectrum already showed the presence of NH<sub>3</sub> in the cell before igniting the plasma. This ammonia originates from prior measurements, where it adsorbed to the surfaces. It is unpractical to completely clean these surfaces

because every NH<sub>3</sub> molecule that is purged from the system must be replaced during the experiments, prolonging the acquisition time. Therefore, rather than fully cleaning the inner surfaces of the cell, NH<sub>3</sub> in the reference spectrum is quantified.

In figure 4.4b, the *measured* signal of the reference spectrum is plotted. Only a small part of the overall absorption spectrum (940 to 1000 cm<sup>-1</sup>) is used to estimate the concentration of NH<sub>3</sub>. This simplifies the required description of the baseline. The baseline is approximated by a fourth-order polynomial and derived using the empty parts of the spectrum, see *baseline*. With this baseline, a typical transmittance spectrum can be constructed and fitted, see *best fit* and *residual*. The molar fraction following this fit is added to the fractions obtained during the experiment.

Figure 4.5 presents the molar fractions of the observed plasma products in time. Nitrous oxide (N<sub>2</sub>O) and carbon monoxide (CO) are produced next to NH<sub>3</sub>, as presented earlier in figure 3.3. The plasma is ignited at 0.0 min. N<sub>2</sub>O and CO immediately appear in the cell after igniting the plasma. Their molar fractions decrease after 15 minutes, which indicates that they originate from impurities inside the system.

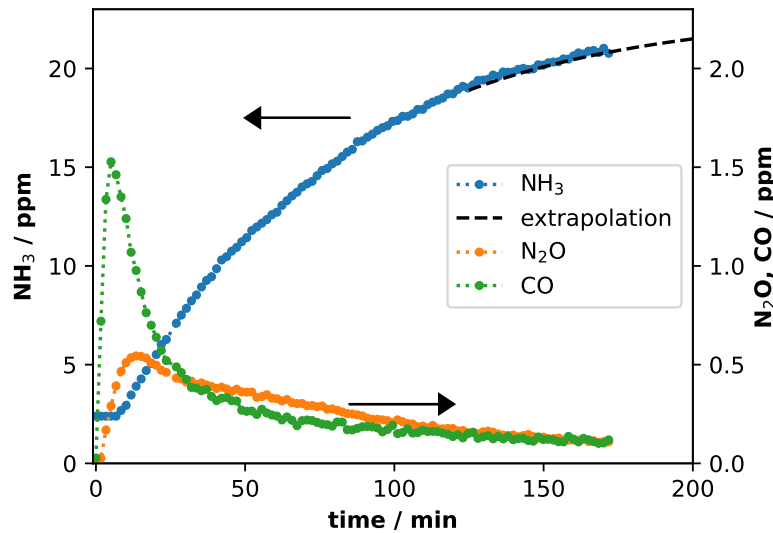


Figure 4.5: The molar fractions of NH<sub>3</sub>, N<sub>2</sub>O, and CO in time that are obtained when igniting the discharge for  $f_{H_2}=95\%$ ,  $c_{admix}=1\%$ ,  $p=4\text{ W}$ , and setting  $T_{cell}=180\text{ }^\circ\text{C}$ .

N<sub>2</sub>O and CO densities respond much faster than NH<sub>3</sub> when igniting the plasma. Their formation is associated to the removal of carbon and oxygen containing impurities inside the plasma reactor. The surfaces inside the reactor are gradually cleaned from any impurities, e.g. through sputtering by helium species. Unlike ammonia, these products do not interact with surfaces. Thus, they follow the relations expected from a 0D continuity equation. Furthermore, N<sub>2</sub>O is likely produced in the effluent as well, since the nitrous oxide density overtakes that of CO after 30 minutes. Molecular oxygen might persist in the gas stream (e.g. from the gas bottle itself) and could oxidise the adsorbed NH<sub>3</sub>. Other nitrogen oxides are not observed due to the low oxygen gas mixtures. Finally, the contribution of N<sub>2</sub>O and CO are omitted when discussing the plasma chemistry, because their concentrations are  $\ll 1\text{ ppm}$  when NH<sub>3</sub> finally reaches a stable value.

The  $\text{NH}_3$  molar fraction has an offset, time delay, and a much longer time constant to grow than  $\text{N}_2\text{O}$  and  $\text{CO}$ . The origin of the offset is already discussed. The time delay between ignition and the increase in the  $\text{NH}_3$  concentration arises from the physisorption inside the tubes that connect the reactor to the multipass cell. Once these surfaces are saturated, the density of the cell increases.

The time constant of the  $\text{NH}_3$  molar fraction is significantly longer than the expected value from a 0D continuity equation, unlike the inert species  $\text{N}_2\text{O}$  and  $\text{CO}$ . This is attributed to the interplay between physisorption-adsorption as  $\text{NH}_3$  readily adsorbs. Surfaces inside the cell need to be saturated with  $\text{NH}_3$  before this effect cancels. Only the stable concentration represents the molar fraction exiting the reactor. Therefore, an acquisition time in the order of several hours is required for each condition.

The acquisition time is shortened by extrapolating the observed trends using a typical exponential function:  $[\text{NH}_3] \propto [\text{NH}_3]_{fin} (1 - e^{-t/\tau})$ , where the time constant  $\tau$  and equilibrium fraction  $[\text{NH}_3]_{fin}$  are fit parameters. This final density is representative of the ammonia produced by the plasma, hence is the desired result. However, this relation is only an approximation. The binding energy of  $\text{NH}_3$  to the surface decreases with increasing  $\text{NH}_3$  surface coverage [133]. A multi-exponential function is needed to accurately describe the full time domain, but such an analysis will over-interpret the data. The presented single exponential holds only when considering the last 50 minutes of plasma operation.

Furthermore, the interplay with the surface is reduced by increasing the multipass cell temperature to  $180^\circ\text{C}$ . This is below the required temperature to dissociate  $\text{NH}_3$  [134]. The desorption rate increases with the surface temperature following equation 2.9 in subsection 2.1.2. This lowers the steady-state surface coverage of  $\text{NH}_3$ . As a result, the interplay of gaseous  $\text{NH}_3$  with the surface is lowered.

In summary, the ammonia production is measured *ex situ* in a multipass cell. This gives an accurate description of the  $\text{NH}_3$  molar fraction produced by the plasma. Impurities that are initially present in the reactor are removed during the first 30 minutes of plasma ignition. Thus, they do not play a role in the concentrations presented next.

## Parameter study

In figure 4.6, the molar fraction of  $\text{NH}_3$  is plotted for 3 parameter variations: a)  $f_{\text{H}_2}$ , b)  $c_{admix}$ , and c) power. Unless varied, these parameters are set to  $f_{\text{H}_2}=95\%$ ,  $c_{admix}=1\%$ , and power=4 W. The repeatability of the measurements is estimated by repeated measurements at  $(f_{\text{H}_2}, c_{admix}, \text{power}) = (95\%, 1\%, 4 \text{ W})$  for 8 times. The measurements show that the experiment is repeatable within 2.5 ppm

The efficiency of  $\text{NH}_3$  production is quantified with the hydrogen-to-ammonia conversion ratio  $\chi_H = \frac{3[\text{NH}_3]_{out}}{2[\text{H}_2]_{in}}$  and the energy yield (EY).  $\chi_H$  is plotted for varying the gas mixture in subfigures 4.6a and b. For a fixed  $\chi_H$ , the  $\text{NH}_3$  increases linearly with the total  $\text{H}_2$  admixture to the gas flow, hence with  $f_{\text{H}_2}$  and  $c_{admix}$ . EY is plotted in subfigure 4.6c and describes the amount of energy required to produce a gram of  $\text{NH}_3$ .

A *blank experiment* is performed to assess any plasma-catalytic synergism. The ammonia fraction increases when increasing  $f_{\text{H}_2}$ ,  $c_{admix}$ , and the power for the blank experiment.  $\chi_H$  and EY decrease when increasing  $c_{admix}$  and the power, respectively. For instance,  $\chi_H$  drops from 0.35 to 0.30% when increasing  $c_{admix}$  from 1.0 to 1.25% and EY drops from 0.062 to 0.045 g- $\text{NH}_3$ /kWh when increasing the power from 4.0 to

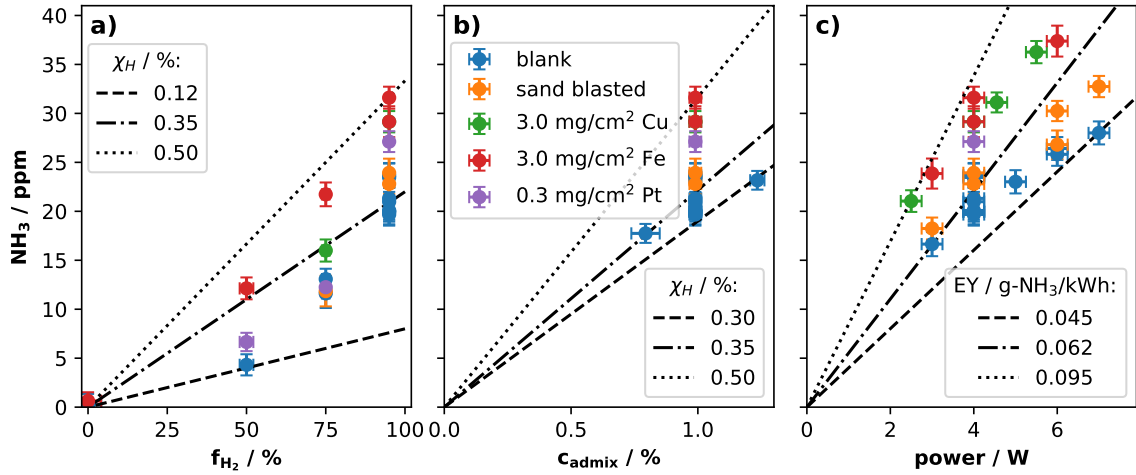


Figure 4.6: The molar fraction of NH<sub>3</sub> plotted as function of the H<sub>2</sub>-to-N<sub>2</sub> ratio (a), N<sub>2</sub>+H<sub>2</sub> admixture to the helium gas stream (b), and the plasma power (c).

7.0 W. The negative relation between  $\chi_H$  and  $c_{admix}$  is attributed to an increasing gas temperature with increasing  $c_{admix}$ . Unlike helium, N<sub>2</sub> and H<sub>2</sub> can be rotationally and vibrationally excited by electrons. These degrees of freedom quickly lose their energy to the translational mode, thereby increasing the gas temperature. The electron density increases when increasing the power. The lowering of EY with power is attributed to the increasing contribution of NH<sub>x</sub> dissociation by electron impact at higher powers.

Conversely,  $\chi_H$  increases with  $f_{H_2}$ , where it nearly triples from  $f_{H_2}=50\%$  towards 95%. Under ideal conditions, where no limiting reactions are present, the optimum gas ratio follows the stoichiometric ratio, i.e.  $f_{H_2}=75\%$ . This is typically observed in DBDs [135–137], which are characterised by high E/N values. Yet, our discharge has a low E/N, so N<sub>2</sub> dissociation might be the limiting reaction. Following the discussion of figure 4.3, the mean electron energy increases with  $f_{H_2}$ . This increase will stimulate the N<sub>2</sub> dissociation rate, thereby stimulating NH<sub>3</sub> synthesis. Hence, NH<sub>3</sub> production is promoted by hydrogen two-fold: 1) in promoting the hydrogenation of nitrogen radicals and 2) in increasing the nitrogen radical formation through increasing the presence of high-energy electrons. Hence, an optimum  $f_{H_2}$  near unity is obtained.

The surface composition has a considerable effect on NH<sub>3</sub> formation. On the one hand, introducing a sandblasted glass plate has a minimal impact on the conversion. Differences are only observed at powers higher than 4 W. On the other hand, introducing Pt, Fe, or Cu coated glass plates increases the NH<sub>3</sub> molar fraction considerably. The power variation shows similar results for the used materials. The differences are more pronounced when lowering  $f_{H_2}$  to 75% and 50%, where the Fe-coated glass plate clearly produces more NH<sub>3</sub> compared to the other used plates. Thus, a catalytic coating has a positive effect on NH<sub>3</sub> production.

The impact of desorption from the surface is studied by increasing the reactor temperature. The reactor temperature  $T_{reactor}$  is increased up to 160 °C for the blank and Fe-coating experiment for the  $f_{H_2}=50\%$  and 95% conditions of figure 4.6a. In figure 4.7, the difference of the molar fraction with respect to the average obtained at 20 °C is plotted with increasing reactor temperature.

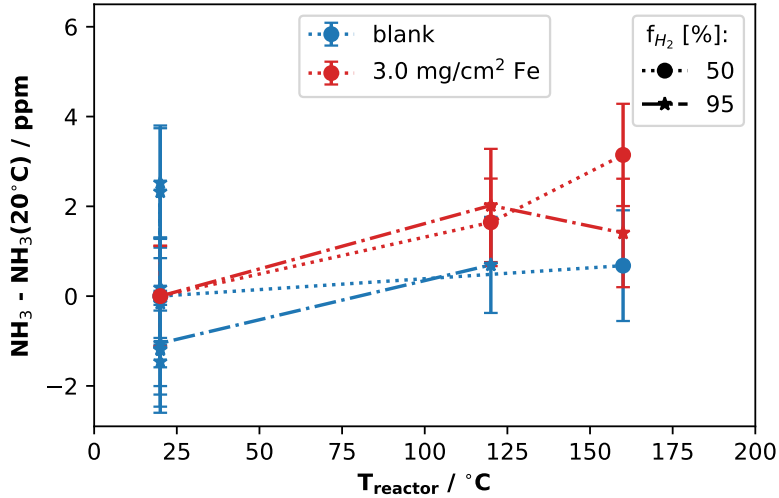


Figure 4.7: The impact of the reactor temperature on the ammonia concentration with the untreated glass plate (blue) and Fe-coated glass plate (orange) for two H<sub>2</sub>-to-N<sub>2</sub> gas ratios.

The NH<sub>3</sub> molar fraction increases only by 2 ppm when increasing  $T_{reactor}$  to 160 °C, which is on the same order as the uncertainty. This is in-line with literature, where a doubling of the NH<sub>3</sub> fraction is seen only for >300 °C [22]. Such temperatures are not achievable with the installed heating system. Therefore, these measurements are inconclusive in proving the activity the catalyst itself.

All in all, investigating the NH<sub>3</sub> fraction in the effluent shows that H<sub>2</sub>-rich environments are optimal for ammonia production. Its fraction can be further increased by increasing the total N<sub>2</sub>+H<sub>2</sub> admixture to the gas stream and discharge power. Yet, this is at the cost of the efficiency. Both the overall conversion and efficiency are improved when introducing a metallic coating to the walls. Therefore, the surface composition has a considerable impact on NH<sub>3</sub> formation. In the next section, the blank and Fe-coating results are reproduced by a kinetic model to study the underlying chemistry, since these data sets show a considerable difference in the NH<sub>3</sub> fraction and have the most data points.

### 4.3 Kinetic Model

Comparing the experiments with a kinetic model is vital for understanding the plasma chemistry. Many reactions are well studied and presented in literature. The reaction set used in this section is widely used in literature [29, 31, 32, 138]. In this section, we will discuss the considerations necessary to build a chemistry model that suits our discharge. Afterwards, this model is fitted to the experiments by adjusting the input parameters, e.g. E/N, which shows the rate limiting reactions.

The applied gas mixture is used as the initial gas composition. The N<sub>2</sub> and H<sub>2</sub> densities are set following their respective admixture at atmospheric pressure. The helium density is set constant to simplify the model, since it does not participate in

chemical reactions. Other kinetic models on similar helium plasmas show that less than 1% of the helium is excited [61, 129]. Therefore, the introduced error is minimal when fixing the He density.

The reaction set is given in appendix A. It is simplified by omitting ions as well as vibrational and electronic excitation of  $H_2$  and  $N_2$ . Only the impact of  $He^*$  is considered. The gas stream mostly exists of helium and the indirect  $N_2$  dissociation is significant at atmospheric pressures [139]. Penning ionisation of  $N_2$  is a prominent reaction in helium rich  $He/N_2$  plasmas [61, 132]. This is utilised to create an artificial reaction path way that dissociates nitrogen:  $He^* + N_2 \rightarrow He + 2N$ . Simultaneously, this reaction serves as a proxy for the various pathways of  $N_2$  dissociation via electronically excited states of  $N_2$ .

### Electron dynamics

The energetic electrons are the driving force behind the chemistry inside the discharge. The OES results of section 4.1 indicate that the electron density scales linearly with the discharge power. This agrees with previous assumptions, thus  $n_e \propto power$  is used with  $n_e(5W) = 10^{11} \text{cm}^{-3}$  [130].

The rate coefficient of electron impact reactions, e.g. dissociation, are calculated using a non-maxwellian EEDF that is calculated with LoKiB [57, 58]. It solves the Boltzmann equation using the reduced electric field, pressure, and gas mixture as input parameters. The electron impact cross sections for  $N_2$  and He are obtained from the LxCat database [54] and for  $H_2$  from [55]. Another database is used for  $H_2$ , since the IST-Lisbon version is under assessment at the time of running the model. The calculations are simplified by only considering the electronic grounds states of He,  $N_2$ , and  $H_2$ . The rotational and vibrational distributions are set in equilibrium with the translational mode, which is set to 300 K. Thus, super-elastic collisions are mostly omitted for the calculations.

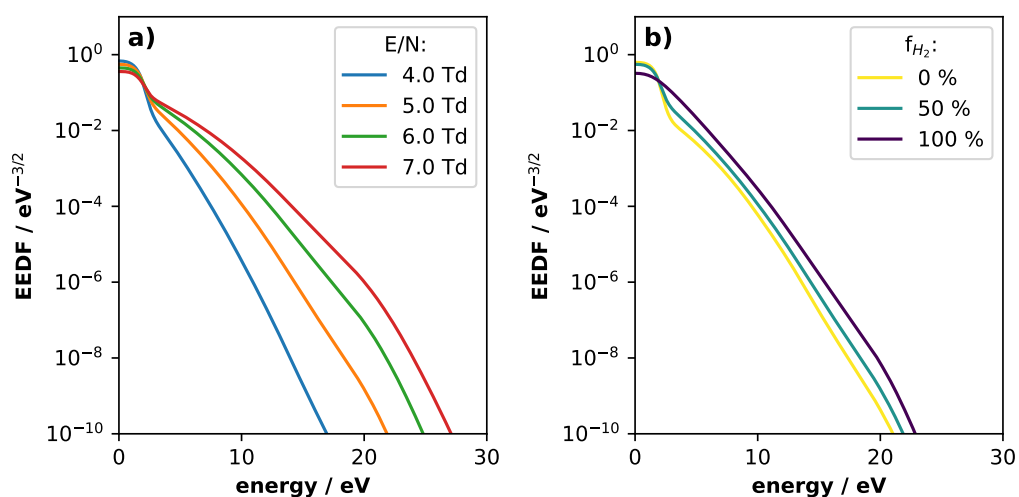


Figure 4.8: The electron energy distribution functions for different E/N values for  $f_{H_2}=50\%$  (a) and  $H_2$ -to- $N_2$  gas flow ratios for E/N=5.0 Td (b).

In figure 4.8, EEDFs are plotted for different E/N and  $f_{H_2}$  values for  $c_{admix}=1\%$

is used. The impact of  $E/N$  is illustrated in subfigure 4.8a, where the presented  $E/N$  values are commonly found in similar discharges [66, 68]. The presence of high-energy electrons ( $>15$  eV) is sensitive to  $E/N$ . The impact of the  $H_2$ -to- $N_2$  gas flow ratio is presented in subfigure 4.8b. The vibrational excitation cross section of  $N_2$  effectively limits the formation of high-energy electrons. This is seen from the bottleneck around 2 eV for  $f_{H_2} = 0$  and 50%. When interchanging  $N_2$  with  $H_2$ , the fraction of high-energy electrons increases, e.g. see  $f_{H_2} = 50$  to 100% where the EEDF increases above 2 eV. Therefore, the presence of high-energy electrons increases when increasing  $f_{H_2}$ .

The experimentally observed  $N_2(C)/N_2$  density ratio is compared to a radiative model in figure 4.9. The goal is to check if it is reasonable to assume that  $E/N$  does not vary with  $f_{H_2}$ . The experimental data for the blank glass plate and 4 W is used, which are labelled as *data*. The model density is calculated following equation 4.2, which is labelled as *model*. This relation describes the steady-state density ratio as function of the formation by electron impact (nominator) and relaxation (denominator). The *model* values are normalised to the experimental data at  $f_{H_2}=95\%$ , because the experiments lack an absolute calibration.

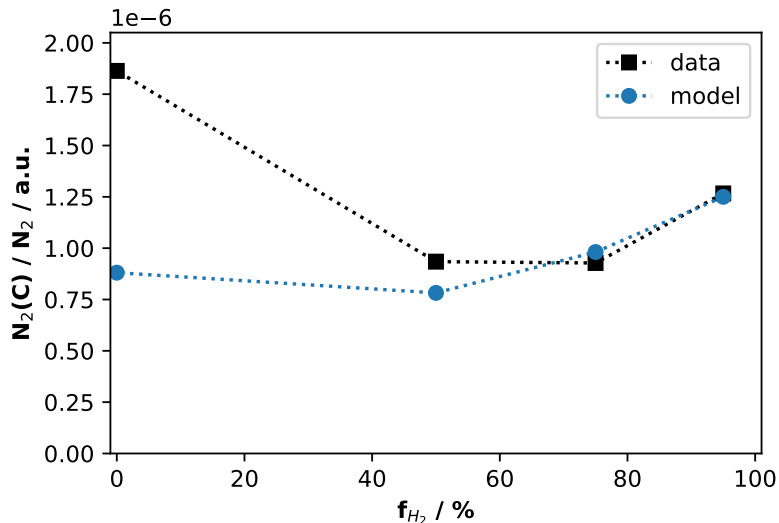


Figure 4.9: Comparing the measured  $N_2(C)/N_2$  density ratio to the radiative model of equation 4.2.

$$\frac{[N_2(C)]}{[N_2]} = \frac{k_{exc,e}n_e}{A + \sum_{M=N_2,H_2,He} k_{coll,M}[M]} \quad (4.2)$$

The electronic excitation by electron impact reaction rate  $k_{exc,e}$  is obtained from the convolution of the reaction's cross section and the EEDF for  $E/N=5.0$  Td, which is a typical value for the used discharge.  $N_2(C)$  deexcites by radiative and collisional relaxation. They are characterised by the Einstein coefficient  $A$  and rate coefficient  $k_{coll,M}$ , for collisional relaxation with species  $M=N_2$ ,  $H_2$ , and  $He$ , respectively. The radiative relaxation as well as the collisional relaxation for  $M=N_2$  and  $H_2$  relies on the vibrational distribution of  $N_2(C)$  [131, 140]. This distribution is obtained from

the experiments.  $k_{coll,Ar}$  is used instead of  $k_{coll,He}$  since they are both noble gases but  $k_{coll,He}$  could not be found in literature [141].

The radiative model correctly predicts the increase in the density ratio with increasing  $f_{H_2}$  in figure 4.9. The increased density of high-energy electrons can be explained due to changes in the EEDF as a function of the gas mixture. Thus, the assumption that  $E/N$  does not depend on  $f_{H_2}$  remains valid, and  $E/N$  may be decoupled from the gas mixture.

However, the model underestimates the density ratio for  $N_2$  rich gas mixtures, see  $f_{H_2} \leq 50\%$  in figure 4.9. This discrepancy is attributed to pooling reactions such as  $N_2(A) + N_2(A) \rightarrow N_2(C) + N_2$  [28]. An accurate description of all involved pooling reactions greatly increase the complexity of the kinetic model. This falls outside the scope of this thesis. Instead, a proxy through  $He^*$  is considered as mentioned before.

### Kinetic model

The kinetic model is fit to the experiments by varying  $E/N$  and the  $N_2$  dissociation gateway via excited helium species. The latter is done by varying the rate coefficient  $k_{R3}$  of reaction 3 in table A.1:  $e + He \rightarrow e + He^*$ . The results of this analysis are presented in figure 4.10. Different versions of the model are compared to the experiments to highlight the necessity of modifying either  $E/N$  or  $k_{R3}$ . First, the model is fit to the absolute value of *reference condition* ( $f_{H_2}, c_{admix}, power$ ) = (95%, 1%, 4 W). Second, the power variation is fit. Third, the impact of the iron coating is fit. Difference in the model between the blank and Fe-coating experiment follow from different sticking coefficients and energy barriers. Hong et al. proposed different values for a metal (which are typically derived in thermal catalysis) and a dielectric material  $Al_2O_3$ , or glass in our case [32].

The model is fit to the *reference condition* by setting  $E/N$  to 6.4 Td, see column labelled as *1. Original*. The  $E/N$  agrees with the expected order of magnitude presented earlier. The trends of the parameter scan are not as easily reproduced by the model. Despite that the model correctly predicts that  $H_2$  rich conditions are favourable for  $NH_3$  production, the relation between  $f_{H_2}$  and  $NH_3$  is too weak. This could arise from secondary effects of the gas mixture on the plasma. For instance, the OES results show that  $[He^*]$  increases with  $f_{H_2}$ . Following the reaction set of table A.1, the dissociation rate of  $N_2$  increases with increasing  $[He^*]$ . However, it is difficult to determine the exact relation between  $[He^*]$  and  $f_{H_2}$ . Therefore, such effects are not considered in the kinetic model to prevent overdetermination of the model.

In contrast to the experiments, the model shows that a negative relation above 4 W between the  $NH_3$  fraction and the power. Electrons contribute to both the forward reaction, through  $N_2$  and  $H_2$  dissociation, as well as to the backward reaction, through dissociation of  $NH$ ,  $NH_2$ , and  $NH_3$ . The negative relation between  $NH_3$  and the power shows that the cracking reactions overtake the positive impact that  $N_2$  and  $H_2$  dissociation have. This indicates that electron-impact reactions are overestimated. Therefore, this is corrected in the next attempt.

The power scan scan of the model is improved by increasing  $k_{R3}$  by a factor of 15 and lowering  $E/N$  to 5.6 Td, see middle column labelled *2. Enhanced  $He^*$* . This yields a good agreement between the model and experiments. Also, the  $NH_3$  vs  $f_{H_2}$  trend agrees better with experiments. However, this version of the model predicts no difference

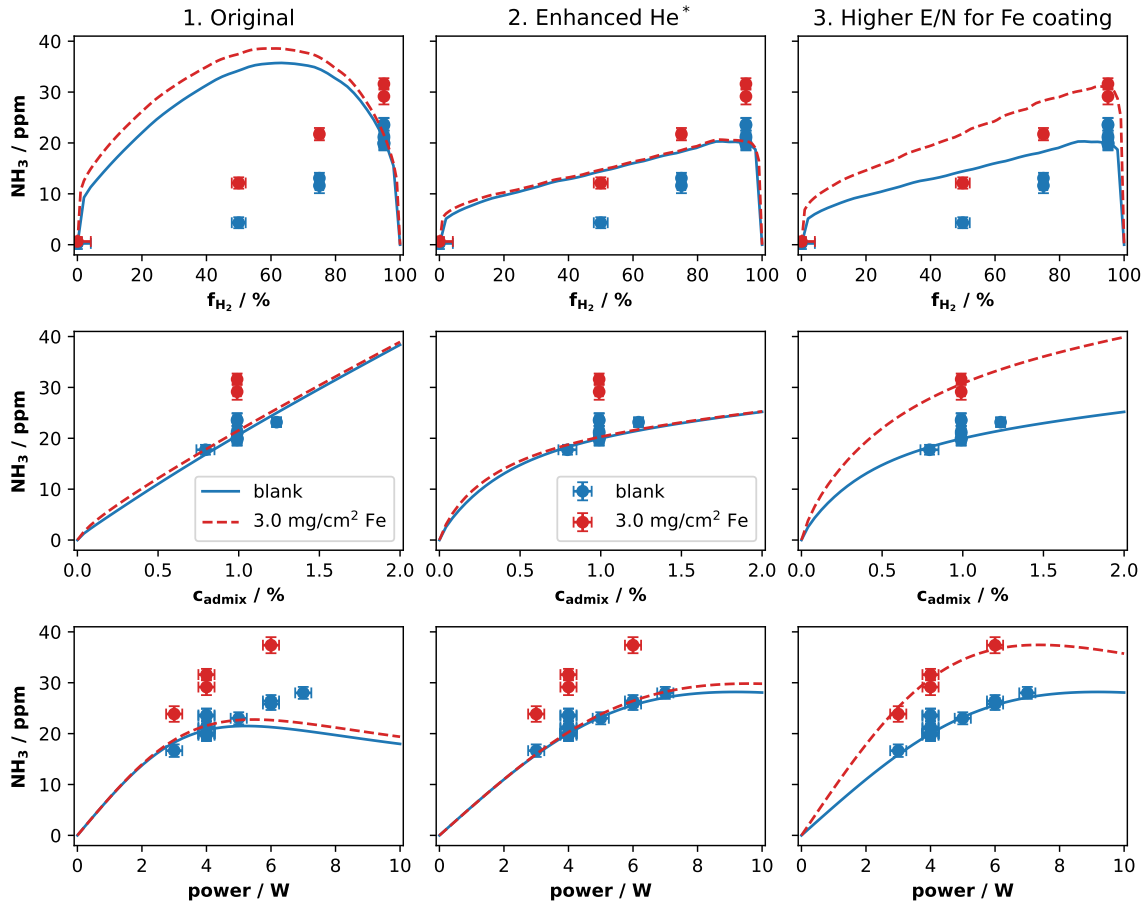


Figure 4.10: A comparison of the model with the measured concentrations for the blank (blue) and Fe-coated (red) measurements, for the different model iterations.

between the blank and Fe-coating. Similar to the electron-impact reactions, not all surface reactions contribute positively towards the formation of  $\text{NH}_3$ . The higher H-abstraction  $\text{H} + \text{H}_s \longrightarrow \text{H}_2 + \text{S}_f$  (reaction S6 in table A.2) sticking coefficient for metals contributes to the so-called back-reactions. This diminishes the positive effect of the coating on the ammonia production, through LH-reactions that form  $\text{NH}_3$ . Therefore, another explanation is required to explain the experimentally observed differences.

Finally, the measured increase in  $\text{NH}_3$  production is realised by increasing  $E/N$  to 5.75 Td for the Fe-coating experiment. This is given in the column labelled as 3. *Higher  $E/N$  for Fe-coating*. The reduced electric field is increased by 0.15 Td that still fits to the experimental results presented in section 4.1. The marginal increase in  $E/N$  is hard to observe in the emission spectra, e.g. see [142] where a change in the electron temperature of several eV is needed to observe differences in the vibrational distribution of  $\text{N}_2(\text{C})$ .

Employing the kinetic model to understand the underlying processing in the formation of  $\text{NH}_3$  is successful. The model reproduces the experiments rather well. Minor differences are attributed to the limitations of this model. Thus, the reaction set responsible for  $\text{NH}_3$  production can now be examined to explain which reactions are responsible for the  $\text{NH}_3$  formation.

### Ammonia formation

In figure 4.11, the molar fractions and the surface coverages are presented for the blank (solid lines) and Fe-coated (dashed lines) experiments of the final model iteration. The molar fractions are plotted in ppm and plotted in the top row. The gas phase fractions of He, H<sub>2</sub>, and N<sub>2</sub> are omitted since they are a magnitude of order greater than of the species that are plotted. In the bottom row, the surface coverages are presented with the same colouring for N, H, NH, and NH<sub>2</sub>.

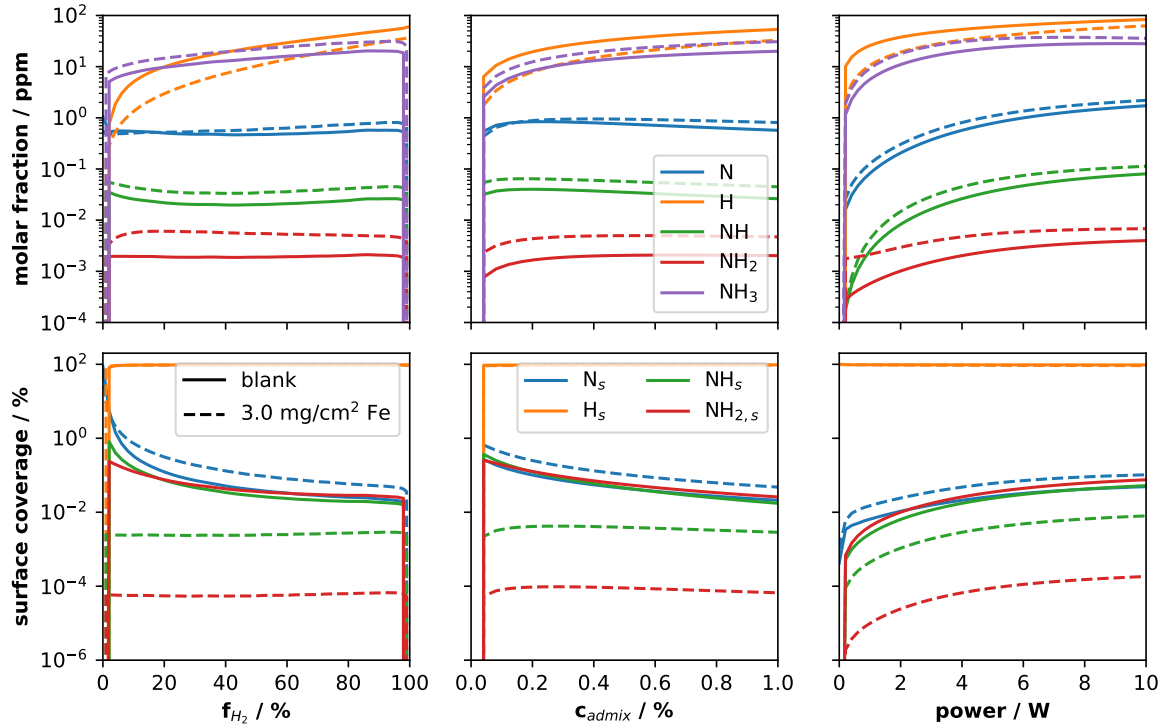


Figure 4.11: The molar fractions (top row) and surface coverages (second row) for the third model iteration of figure 4.10 for the blank (solid lines) and Fe-coated (dashed lines) experiment.

The surface chemistry differs between the blank and the Fe-coating experiment due to the different sticking coefficient and reaction energy barriers. However, following the literature values, the Fe-coating has a negative impact on the NH<sub>3</sub> production. The higher coefficient for H-abstraction on the surface dominates over the stepwise hydrogenation of nitrogen. Thereby, the loss rate for hydrogen radicals increases. This is seen in the lower H(g) density in the first row. The densities of N, NH, NH<sub>2</sub> and NH<sub>3</sub> only increase after increasing E/N by 0.15 Td. Consequently, the surface coverages of H decreases and N increases from the blank to the Fe-coating experiment. Nonetheless, hydrogen still dominates on the surface, since the atomic hydrogen density is significantly higher than of atomic nitrogen. Also, H reaches the surface faster than N following the diffusion model, see equation 2.6.

Metals such as iron are typically used in thermal catalysis due to the low energy barriers for LH-reactions. These reactions also affect the surface composition in our case. The coverage of the radicals NH and NH<sub>2</sub> are lower on the iron coating than

with the blank experiment, since these adsorbants quickly reacts to  $\text{NH}_3$ . This has a positive effect on the  $\text{NH}_3$  production.

The model predicts that most of the ammonia is made in the gas phase. For the blank experiment, only 8% is produced on the surface and that is solely associated to ER-reactions. This value increases to 14% when introducing the Fe-coating. There, 10% is associated to LH-reactions and 4% to ER-reactions. This in contrast to other studies [32, 138]. There DBDs were used that have a higher surface area to plasma volume ratio that enlarges the impact of surface reactions to the overall chemistry.

Finally, the molar fractions and surface coverages highlight that the iron coating does not have a typical catalytic effect on  $\text{NH}_3$  production. The higher H-abstraction rate from the surface cancels any positive effect the improved LH-reaction rates may have. Rather, the increased E/N by the coating increasing the nitrogen dissociation rate, thereby the stepwise hydrogenation towards  $\text{NH}_3$ .

## 4.4 Discussion

The ammonia synthesis in an atmospheric RF discharge using  $\text{He}/\text{N}_2/\text{H}_2$  gas mixtures is studied in this chapter. The production is experimentally characterised by measuring the trends in the  $\text{NH}_3$  molar fraction in the effluent. A hydrogen rich gas mixture is optimal for the production of ammonia. Sandblasting and introducing a metallic coating to the glass plates increases the production further.

In thermal catalysis, the N-binding energy is an important parameter in determining the optimal material for  $\text{NH}_3$  production. In this study, three materials are used that effectively scan the N-binding energy from -1 to 2 eV. Yet, the results are very similar. Note that Pt under-performs compared to Cu and Fe, but this is associated to the much lower specific surface area of the Pt coating compared to that of copper and iron. Thus, the N-binding energy is not important for plasma catalysis, as is suggested in literature [34, 35].

The observed trends are reproduced with a kinetic model to study the underlying chemistry. The model shows that the  $\text{N}_2$  dissociation is the limiting factor for  $\text{NH}_3$  production. Hence, the  $\text{NH}_3$  fraction in the effluent is very sensitive to the mean electron energy. The positive impact of the Fe-coating on the  $\text{NH}_3$  is explained through an increase in E/N that stimulates  $\text{N}_2$  dissociation. Therefore, rather than improving the chemistry, the supposedly catalytic coating improved the plasma performance for the ammonia production.

The proposed higher E/N for Fe-coated glass compared to the untreated glass plate is explained by considering the secondary electron emission coefficient  $\gamma_{se}$ . Following the discussion on secondary electron emission in subsection 2.1.1,  $\gamma_{se}$  is higher for the untreated glass plate (i.e. a dielectric surface) than with a Fe-coating (i.e. metallic surface). A higher ionisation rate in the gas gap is required to sustain the discharge at similar conditions (e.g. driving voltage, plasma power, and  $\text{N}_2$  emission). This can be realised by increasing E/N. Hence, a higher E/N is expected with the Fe-coating than for the blank experiment.

Furthermore, the secondary electrons contribute mostly to the high-energy tail of the EEDF [48]. This could explain the slightly more intense FNS emission of figure 4.3b for untreated glass plate (blank) compare to the Fe-coating. All in all, the difference

in the SEE is a likely candidate to explain the higher E/N values for the Fe-coating with respect to the blank experiment.

More recently the term Plasma-Catalysis Promoter (PCP) was coined by Ruiz-Martín et al. [143]. They highlighted that many papers report on the catalyst impact the plasma, rather than the catalyst opening up more efficient reaction path ways. The results presented in this chapter follow this narrative. Hence, an in-plasma catalyst should perhaps be chosen for their impact on the plasma itself.



# Chapter 5

## Nitrogen Fixation in a Plasma-Exposed Surface Interface

The combination of plasmas with catalysis is proposed to create a breakthrough in the conversion and selectivity of gas conversion [145]. Electronic and vibrational excitation by the plasma are expected to help molecules to overcome reaction barriers that are typically found in thermal catalysis. A plasma catalytic reactor is a complex system with various degrees of freedom. In this chapter, the plasma-induced surface chemistry is studied, which is one of the important aspects of plasma catalysis.

The surface chemistry is understood by examining the steady-state surface compositions in a  $\text{N}_2/\text{O}_2$  and  $\text{N}_2/\text{H}_2$  gas mixture. First, this requires to understand how the surface composition is altered by the plasma. Second, a parameter study is performed to investigate the formation of the observed surface groups. The surface must be carefully prepared before the measurements can be performed. Therefore, in each section, the pretreatment is first discussed whereafter the surface composition is examined and finally a parameter study is performed.

### 5.1 $\text{NO}_x$ Formation by $\text{N}_2+\text{O}_2$ Plasma

The nitrogen oxidation via surface processes is studied by investigating the presence of nitrogen oxides on an iron foil. Iron is a commonly used material for nitrogen fixation processes. Before studying the  $\text{NO}_x$  formation, the substrate is pretreated to reduce the impact of impurities on the IRRAS spectra and surface chemistry following subsection 3.2.2.

#### 5.1.1 Pretreatment

The iron foil is in direct contact with a  $\text{N}_2/\text{O}_2$  low-pressure plasma. Iron oxides are readily formed once such a plasma is ignited. Also, the presence of impurities must be avoided, as mentioned in section 3.2.2. The substrate is first treated with a 200+20

---

This chapter is partially based on the work previously published as Vervloedt and von Keudell Plasma Chemistry and Plasma Processing 45 (2025) 1551–1565 [144]

sccm He+O<sub>2</sub> plasma. Secondly, a 20 sccm O<sub>2</sub> plasma is ignited to finalise the oxidation, so this does not appear in the later IRRAS spectra of N<sub>2</sub>+O<sub>2</sub> plasmas.

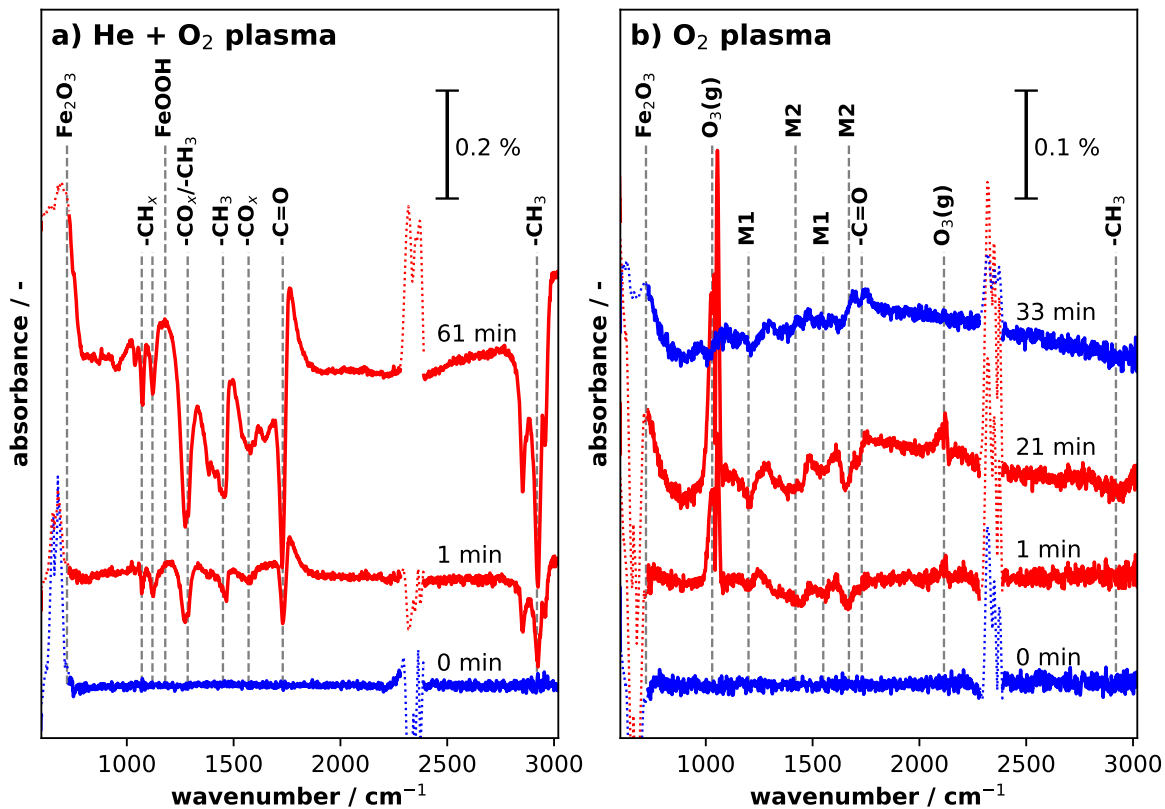


Figure 5.1: IRRAS spectra obtained during the He+O<sub>2</sub> plasma (a) and the subsequent O<sub>2</sub> plasma (b).

In figure 5.1, IRRAS spectra obtained during a typical pretreatment are presented. The reflection spectra are plotted in a stacked plot so the changes in time are visualised. The red and blue colouring indicate that the plasma is either on or off, respectively. The time compared to its reference spectrum is indicated at each spectrum. This format will be repeated for the other plots in this chapter. The contribution of CO<sub>2</sub>(g) could not fully be removed from the spectra, despite isolating the open-air path and correcting with a reference spectrum. These regions are smoothed using a moving average over 10 cm<sup>-1</sup> and plotted using a dotted line.

The impact of the He/O<sub>2</sub> plasma is presented in figure 5.1a. Negative absorption bands are observed after operating the plasma for 1 minute. They indicate the removal of carbonyl and hydrocarbon species. The bands at 2850, 2920, and 2960 cm<sup>-1</sup> are identified as the CH<sub>3</sub> stretch modes. The band at 1730 cm<sup>-1</sup> is associated with the C=O stretch mode [146–148]. The peaks in the fingerprint region, 1000 to 1700 cm<sup>-1</sup>, are more difficult to identify. The bending modes of various hydrocarbon and carbonyl species are expected to appear here [149]. Thus, all bands observed in this spectral region are attributed to these carbon impurities.

The carbonyl and hydrocarbon impurities continue to be removed in time. The spectrum *61 min* shows positive absorption bands at 720, 1180, and 1760 cm<sup>-1</sup> as

well. They are attributed to the formation of  $\text{Fe}_2\text{O}_3$ , iron oxyhydroxide ( $\text{FeOOH}$ ), and restructuring of carbonyl groups [149, 150]. Other iron oxides cannot be observed due to the lower limit of the measured spectra, as these typically absorb light from 300 to  $600\text{ cm}^{-1}$  [151, 152].  $\text{FeOOH}$  is likely the result of hydrogen radicals re-adsorbing on the surface. The removal and subsequent oxidation of the hydrocarbons is a likely source for the hydrogen. The growth of  $\text{FeOOH}$  is more pronounced in measurements where the reactor is vented in the days before (not shown). The humidity from air is able to adsorb at the surfaces inside the reactor and provide the plasma with a constant supply of hydrogen radicals that form  $\text{FeOOH}$  in a  $\text{He}/\text{O}_2$  plasma, similar to [150, 153].

The impact of a 20 sccm  $\text{O}_2$  plasma is presented in figure 5.1b. The scale is magnified to better present the smaller changes in the IRRAS spectra. This plasma is ignited in quick succession after the  $\text{He}+\text{O}_2$  to prevent re-adsorption of carbon impurities. A new reference spectrum is obtained, see spectrum *0 min*. The plasma also produces  $\text{O}_3$ , which is very typical for a  $\text{O}_2$  plasma. This plasma continues to remove impurities from the surface. Bands other than  $\text{C}=\text{O}$  are labelled as M1 and M2. Their origin is not known. The bands of M2 appear in later spectra as well. The impurities tend to re-adsorb once the plasma is turned off. Therefore, minor changes in the fingerprint region are expected to persist in the later  $\text{N}_2+\text{O}_2$  plasma spectra.

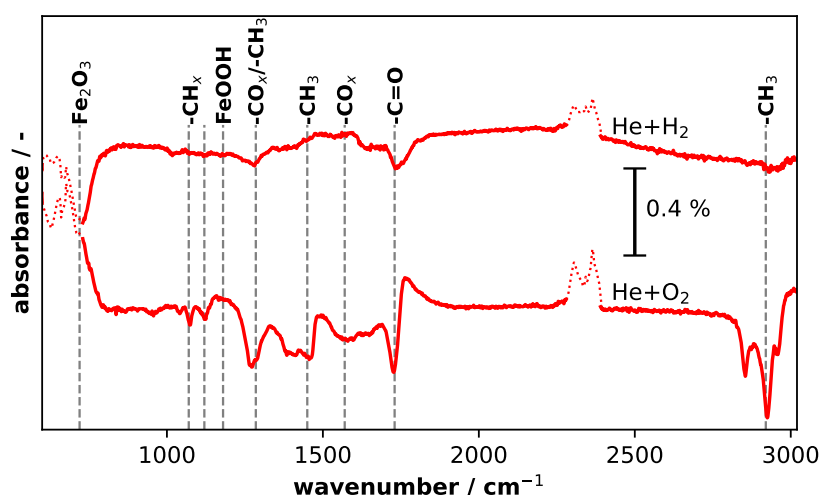


Figure 5.2: IRRAS spectra obtained after 61 min of  $\text{He}+\text{O}_2$  and subsequently igniting a  $\text{He}+\text{H}_2$  plasma.

The formation of  $\text{Fe}_2\text{O}_3$  and restructuring of  $\text{C}=\text{O}$  bonds are verified by igniting a 200 sccm  $\text{He}$  with 20 sccm  $\text{H}_2$  plasma directly after the  $\text{He}+\text{O}_2$  plasma. The IRRAS spectra obtained after these spectra are plotted in figure 5.2. The  $\text{He}+\text{H}_2$  plasma spectrum shows the removal of the iron(III)oxide and  $\text{C}=\text{O}$  band around  $720$  and  $1740\text{ cm}^{-1}$ , respectively. Thus, these observations support the previous assignment of the iron oxide peak and restructuring of carbonyl groups.

In the end, the pretreatment minimises the surface coverage of carbon impurities as well as oxidising the top layer of the substrate. Therefore, the formation of  $\text{NO}_x$  will be considered on iron oxides, instead of a pure metallic iron foil.

### 5.1.2 Identification of Reflection Spectra in 1:1 N<sub>2</sub>:O<sub>2</sub>

A 10+10 sccm N<sub>2</sub>+O<sub>2</sub> plasma is ignited after the He+O<sub>2</sub> and pure O<sub>2</sub> plasmas. The surface temperature is controlled at 40 °C and the plasma power at  $1.01 \pm 0.05$  W. The reflectance spectra are plotted in time in figure 5.3 from 650 to 3500 cm<sup>-1</sup>. Their baseline is corrected with a linear fit. The timestamps are plotted above the corresponding spectra. The first spectrum (0.0 min) is obtained before plasma ignition. The plasma is ignited from 1.5 to 27.0 minutes, see red spectra. The reactor is evacuated at 42.5 min.

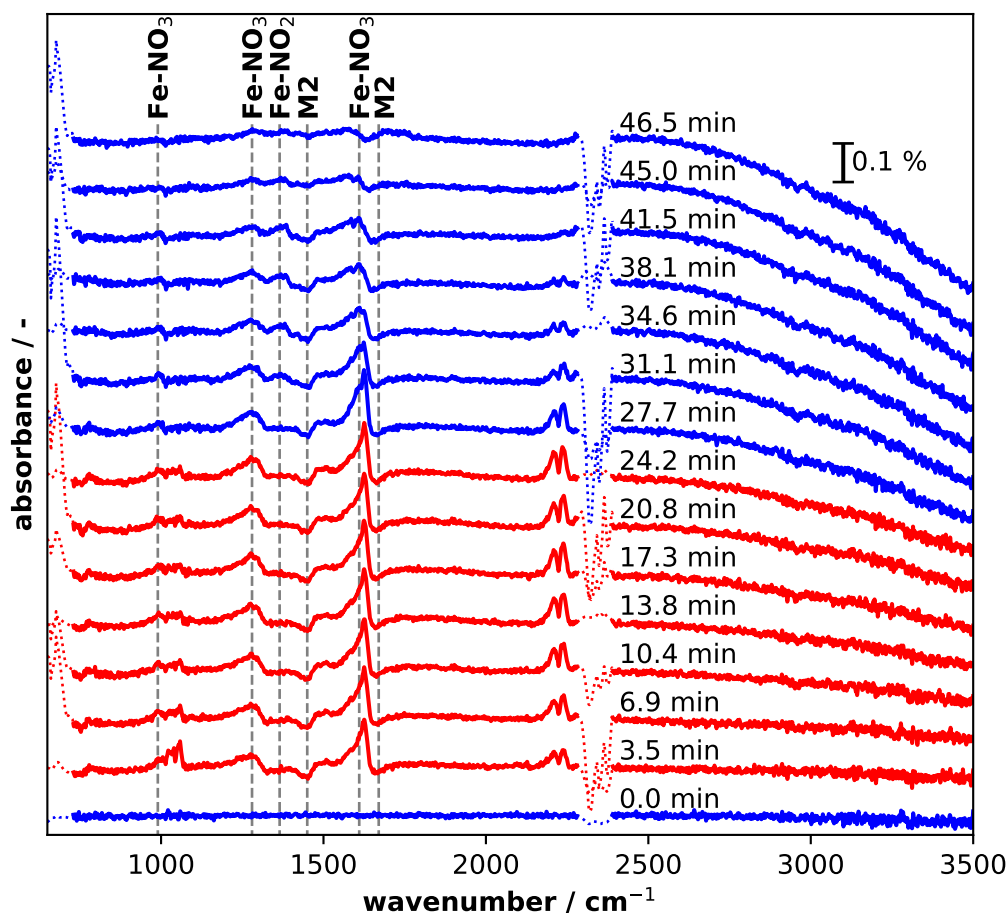


Figure 5.3: Reflectance spectra obtained during a N<sub>2</sub>+O<sub>2</sub> plasma with 10+10 sccm N<sub>2</sub>+O<sub>2</sub> gas flow with the identification attributed to surface-bound species.

#### Line identification

The spectra contain absorption features of both gaseous and surface-bound species between 900 and 2280 cm<sup>-1</sup>. The formation of O<sub>3</sub>(g) and N<sub>2</sub>O(g) are readily apparent from the spectra, where their ro-vibrational bands occur around 1040 and 2220 cm<sup>-1</sup>, respectively. Two negative absorbance bands around 1430 and 1680 cm<sup>-1</sup> are similar to the M2 bands seen during a pure O<sub>2</sub> plasma in figure 5.1b. They are associated to

the reoccurring removal of impurities from the substrate that readsorb once the plasma is switched off.

Four distinct positive absorbance bands around 990, 1280, 1360, and 1620 cm<sup>-1</sup> are associated to nitrogen oxides. The band around 1620 cm<sup>-1</sup> is the most often observed in literature and often associated to nitrates (NO<sub>3</sub><sup>-</sup>) [40, 41, 43, 154]. It is typically observed alongside bands between 1200 and 1300 cm<sup>-1</sup> [43, 154–156]. The band at 990 cm<sup>-1</sup> is also associated to nitrates [41, 157]. It is, however, rarely presented in literature as it falls outside the spectral range of many studies. Finally, the band at 1360 cm<sup>-1</sup> is associated to nitrites (NO<sub>2</sub><sup>-</sup>) [43, 156].

However, literature is not consistent in identifying the 1620 cm<sup>-1</sup>-band to nitrates. Some studies attributed it to nitrites instead [156, 158–160]. It is difficult to spectrally distinguish between NO<sub>2</sub> and NO<sub>3</sub>, since they have similar stretch modes [39, 155, 161]. Nitrites are typically formed under low NO-exposures whereas nitrates grow when increasing the NO exposure [43]. When comparing the gas phase densities (which are  $\sim 10^{13}$  cm<sup>-3</sup> as will be presented later) to typical surface science experiment exposures, the surface is already heavily dosed after acquiring a single spectrum. The dosing already exceeds 1000 L, i.e. sufficient to fill 1000 monolayers. Thus, the presence of nitrates is more likely than of nitrites.

Furthermore, other nitrogen oxide surface groups are not observed. Adsorbed NO, N<sub>2</sub>O, and N<sub>2</sub>O<sub>4</sub> species appear between 1700 and 2300 cm<sup>-1</sup> [162–166]. No such bands are observed in the IRRAS spectra, despite that they are observed in the presence of the NO<sub>x</sub>(g) species under thermal conditions, e.g. see [165]. This indicates that these species are quickly oxidised on the surface once they adsorb. Evidence of the strong oxidising nature of the plasma is seen in the production of Fe<sub>2</sub>O<sub>3</sub> in 10:1 He:O<sub>2</sub> plasma in figure 5.1a and 5.2.

### Deconvolution of IRRAS spectra

The spectral contributions are characterised to estimate the gas phase densities and the intensities of surface-bound associated bands. The intensity is proportional to the surface coverage, but absolute coverage values cannot be obtained as mentioned in section 2.2.3. In figure 5.4, the spectra obtained at 6.9, 24.2, and 34.6 min are deconvoluted in the gas and surface phase components. In subfigures a-c, the spectra are plotted from 900 to 2280 cm<sup>-1</sup> and contain most of the contributions. The feature around 1620 cm<sup>-1</sup> consists of multiple contributions. Its deconvolution is plotted in subfigures d-f, where the spectra are zoomed-in to the range from 1500 to 1775 cm<sup>-1</sup>.

Two stretch modes of N<sub>2</sub>O(g) are observed around 1280 and 2220 cm<sup>-1</sup>. They correspond to the N-O and N-N stretch, respectively. The N-N stretch is spectrally isolated from other contributions and is more IR-active than N-O stretch. It is, therefore, suitable to quantify the N<sub>2</sub>O density using a synthetic spectrum. The outcome of the fitting is used to estimate the absorption feature expected from the N-O stretch. The total N<sub>2</sub>O(g) spectrum is plotted in subfigures 5.4a-d. The removal of the N-N stretch mode gives a near linear baseline. This indicates that no other features are present at this spectral position. The removal of the N-O stretch bands around 1280 cm<sup>-1</sup> indicate that at least two other absorption bands are present from 1200 to 1310 cm<sup>-1</sup>.

The absorption feature of NO(g) typically hides in the noise of the IRRAS spectrum. Nonetheless, a synthetic spectrum is fit to the measured spectra. Other nitrogen oxides

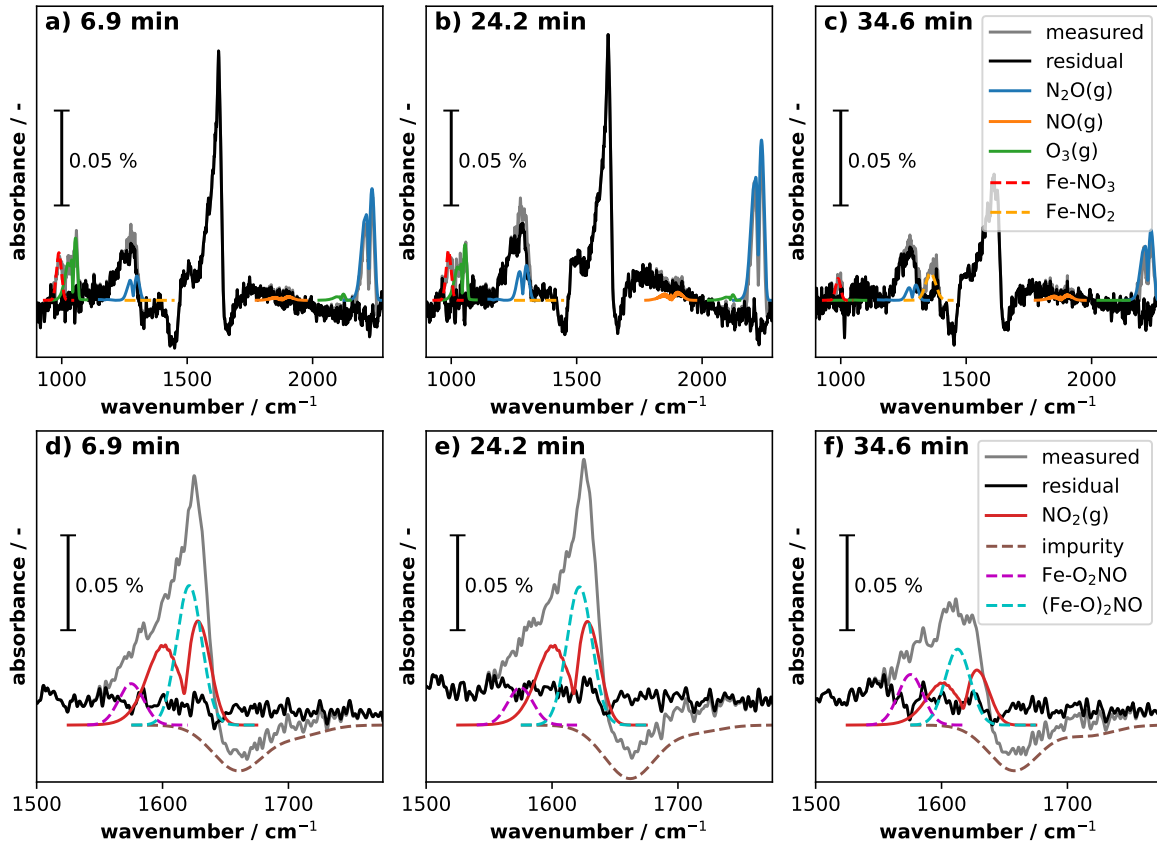


Figure 5.4: Deconvolution of the IRRAS spectra at 6.9 min (a, d), 24.2 min (b, e), and 34.6 min (c, f) in two parts, where gaseous contributions are plotted with solid lines and surface contributions with dashed lines.

are observed, thus nitric oxide is likely present as well. Its presence is more clear near the end of the plasma operation phase (see spectrum at 24.2 min in figure 5.4b) and for higher  $N_2$ -to- $O_2$  gas flow ratios, as we will see in section 5.1.4.

Ozone has one IR active mode that is visible around  $1040\text{ cm}^{-1}$  and the overtone ( $\Delta v=2$ ) around  $2100\text{ cm}^{-1}$ . The  $1040\text{ cm}^{-1}$  band is more IR-active than the overtone, but it overlaps with a band associated with nitrates around  $990\text{ cm}^{-1}$ . This feature is approximated as a Gaussian lineshape with a FWHM of  $23.5\text{ cm}^{-1}$  and labelled as  $Fe-NO_3$ . These features are simultaneously fit. The resulting  $O_3(g)$  density is used to estimate the absorption of the overtone, similar to  $N_2O(g)$ .

After switching off the plasma, another surface band that is associated to nitrites  $Fe-NO_2$  is observed around  $1360\text{ cm}^{-1}$  [43]. This band is approximated by a Gaussian with a FWHM of  $47.0\text{ cm}^{-1}$ , since it appears broader than the aforementioned  $Fe-NO_3$  band. However, the baseline estimation is ambiguous due to the surrounding changes in the absorbance. Thus, the uncertainty of its intensity is higher than of the other surface-bands.

In figures 5.4d-f, the nitrate band around  $1620\text{ cm}^{-1}$  is characterised together with the expected  $NO_2(g)$  absorption feature. The impurity removal, on the right hand side, is approximated with two Gaussian peaks with FWHM of  $47.0\text{ cm}^{-1}$  centred at  $1670$  and  $1720\text{ cm}^{-1}$ . Their contribution is estimated by fitting these Gaussians to the

spectrum from 1650 to 1850  $\text{cm}^{-1}$ , see *impurity* spectrum. The outcome is removed before the contributions of  $\text{NO}_2(\text{g})$  and nitrate are fit. The nitrate contribution is characterised with two Gaussian peaks with FWHM of 23.5  $\text{cm}^{-1}$  centred at 1580 and 1620  $\text{cm}^{-1}$ . They are attributed to chelating bidentate nitrate  $\text{Fe-O}_2\text{NO}$  and bridging bidentate nitrate  $(\text{Fe-O})_2\text{NO}$  [41, 43, 154]. The corresponding binding configurations are illustrated in figure 5.5. Bridged bidentate nitrates binds to neighbouring Fe-sites. Its binding energy is higher than that of chelating bidentate nitrates, which is only bound to a single site.

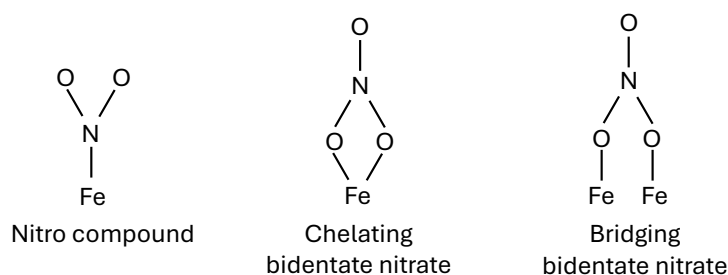


Figure 5.5: The binding configuration of the observed nitrite and nitrates.

### Temporal trends of gas and surface-bound species

In figure 5.6, the gas phase densities and the intensities of the nitrite and nitrate intensities are plotted in time. These values are obtained from the previously mentioned deconvolution of the spectra. The timestamp at which the plasma is switched on and off and when the reactor is evacuated is indicated with vertical black dashed lines. The gas phase densities are obtained similar to IR absorption spectroscopy. This is a line-of-sight averaged diagnostic, thus spatially averaged densities are given. A density gradient is expected along the line-of-sight of the IR beam. The plasma products are synthesised in the center of the reactor and diffuse outwards. However, a proper description of the spatial profile falls outside the scope of this thesis.

The gas phase densities all increase during the plasma operation and all decrease once the plasma is switched off. The temporal trend of  $\text{N}_2\text{O}(\text{g})$  follows the behaviour expected from the continuity equation with a constant plasma production term and an outflow term. During plasma operation, the reactor gradually fills with  $\text{N}_2\text{O}(\text{g})$ . This yields the limited exponential growth. Once the plasma is switched off, its density exponentially decreases, since the production term is set to zero. Finally, when evacuating the reactor,  $\text{N}_2\text{O}(\text{g})$  is completely removed from the reactor. Similar trends are also observed for the other plasma products, but some notable differences are observed.

The  $\text{O}_3(\text{g})$  density shows abrupt changes in time. Its density spikes when switching on the plasma, whereafter it relaxes to a lower value at  $2.0 \times 10^{13} \text{cm}^{-3}$ . Ozone is a reactive molecule that readily reacts with  $\text{NO}(\text{g})$  to form  $\text{NO}_2(\text{g})$  as  $\text{O}_3 + \text{NO} \longrightarrow \text{O}_2 + \text{NO}_2$ , therefore the  $\text{O}_3(\text{g})$  density decreases with increasing  $\text{NO}(\text{g})$  density in time [90]. When switching-off the plasma, the  $\text{O}_3(\text{g})$  and  $\text{NO}(\text{g})$  densities drop and that of  $\text{NO}_2(\text{g})$  undergoes a instantaneous increase. The aforementioned  $\text{NO}(\text{g})$ -oxidation is countered by the reactions involving atomic oxygen during plasma operation. Ozone is produced

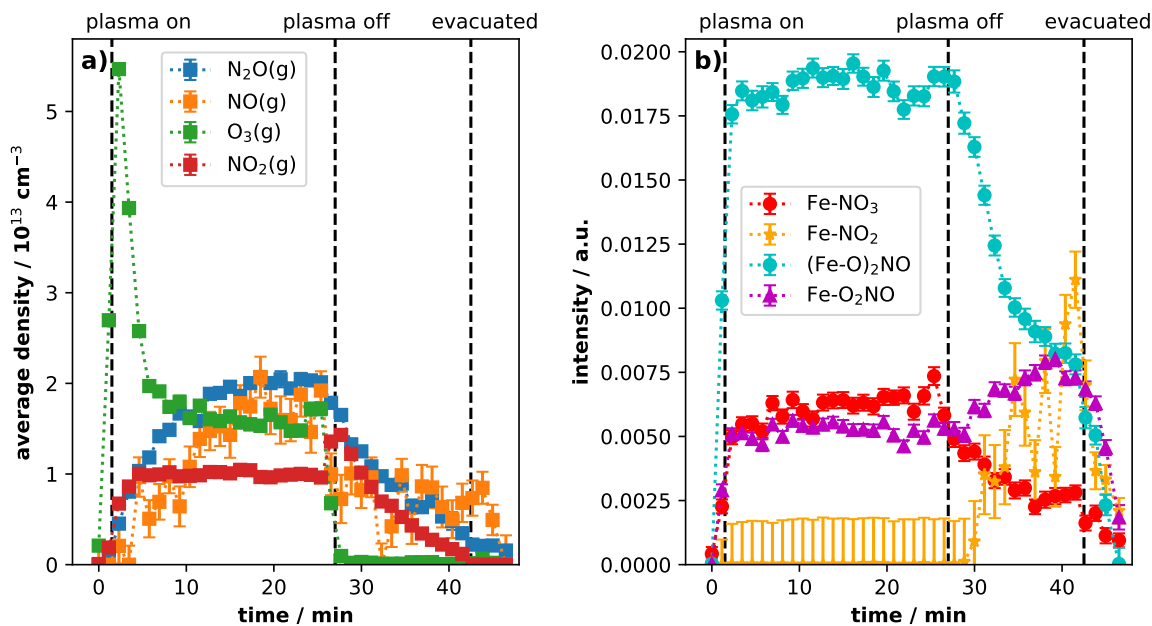


Figure 5.6: The line-of-sight averaged densities of the gaseous species (a) and the nitrites and nitrates intensities (b) in time obtained from the spectra shown in figures 5.3 and 5.4.

as  $\text{O}_2 + \text{O} + \text{M} \longrightarrow \text{O}_3 + \text{M}$  and  $\text{NO}_2$  is reduced as  $\text{NO}_2 + \text{O} \longrightarrow \text{NO} + \text{O}_2$ , where M is an arbitrary third collision partner. Atomic oxygen quickly recombines once the plasma is off, since the recombination time constant is much shorter than the time resolution ( $\sim 1.0$  min). Thus, the  $\text{NO}(\text{g})$ -oxidation prevails and the  $\text{NO}_2(\text{g})$  density increases at the cost of the  $\text{NO}(\text{g})$  and  $\text{O}_3(\text{g})$  densities.

Furthermore, the abrupt change in the  $\text{O}_3(\text{g})$  density compared to  $\text{N}_2\text{O}(\text{g})$  indicates that most  $\text{O}_3(\text{g})$  is localised in (or near) the plasma source. Otherwise, this density would change on a longer time scale. This is also expected for atomic oxygen, which is confined near the plasma by recombination reactions. In an atmospheric  $\text{O}_2/\text{He}$  plasma, atomic oxygen is confined to 1 mm around the plasma source [86]. This loss rate of atomic oxygen is associated to reactions with molecular oxygen. When extrapolating to the conditions in this chapter, by considering a change in the diffusion constant and the applied  $\text{O}_2$  partial pressure, all atomic oxygen species are lost at a distance of 1 cm from the plasma. This is much shorter than the total optical path length of 42.6 cm. Therefore, the  $\text{O}_3(\text{g})$  density distribution coincides with that of atomic oxygen.

In figure 5.6b, the intensities of the nitrites and nitrates contributions are plotted. Bridged bidentate nitrate  $(\text{Fe-O})_2\text{NO}$  has the highest intensity. It is formed after igniting the plasma, where it immediately reaches steady-state value. Its intensity decreases after switching off the plasma, which indicates that it is removed from the surface. The  $\text{Fe-NO}_3$  band at  $990 \text{ cm}^{-1}$  mirrors this trends, thus it is associated to  $(\text{Fe-O})_2\text{NO}$  as well.  $\text{Fe-O}_2\text{NO}$  is formed during plasma operation, but it increases further after the plasma is switched off.  $\text{Fe-NO}_2$  appears in the spectrum only after switching off the plasma. It could be a result of the gradual desorption as  $(\text{Fe-O})_2\text{NO} \Rightarrow \text{Fe-O}_2\text{NO} \Rightarrow \text{Fe-NO}_2$ . Yet, it also fits to the aforementioned argument that nitrites are

formed for low NO(g) exposure and nitrates at high NO(g) exposure [43]. Thus, the relation between the nitrite and nitrates is not yet fully understood.

Nitrates are mostly bound to the surface in the form of (Fe-O)<sub>2</sub>NO. When switching off the plasma, it is interchanged with Fe-O<sub>2</sub>NO. Both nitrates fully desorb once the reactor is evacuated. The formation of these surface-bound species follows the densities of the nitrogen oxides in the gas phase. Therefore, the formation of nitrogen oxides on the surface when sequentially igniting a pure O<sub>2</sub> or N<sub>2</sub> plasma is investigated next.

### 5.1.3 Chemical Looping: O<sub>2</sub> → N<sub>2</sub> Cycle

Nitrogen oxides are not natively formed by pure N<sub>2</sub> or O<sub>2</sub> plasmas themselves. Instead, the missing nitrogen or oxygen must be supplied by surfaces surrounding the plasma. These surfaces introduce a memory effect. N<sub>2</sub> or O<sub>2</sub> that is previously impregnated on the surface could be utilised to form NO<sub>x</sub> surface groups. Alternatively, nitrogen oxides can be formed in the gas phase when these previously impregnated species desorb, e.g. through sputtering.

In figure 5.7a, IRRAS spectra are presented when cycling between a pure O<sub>2</sub> and pure N<sub>2</sub> plasmas. The spectra near the end of the plasma-on phase are presented such that the impact of each plasma treatment can be studied. They are plotted above each other, and the order is labelled with Roman numerals. The surface is treated by a He+O<sub>2</sub> plasma before the first O<sub>2</sub> plasma treatment, i.e. spectrum (I) O<sub>2</sub>.

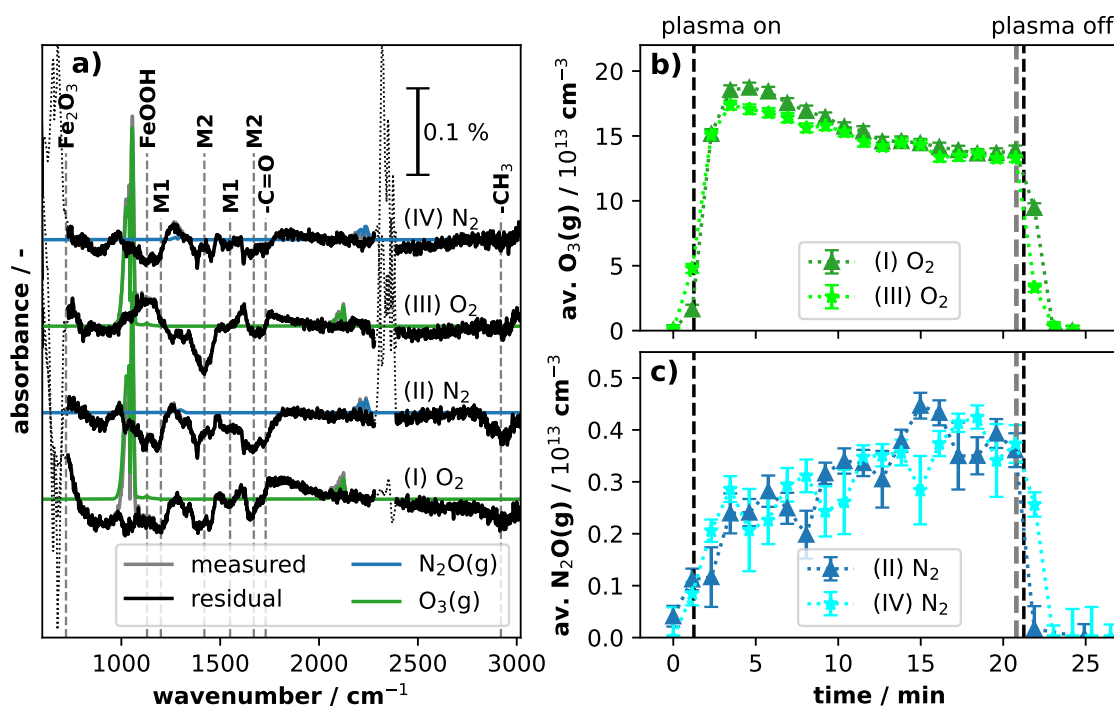


Figure 5.7: IRRAS spectra obtained when sequentially igniting pure O<sub>2</sub> and N<sub>2</sub> plasmas after 20 minutes of plasma ignition (a), and the gas phase densities of O<sub>3</sub> (b) and N<sub>2</sub>O (c) in time.

Spectrum I is identical to the final O<sub>2</sub> IRRAS spectrum of subfigure 5.1b. This spectrum shows the formation of Fe<sub>2</sub>O<sub>3</sub> and the removal of impurities from the surface. The average ozone density is estimated following the routine of the previous section. The density values are plotted in subfigure 5.7b. There, the timestamps when igniting and extinguishing the plasma are indicated with vertical black dashed lines and the time stamp of the spectra of a is indicated with the vertical grey dashed line.

Spectrum II and IV show the impact of a N<sub>2</sub> plasma. Impurities are removed and a minor contribution of FeOOH is observed [150]. The oxidation state of iron is not altered, because the Fe<sub>2</sub>O<sub>3</sub> band is not observed in the spectra. This fits with the typical surface cleaning, where N<sub>2</sub> is ineffective in reducing the surface.

In parallel, the N<sub>2</sub>O(g) is formed in the gas phase. The averaged N<sub>2</sub>O(g) density values are plotted in subfigure 5.7c. This production is linked to the previous oxidation of the surfaces surrounding the plasma, where oxygen is released through sputtering. The stable N<sub>2</sub>O(g) subsequently fills the volume of the reactor, hence the average density grows during plasma operation. Desorbing oxygen radicals present a finite oxygen source, thus the N<sub>2</sub>O(g) production should end once the surfaces are cleaned. This should impede the N<sub>2</sub>O(g) production given enough time, which is not the case in these plasmas. Also, the removal of iron oxides is not observed. Most likely, the oxide removal falls outside the observed spectral range.

The O<sub>2</sub> plasma spectrum (III) is obtained after igniting a N<sub>2</sub> plasma. It shows the reformation of FeOOH and removal of impurities that are similar to the earlier plasmas. The continued removal of the same impurities in these spectra show that the interference by these impurities is impossible to avoid. However, no nitrogen oxides can be identified as a result of this plasma treatment. The bands associated with the impurities make it impossible to identify any band to nitrates or nitrites.

The spectra show no significant formation of nitrates on the surface in either the pure oxygen or nitrogen plasmas. This reinforces the hypothesis that nitrates are formed through the adsorption of plasma produced nitrogen oxides. Next, a parameter study is performed to investigate the relation between gas species and the nitrate formation.

#### 5.1.4 Parameter Study

A parameter study is employed to investigate which processes are responsible for the nitrate formation. Changing the gas mixture has a profound impact on the NO<sub>x</sub> formation in the gas phase. It is, therefore, ideal when studying the relation of NO<sub>x</sub>(g) with the surface bound nitrates. However, changing the gas composition has a profound impact on the electrical characteristics of the plasma, thus this must first be understood. The intensity of the bridging bidentate nitrate at 1620 cm<sup>-1</sup> is the highest, therefore the most suitable for a parameter study.

##### Plasma power

The most apparent difference in the electrical characteristics when changing the gas mixture is found in the power-to-voltage curve. In figure 5.8, the plasma power with increasing rms voltage for different N<sub>2</sub>-to-O<sub>2</sub> gas flow ratio is presented.

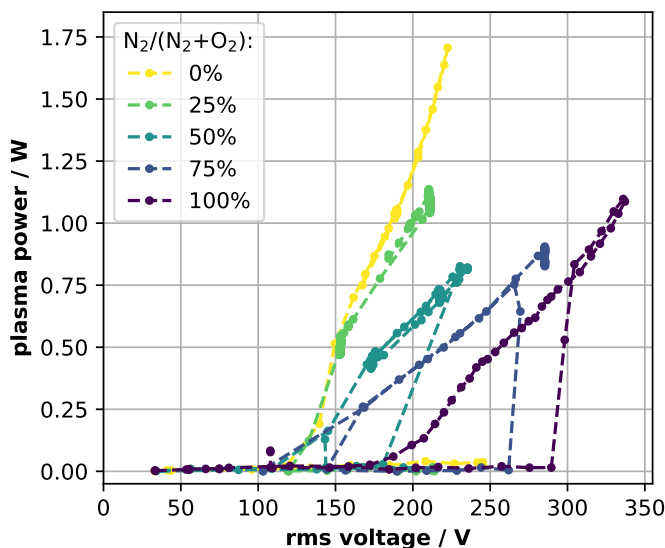


Figure 5.8: Plasma power to rms voltage curves for different gas mixtures.

A pure O<sub>2</sub> plasma ( $N_2/(N_2+O_2)=0\%$ ) ignites at the lowest voltage. The O<sub>2</sub> plasma initially ignites outside the electrodes as well, which is referred to as a parasitic discharge [144]. This does not happen in later measurements where the electric insulation of the wires connecting the electrodes to the IV-box are insulated with glass fibre instead of a polimide material (similar to Kapton). Interchanging O<sub>2</sub> with N<sub>2</sub> increases the required voltage to attain the same plasma power. This is also seen before with the He/N<sub>2</sub>/H<sub>2</sub> discharge in figure 4.1.

The impact of the plasma power on the gas densities and surface intensities is studied by continuously operating the plasma whilst varying the plasma power. This shortens the overall measurement time and minimises readsorbing impurities to affect the measurements. In figure 5.9, the gas phase densities and the (Fe-O)<sub>2</sub>=NO intensity are presented for a 10:10 sccm N<sub>2</sub>:O<sub>2</sub> gas flow mixture.

The plasma power is varied from 0.86 to 0.44 to 0.68 W to minimise the impact of hysteresis on the data. The plasma is operated for 20 minutes for each power value. The last 5 minutes are averaged and plotted in figure 5.10a. There, the densities and nitrate intensity are plotted with increasing plasma power. The uncertainty is estimated by combining the variation over these 5 minutes plus the average over the uncertainties of the individual data points. The gas phase densities are plotted on the left y-axis and the bridging bidentate nitrate (Fe-O)<sub>2</sub>NO intensity is plotted on the right y-axis.

All species show a positive relation with the plasma power. In particular, (Fe-O)<sub>2</sub>NO shows a linear relation with power. This must be considered in the next part, where the gas mixture is varied.

### Gas mixture

In figure 5.10b, the average gas phase densities and the intensity of the bidentate nitrate are plotted with increasing nitrogen admixture to the total gas mixture, which is expressed as the  $N_2/(N_2+O_2)$  gas flow ratio. The data points are obtained from

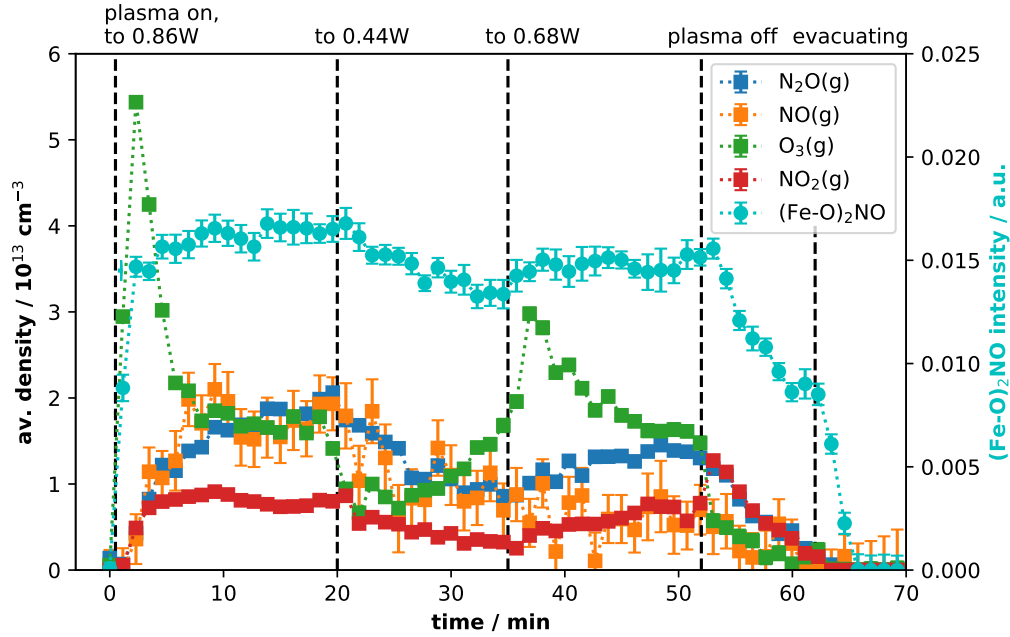
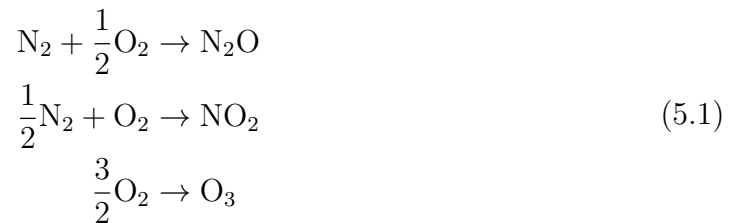


Figure 5.9:  $\text{NO}_x(\text{g})$  densities and nitrate intensity in time when varying the plasma power when controlling  $T_{surf}$  to  $40^\circ\text{C}$  during a 10+10 sccm  $\text{N}_2+\text{O}_2$  plasma.

individual plasma cycles, where the plasma is ignited for 20 to 25 minutes and the average is taken over the last 5 minutes of the plasma phase.

The measurements are obtained over several days, where a fresh iron foil is used per session. The plasma power is controlled between 0.8 and 1.0 W. Minor differences cannot be attributed to the plasma power alone. Rather, these are attributed to the uncertainty in the exact composition of the used foils, e.g. the poly crystalline structure and the level of impurities interfering with the measurements.

The trends of  $\text{N}_2\text{O}(\text{g})$ ,  $\text{NO}_2(\text{g})$ , and  $\text{O}_3(\text{g})$  follow the stoichiometric ratio of equation 5.1. This is indicated using the dashed lines in figure 5.10b. This is likely related to the high non-plasma volume inside the reactor. Active plasma produced radicals are confined to the plasma volume and do not contribute to the chemistry outside this volume.



The  $\text{NO}(\text{g})$  density follows a quadratic relation with the gas mixture, in contrast to the other gas species. This agrees with the values obtained earlier in an atmospheric  $\text{He}/\text{N}_2/\text{O}_2$  plasma [90]. They show that the  $\text{NO}(\text{g})$  density is strongly related to that of  $\text{O}_3(\text{g})$ . The ozone density decreases with increasing  $\text{N}_2$  admixture. This limits the oxidation of  $\text{NO}(\text{g})$  to  $\text{NO}_2(\text{g})$  for higher  $\text{N}_2/(\text{N}_2+\text{O}_2)$  ratios. Hence,  $\text{NO}(\text{g})$  density

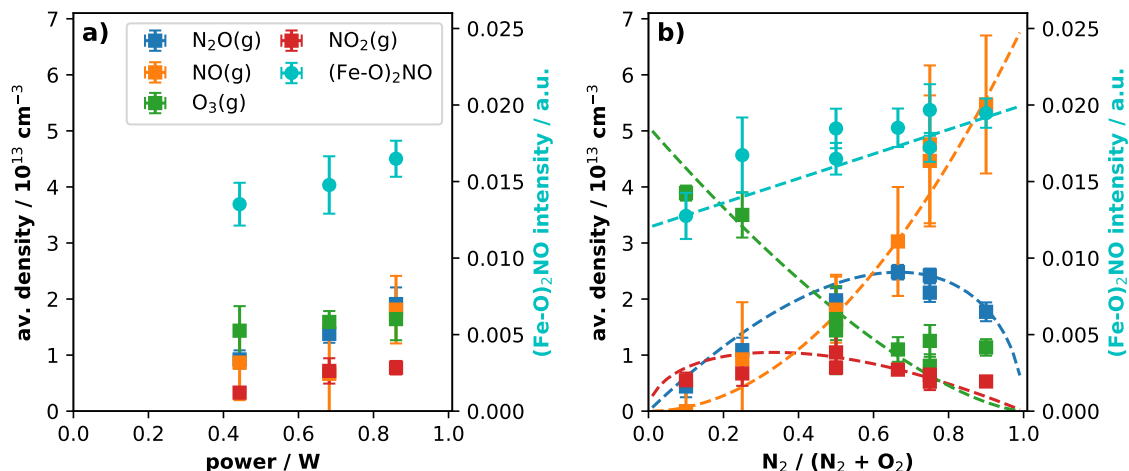


Figure 5.10: The NO<sub>x</sub>(g) densities and nitrate intensity as function of the plasma power (a) and the gas mixture (b) when controlling  $T_{surf}$  at 40 °C.

increases with  $N_2/(N_2+O_2)$ .

The bidentate nitrate intensity is less sensitive to the gas flow ratio. Nonetheless, it shows a linear increase with the N<sub>2</sub> admixture. This is similar to the NO(g) increase, thus a relation between the (Fe-O)<sub>2</sub>=NO intensity and NO(g) is observed.

Finally, the results in this section show the formation of nitrates on the iron substrate. The nitrate formation is correlated to the presence of plasma produced NO<sub>x</sub>(g) species. A positive relation between the intensity of the nitrates in the IRRAS spectra and the NO(g) densities is observed.

## 5.2 NH<sub>3</sub> Synthesis in N<sub>2</sub>+H<sub>2</sub> Plasma

The NH<sub>3</sub> synthesis on a plasma exposed iron foil is studied in this section. A similar methodology is used as in the previous section. The pretreatment is extended to a He+O<sub>2</sub> plasma and He+H<sub>2</sub> plasma treatment. This is deemed necessary since impurities interfere with NH<sub>x</sub> formation on the surface. The experiments focussed on identifying the presence of NH<sub>x</sub> intermediates on the surface in a N<sub>2</sub>/H<sub>2</sub> or N<sub>2</sub>/D<sub>2</sub> plasma. Interchanging H<sub>2</sub> with D<sub>2</sub> red shifts the NH<sub>x</sub>-bands with a factor of  $\sim 1/\sqrt{2}$ . This makes it useful to identify the origin of the formed bands.

### 5.2.1 Pretreatment

In figure 5.11, typical spectra are presented that are obtained during the pretreatment. First, a 200+20 sccm He+O<sub>2</sub> plasma is ignited. It proved effective in removing hydrocarbons and carbonyl impurities in the previous section. Yet, it also oxidises the surface, thus the surface must be reduced before NH<sub>3</sub> synthesis can be studied.

Second, a 200+20 sccm He+H<sub>2</sub> plasma is ignited for 2 to 3 hours. The substrate is reduced and carbonyl species are further removed, similar to the spectra presented in figure 5.2. This is seen in the negative absorbance Fe<sub>2</sub>O<sub>3</sub> band around 720 cm<sup>-1</sup>

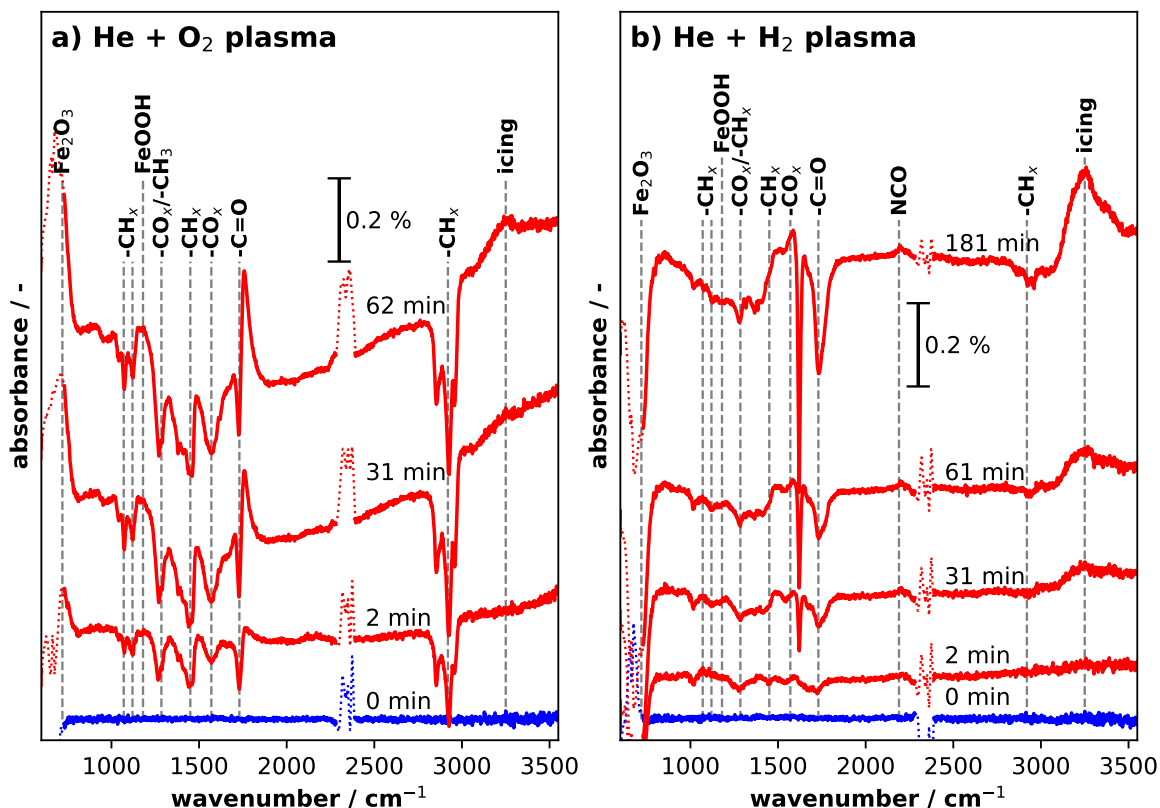


Figure 5.11: Reflectance spectra obtained during the He+O<sub>2</sub> plasma (a) and subsequent He+H<sub>2</sub> plasma (b).

and C=O band around 1730 cm<sup>-1</sup> [153, 167]. With time a new band at 2190 cm<sup>-1</sup> is observed. that is associated to NCO-group [168]. The sharp band around 1620 cm<sup>-1</sup> is a striking difference compared to the earlier presented He+H<sub>2</sub> plasma spectrum in section 5.1. This and the C=O band indicate the continuous removal of the respective surface groups. The linear trend is uninterrupted after 3 hours of igniting the He+H<sub>2</sub> plasma, and shows no indication of slowing down.

### 5.2.2 Identification of Reflection Spectra in 1:3 N<sub>2</sub>:H<sub>2</sub>

In figure 5.12, IRRAS spectra obtained during a 20 sccm H<sub>2</sub> plasma are presented. The plasma is ignited for 30 minutes. During operation, negative absorption bands are observed between 1100 and 1800 cm<sup>-1</sup> and at 2930 cm<sup>-1</sup>. These fingerprint region bands are fitted to estimate their behaviour in time. The outcome of a fitted spectrum is given in subfigure b and the intensities are plotted in time in subfigure c.

The negative absorption bands are similar to those observed during the He+H<sub>2</sub> plasma. The bands at 1180, 1290, 1410, and 1730 cm<sup>-1</sup> are approximated with a Gaussian line shape using a FWHM of 25, 140, 70, and 60 cm<sup>-1</sup>, respectively. The band at 1180 cm<sup>-1</sup> is associated with FeOOH. The band around 1290 cm<sup>-1</sup> is very broad because it is a combination of carbonyl and hydrocarbon groups. The bands at 1410 and 2930 cm<sup>-1</sup> are associated with the scissoring  $\delta$  and stretch  $\nu$  mode of CH<sub>2</sub>

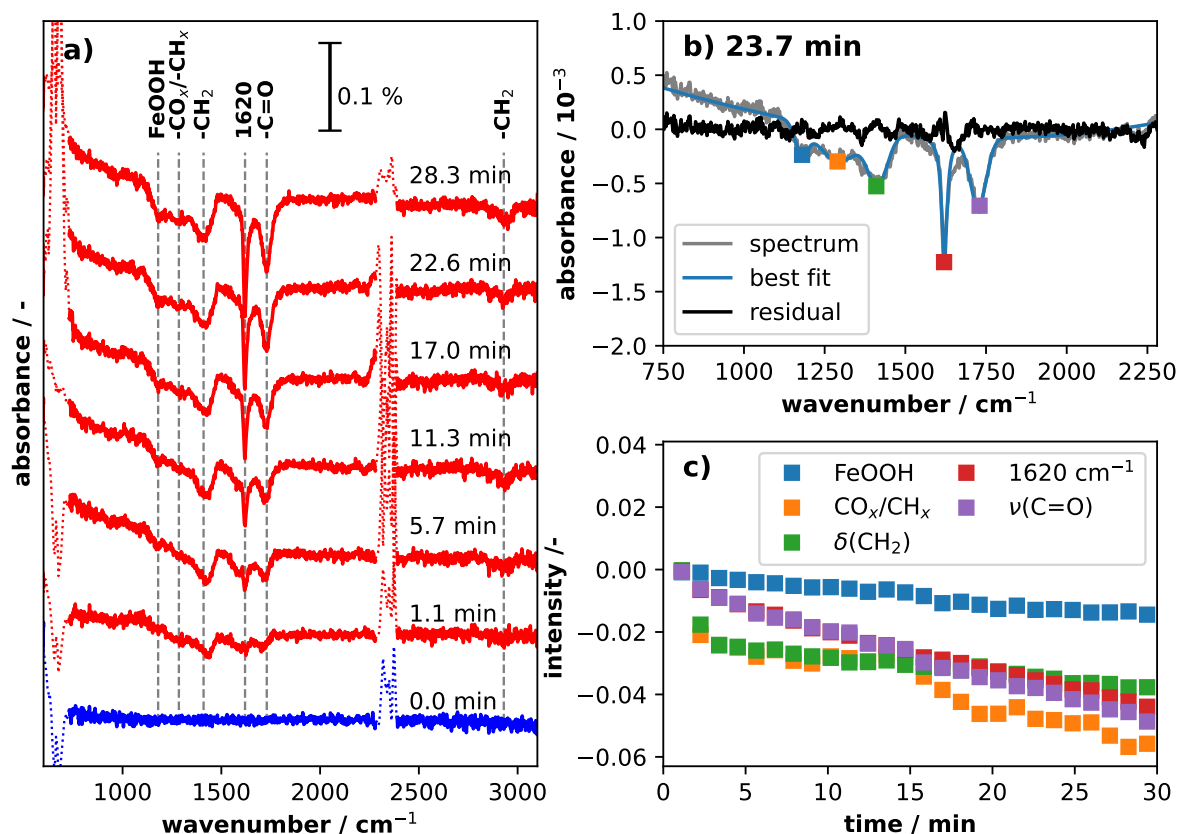


Figure 5.12: IRRAS spectra obtained during a 20 sccm H<sub>2</sub> plasma (a). The spectra show different contributions (b) that are tracked in time (c).

[147]. The band at 1730 cm<sup>-1</sup> with C=O stretch.

In subfigure 5.12c, the intensities of these bands are plotted in time. The removal of FeOOH and  $\delta(\text{CH}_2)$  occur at the same speed, which is evident of the slope of the intensity with time. The removal of C=O band occurs at a higher speed, which is evident from the steeper slope. Since the  $-\text{CO}_x + -\text{CH}_x$  band is a combination of both hydrocarbon and carbonyl components, it initially follows that of  $\delta(\text{CH}_2)$  and later that of C=O.

The 1620 cm<sup>-1</sup> band is approximated by a Lorentzian line shape with FWHM of 20 cm<sup>-1</sup>. This lineshape better encapsulates the narrow peak head than a Gaussian. The difference in the lineshape is striking, since up to now all bands observed in this chapter are well described by a Gaussian lineshape.

However, the origin of this band is still unclear. It is not seen during earlier He+H<sub>2</sub> plasma, which is presented in figure 5.2. Therefore, it is unlikely to be associated with a carbonyl group, since these are already observed under other conditions and behave different. It is very unlikely to be nitrates as well, despite they spectrally overlap. The intensity is many times greater than observed in the previous N<sub>2</sub>+O<sub>2</sub> measurements. Alternatively, it can be associated to FeOOH, but it follows a different trend at the already identified FeOOH band at 1180 cm<sup>-1</sup> [169]. The band could be due to the scissoring mode of "freely" bound H<sub>2</sub>O [149, 170, 171]. However, water should also yield a stretch band around 3400 cm<sup>-1</sup> that is not observed [172]. Therefore, the origin

of this band remains elusive here.

### $N_2+H_2$ plasma

The gas mixture is changed from 20 sccm  $H_2$  to 15+5 sccm  $H_2+N_2$  whilst continuing to operate the plasma. This minimises the readsorption of impurities on the substrate. In figure 5.13, IRRAS spectra obtained during  $N_2+H_2$  gas flow are presented. A new reference spectrum is obtained before changing the gas mixture, see *0.0 min* spectrum.

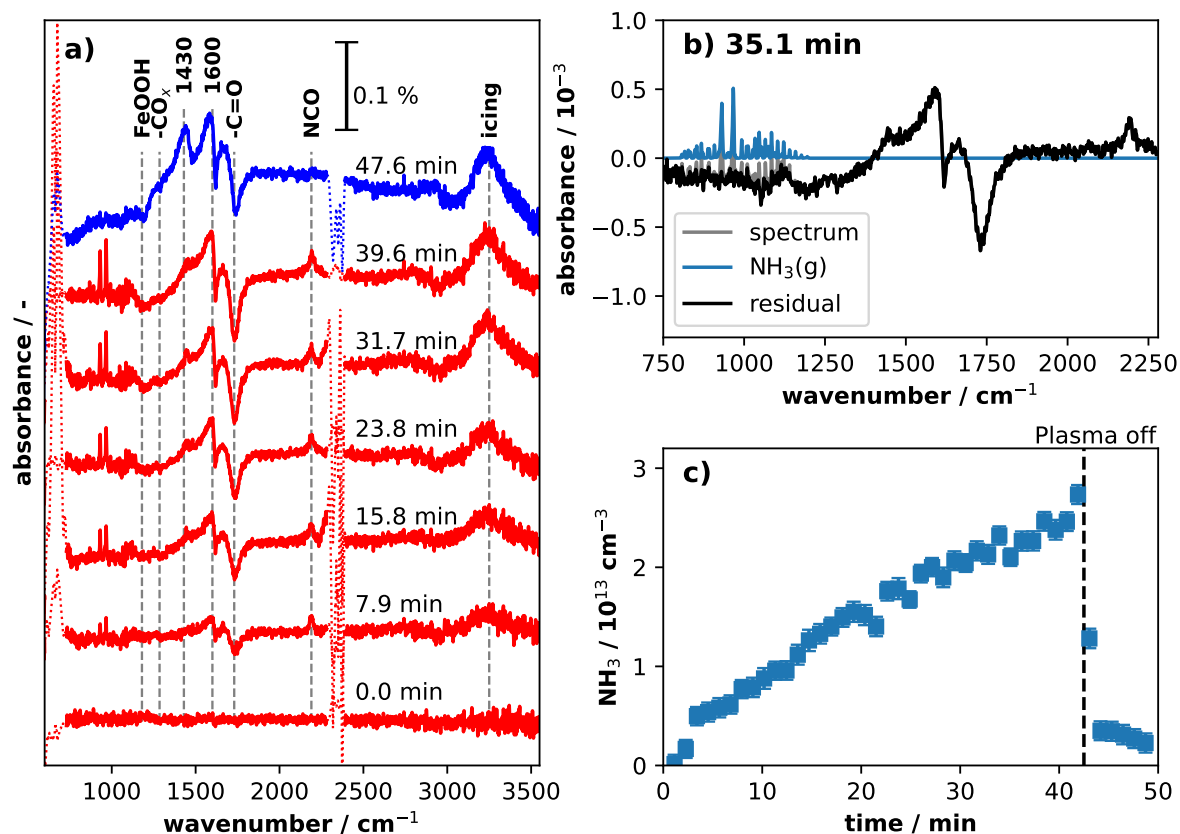


Figure 5.13: IRRAS spectra obtained during a 15 sccm  $H_2 + 5$  sccm  $N_2$  plasma (a). The  $NH_3(g)$  contribution is fitted (b) and its densities is tracked in time (c).

After admixing  $N_2$  to the  $H_2$  gas stream,  $NH_3(g)$  is observed alongside a NCO band at  $2190\text{ cm}^{-1}$  and new band at  $1580\text{ cm}^{-1}$ . The  $NH_3(g)$  absorption feature is fitted using the routine used for the  $NO_x(g)$  analysis in section 5.1.2. A typical spectral fit is presented in subfigure 5.13b. The gas-phase density in time is plotted in subfigure c.

The near-linear increase of  $NH_3(g)$  density with time is due to a convolution of the changing gas mixture, which affects the formation process, and the diffusion to and adsorption on inner walls of the reactor. The residence time of the gas is about 5.8 minutes, thus the gas composition should resemble the 1:3  $N_2:H_2$  ratio after 20 minutes. Hence, the  $NH_3$  production rate should be stable after 20 minutes. In addition, following the behaviour of  $N_2O(g)$ , another 20 minutes can be expected from the diffusion into the non-plasma regime of the reactor. Yet, the  $NH_3(g)$  density continuously increases up to 43 minutes. This is attributed to the adsorption to the inner walls of

the reactor vessel. Such a process is seen during the *ex-situ* multipass FTIR absorption measurements in figure 4.5 of section 4.2.

The band around 1580 cm<sup>-1</sup> could be associated with  $\delta(\text{NH}_2)$  [173, 174]. However, it could also be explained by a COO and H<sub>2</sub>O band. The latter can be omitted on basis of the absence of any OH-stretch bands, but the COO cannot.

The NCO band at 2190 cm<sup>-1</sup> is again observed [168]. It is formed during plasma operation and disappears once the plasma is off. This is another sign that impurities such as CO<sub>x</sub> species are still present in the reactor and reacting on the surface.

The band around 1430 cm<sup>-1</sup> is previously associated to  $\delta(\text{CH}_2)$ . However, it regrows after switching off the plasma unlike the  $\nu(\text{CH}_2)$  band around 2900 cm<sup>-1</sup>. This hints that the attribution to  $\delta(\text{CH}_2)$  is incorrect here.

### Replacing H<sub>2</sub> with D<sub>2</sub>

The measurement is repeated with deuterium to investigate potential isotope shifts of the previously observed bands. The plasma with 20 sccm D<sub>2</sub> is ignited after cleaning the surfaces following the aforementioned pretreatment steps. After 30 minutes of D<sub>2</sub> plasma operation, a new reference spectrum is taken and the gas mixture is changed to 15 + 5 sccm D<sub>2</sub>+N<sub>2</sub>. Finally, the gas mixture is changed to H<sub>2</sub>+N<sub>2</sub> after 50 minutes of D<sub>2</sub>+N<sub>2</sub> plasma ignition. The resulting spectra of this sequence are plotted in figure 5.14a. The D<sub>2</sub> spectrum is obtained after 25 minutes of plasma ignition and the N<sub>2</sub>+D<sub>2</sub> and N<sub>2</sub>+H<sub>2</sub> after 45 minutes of igniting the plasma at the respective gas mixtures.

The D<sub>2</sub> plasma ignition yields a very similar IRRAS spectra to that of a H<sub>2</sub> plasma, see figure 5.14b. Both spectra only show the removal of impurities. Introducing nitrogen to the D<sub>2</sub> gas stream affects the IRRAS spectra also similar to the N<sub>2</sub>+H<sub>2</sub> counterpart. Only a stronger FeOOH-band is observed.

The pretreatment with a H<sub>2</sub> mixture dosed the surfaces surrounding the plasma with hydrogen. Hydrogen is known to penetrate into metals. Thus, during the D<sub>2</sub> containing plasmas, the hydrogen might diffuse out of the surfaces and contribute to the plasma chemistry. Since hydrogen is lighter than deuterium by a factor of 2, hydrogen radicals react faster than that of deuterium. Therefore, using D<sub>2</sub> instead of H<sub>2</sub> yields very similar results.

On another note, the presence of deuterium is verified in less defined conditions where more oxygen impurities remained in the system. The formation of the  $\nu(\text{O-D})$  stretch at 2740 cm<sup>-1</sup> was observed [175]. Yet, N<sub>2</sub>O(g)-like absorption band around 2220 cm<sup>-1</sup> is seen in the spectrum of subfigure 5.14c. The observed band is wider than the previously noted 2190 cm<sup>-1</sup> band thus is notably different. This indicates that the observed band is indeed N<sub>2</sub>O(g). It indicates that impurities play a role in the chemistry

The spectra presented in this section show an inconclusive picture of the surface composition on NH<sub>x</sub> formation. Whilst many bands can be associated with the removal of impurities, the presence of NH<sub>x</sub> intermediates can not be identified. The only candidate remains the broad band around 1580 cm<sup>-1</sup>.

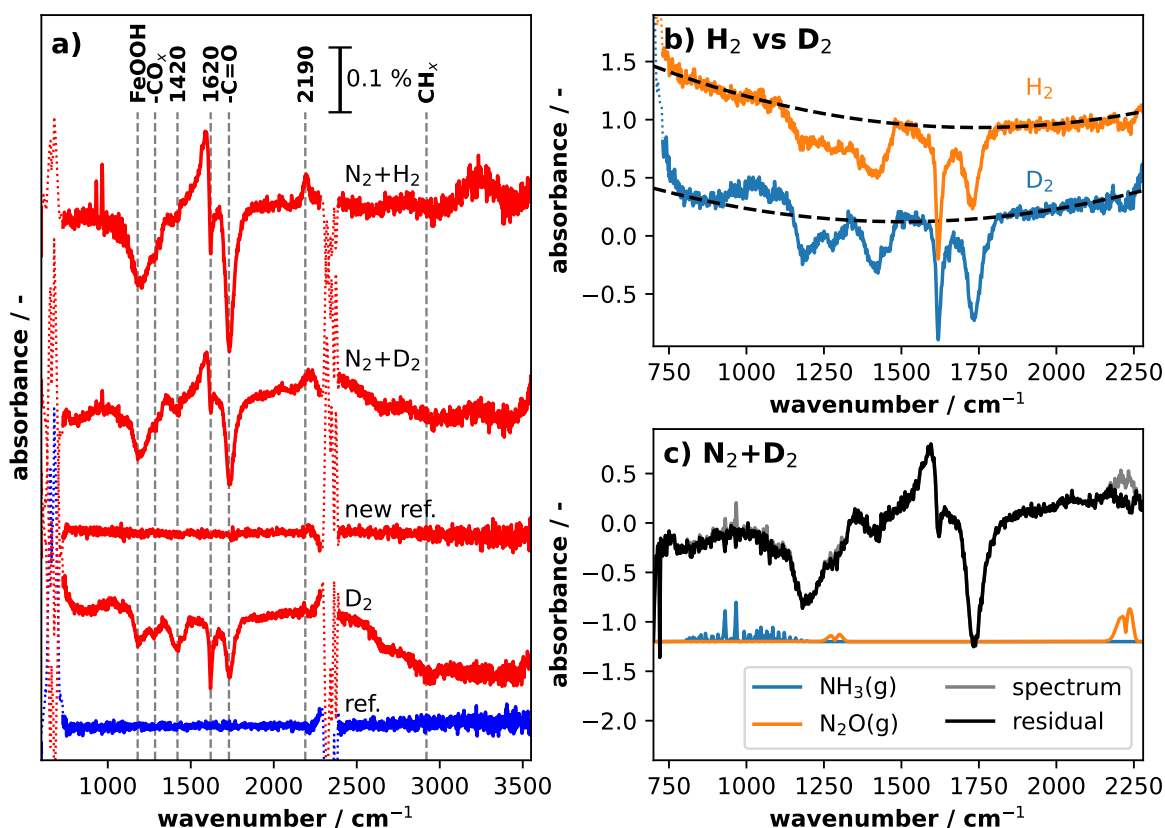


Figure 5.14: IRRAS spectra acquired during the  $D_2 \rightarrow N_2+D_2 \rightarrow N_2+H_2$  plasma ignition (a), the comparison of the  $H_2$  and  $D_2$  spectra (b), and the identification contributions in the  $N_2+D_2$  plasma (c).

## 5.3 Discussion

### $NO_x$ formation at a plasma-surface interface

The absence of other nitrogen oxide surface groups hints at the strong oxidising nature of the  $N_2+O_2$  plasma. When an iron zeolite is dosed by only  $NO(g)$ , then only  $NO^+$  and nitrosyl  $-(NO)_{1,2}$  groups are formed [39, 40, 158, 164, 165]. Nitrites and nitrates are only formed when adding  $O_2$  to the gas mixture. Yet, this occurs along side the formation of the  $NO^+$ , nitrosyls, and  $N_2O_4$ . Similarly, the adsorption of  $NO_2(g)$  produces mainly nitrites/nitrates, but other nitrogen oxide groups as well. Only when dosing metals oxides (e.g.  $Al_2O_3$ ) with  $NO_2$  are nitrites/nitrates exclusively formed [154, 176]. Therefore, the  $N_2+O_2$  plasma IRRAS spectra presented in this chapter are very similar to oxygen rich environments. This fits to the picture where the chemistry in such a plasma is mostly dictated by oxygen radicals [33].

The  $NO_x$  measurements show that nitrates quickly disappear once the plasma is switched off, e.g. see figure 5.6b. However, literature describes that surface-bound nitrates are especially stable. At least 500 K is needed before it starts desorbing [39, 177]. For instance, the activation barrier of bidentate nitrate is 170 to 250  $\text{kJ mol}^{-1}$  when desorbing as either  $NO_2(g)$  or  $NO(g)$  [178]. At the maximum measured substrate temperature of 40 °C, the desorption rate is basically zero. Yet, the removal is observed

in the experiments. Thus, another reaction path must remove the nitrates from the substrate.

The oxidation of plasma products can explain the observed high nitrate removal rate. Molecules such as  $\text{N}_2\text{O}$ ,  $\text{NO}$ , and  $\text{O}_3$  can further oxidise to produce  $\text{N}_2$ ,  $\text{O}_2$ ,  $\text{NO}$ , and  $\text{NO}_2$ . This may occur over the surface where an oxygen atoms is transferred from the nitrite and nitrates to the plasma products. For instance, literature mentions that nitrites and nitrates are effective in oxidising nitrous oxide [160, 178]. This would reduce the nitrate towards nitrites and eventually remove the nitrites as well. This transformation is observed in the experiments. The nitrites only appear once the plasma is switched off and the intensity of the bridging bidentate nitrate decreases. However, the experiments do not show any impact on the decay of the gaseous plasma products. The small surface area of the iron substrate compared to the other inner walls of the reactor likely obscures the impact of the surface chemistry on the gas phase composition. Another reactor design is needed to test this hypothesis.

Alternatively, the readsorption of impurities might stimulate the nitrate desorption rate by opening up alternative chemical pathways. Lobree et al. found that the desorption of nitrates occurred at lower temperatures when exposing the substrate to propane instead of helium [39]. They propose that the propane reacts with the nitrates to form a  $\text{C}_x\text{H}_y\text{NO}$ -group. This provides an alternative chemical pathway with a lower reaction barrier.

On a similar note, water impurities might lower desorption barrier as well. Evidence of this is seen in literature. The sufficient  $\text{NO}(\text{g})$  presence enhances  $\text{N}_2\text{O}(\text{g})$  decomposition over an iron zeolite substrate, e.g. see [158]. This is explained by Heyden et al. as follows [178]: The adsorption of water prevails under normal conditions. This deactivates surface sites by forming the  $\text{Fe}(\text{OH})_2$ -groups.  $\text{NO}(\text{g})$  reacts with these groups to produce  $\text{HNO}_2$  that readily desorbs, thereby re-activating the sites for  $\text{N}_2\text{O}(\text{g})$  decomposition. In our case, the reverse process might apply. Water impurities are reintroduced after switching off the plasma. They could react with adsorbed nitrates to produce the readily desorbing  $\text{HNO}_2$ . Thereby, the reintroduction of water impurities opens-up an alternative desorption path for the nitrates.

In our work, the experiments show that impurities are removed by plasma operation and readsorb once the plasma switched off. The readsorbing impurities can open-up alternative pathways with a lower reaction barrier as just mentioned. Thereby, the high desorption energy barriers for the classical  $\text{NO}_3$  desorption is circumnavigated.

### Difficulty in interpreting IRRAS spectra from $\text{N}_2+\text{H}_2$ plasma operation

The IRRAS spectra yield non-unique absorption features. Unlike in the gas phase where all rotational-vibrational transitions are well known and documented, the central wavenumbers of the very same surface group differs as function of the substrate material, crystalline structure, and surrounding surface composition. Sälli et al. showed that the perturbation in the stretch and bending modes of  $\text{NH}_3$  adsorbed on different transition metals changes as function of the binding energy of  $\text{NH}_3$  with the surface [124]. Iyngaran et al. observed a change in the symmetric bending mode of  $\text{NH}_3$  on iron as function of dosing, preadsorption with potassium, and oxidation degree of an iron substrate [179, 180]. Therefore, the observed absorption features must be carefully compared to the spectra presented in literature.

Identifying the  $\text{NH}_x$ -intermediates on the surface is difficult. This is seen in this chapter as well as mentioned by Cha et al. [181]. The radical generation by the plasma overtakes many rate limiting steps that typically exist during thermal processes, e.g. the need of dissociating  $\text{N}_2$  on the surface. Winter et al. performed Diffuse reflectance IR Fourier transform spectroscopy (DRIFTS) measurements on a volume DBD setup using  $\text{Al}_2\text{O}_3$  beads that are coated by either Ni or Fe [182]. They observe distinct peaks around 1200, 1600, and 2100  $\text{cm}^{-1}$ . They attribute these peaks to  $\text{NH}_x$  intermediates (1200 and 1600  $\text{cm}^{-1}$ ) and to the N=N stretch (around 2200  $\text{cm}^{-1}$ ). Bands at similar spectral positions are observed during the  $\text{N}_2+\text{H}_2$  plasma of section 5.2. However, the 1200  $\text{cm}^{-1}$  band is attributed to FeOOH instead of  $\text{NH}_x$  intermediates. On the same note, the other two bands are also associated with the scissoring mode of  $\text{H}_2\text{O}$  adsorbed on  $\text{Al}_2\text{O}_3$  and the bending, frustrated rotation, and hindered translation of  $\text{Al}_2\text{O}_3$  itself, respectively [171]. Lee et al. combined polarisation-modulation IRRAS, XPS, and DFT calculations to identify the origin of the 2200  $\text{cm}^{-1}$  and found that NCO is the likely candidate [168]. Therefore, the identification of  $\text{NH}_x$  species on the  $\text{Al}_2\text{O}_3$  beads and the metallic iron substrate of this thesis is questionable.

The strongest IR absorption band of adsorbed  $\text{NH}_3$  occurs around 1100  $\text{cm}^{-1}$ , which is observed at cryogenic temperatures [179, 180]. However, following the kinetic studied on  $\text{NH}_3$  production, it should readily desorb at room temperature and above. Therefore, it is rather unlikely to exist on the studied substrate, see kinetic model used in the last chapter.

# Chapter 6

## Conclusion and Outlook

### 6.1 Conclusion

The work presented in this thesis focusses on understanding different aspects of introducing a catalyst to a plasma. It is investigated with two different experiments. First, the plasma catalytic ammonia synthesis is studied in an atmospheric helium RF plasma. Second, the surface composition is examined at a plasma-surface interface.

#### Surface enhanced plasma operation

Ammonia synthesis from  $N_2$  and  $H_2$  is a complex process. The stable reactants must be dissociated and carefully reordered to form  $NH_3$ . On the one hand, the mean electron energy should be high enough to dissociate  $N_2$ . On the other hand, electron impact dissociation of  $NH_3$  and  $NH_x$  intermediates should be minimised. The intricate interplay between forward and backward reactions was observed in chapter 4.

After a careful comparison of experiments and a global kinetic model, it became clear that the nitrogen dissociation is the main limiting factor in the used plasma source. A positive relation of the  $NH_3$  molar fraction with increasing power is observed. It shows that increasing the electron density enhances the synthesis through increasing the  $N_2$  dissociation rate more than destroying  $NH_3$  through electron impact reactions.

Having established how the  $N_2$  dissociation is the rate limiting factor for the  $NH_3$  synthesis, the impact of a catalytic coating is investigated. Copper, iron, and platinum nano particles are coated on the glass plates, without affecting either the gas flow or the plasma operation mode. An increase in the conversion and efficiency of the  $NH_3$  synthesis is observed. Iron presented the greatest impact at  $H_2/(N_2+H_2)$  ratios below 80%. The quadratic trend of  $NH_3$  fraction with  $H_2/(N_2+H_2)$  for the blank experiment changed to a linear relation with the iron coating.

The chemistry model expected a decrease in the  $NH_3$  production when introducing the metallic coating, in contrast to the experimentally observed increase. The hydrogen abstraction rate is higher on metals than for glass. This constitutes a back-reaction, hindering the  $NH_3$  production.

The contradiction suggests that the plasma conditions are altered by the surface coating. Only a small increase in  $E/N$  is enough to explain the observed enhancement in  $NH_3$  production. It is proposed that this originates from a lower secondary electron

emission coefficient for metals than for dielectrics. The fewer secondary electrons are generated, the more ionisation inside the plasma should occur to maintain the plasma. Thus, the plasma conditions are improved by the metallic coating rather than the coating enabling alternative (more efficient) chemical pathways.

### Plasma induced surface reactions

The surface composition of an iron foil is studied *in operando* using IRRAS. The removal of hydrocarbon and carbonyl groups are positively identified during the pre-treatment. Their contribution to the reflection spectra and surface chemistry can be minimised by treating the substrate with a He/O<sub>2</sub> and He/H<sub>2</sub> plasmas.

The N<sub>2</sub>/O<sub>2</sub> plasmas show the formation of nitrates and nitrites on the surface and N<sub>2</sub>O, NO, NO<sub>2</sub>, and O<sub>3</sub> in the gas phase. The fact that only nitrates are observed on the surface during plasma operation is striking. It shows that the plasma creates a strongly oxidising environment. The results are very similar to the NO<sub>2</sub>/O<sub>2</sub> exposure on metal oxides without plasmas, where also only nitrates are observed.

The gas composition is controlled by the N<sub>2</sub>-to-O<sub>2</sub> gas ratio. The N<sub>2</sub>O(g), NO<sub>2</sub>(g), and O<sub>3</sub>(g) densities follow their respective stoichiometric ratio. This is not the case for NO and the surface-bound nitrates. Instead, they both increase with N<sub>2</sub>/(N<sub>2</sub> + O<sub>2</sub>). Their correlation indicates that nitrate production at the surface is related to the nitric oxide presence in the gas phase. Therefore, the nitrates are most likely formed by NO(g) adsorption followed by the oxidation by plasma produced oxygen radicals.

After plasma operation, the nitrates readily disappear from the surface. The binding configuration changes from bridging to chelating bidentate nitrate, and nitrite appears in the spectrum. This cannot be explained through a typical desorption process, since nitrates are strongly bound to the surface. Rather, secondary reactions with plasma products or impurities open up alternative pathways that allow the fast desorption of nitrates. This requires further experimenting to fully understand which reactions are responsible for this observation.

In contrast, the N<sub>2</sub>/H<sub>2</sub> plasma experiments are less fruitful. The spectra continue to be plagued by absorption bands associated to impurities rather than to NH<sub>x</sub> intermediates. Further improvements to the setup are needed to reduce the impact of these impurities. For instance, removing the presence of oxygen impurities in the form of FeOOH and carbonyl groups. The successful identification of N<sub>2</sub>/H<sub>2</sub> plasma induced intermediates will be possible once the absorption features are better spectrally isolated.

## 6.2 Outlook

IRRAS is an appropriate technique to *in operando* study the surface composition, but it should be complemented with other diagnostics or DFT calculations, similar to [168]. This helps with the identification of NO<sub>x</sub> and NH<sub>x</sub> intermediates adsorbed at the iron foil. Literature presents a great scala of vibrational bands but they are all observed for different substrates. This affects the respective spectral positions and increases the ambiguity of the interpretation of the spectra.

Alternatively, the experiment can be further simplified: I) The plasma could be operated at even lower pressures such that the impurity level can be better controlled. However, this will move the plasma conditions even further from typical atmospheric pressure conditions at which plasma-catalysis is studied. II) A silicon wafer with a defined crystalline structure can be used instead. The variability by the presence of different crystalline structures is minimised. The oxidation and hydrogenation of the surface can be better studied as well, since the corresponding absorption bands lie within the detectable spectral range. The downside of this simplification is the lack of novelty. The interaction of silicon wafers with plasmas is widely studied in literature. Granted these studied focus on other applications, e.g. solar cell fabrication [101].

In-plasma catalysis does not live-up to the promised increase in the yield and energy efficiency. Instead, more and more studies highlight the impact of the surface material on the plasma operation itself [143]. This means that in-plasma catalysis should focus on finding materials that optimise the plasma conditions rather than opening-up chemical pathways with surface processes.

Post-plasma catalysis is another interesting point of study. It is promised to combine the advantages of exciting the reactants without doing the exact same for the products. For instance, a cycling system can produce  $\text{NH}_3$  in two steps: 1) formation of nitrates on a substrate by  $\text{NO}/\text{O}_2$  adsorption; 2) exposure by  $\text{H}_2$  at mild conditions to reduce the nitrates to  $\text{NH}_3$  [183, 184]. The first step can be performed by a  $\text{N}_2/\text{O}_2$  plasma as it can readily form the  $\text{NO}(\text{g})$  and  $\text{NO}_2(\text{g})$  species needed to produce the nitrates. The nitrate production is observed in this thesis, but the binding lacks stability in the aftermath of the plasma. Therefore, it is interesting to investigate how to increase the stability of these nitrates, so they can be utilised in subsequent steps.

# Appendix A

## Chemistry set He/N<sub>2</sub>/H<sub>2</sub> plasma

Most of the reactions are originate from Carrasco et al. since they are also used by other publications [31], e.g. Hong et al. [32]. The electron impact reactions of the H<sub>2</sub> and NH<sub>3</sub> dissociation are updated. The equations as function of the electron temperature  $\hat{T}_e$  are replaced to cross section sets, which fit better to the non-maxwellian EEDFs used for our case. The dissociation of H<sub>2</sub> by electron impact is included by considering the electronic excitation to H<sub>2</sub>( $b^3\Sigma_u^+$ ), which is a repulsive state readily dissociates [185]. The cross sections for the NH<sub>3</sub> cracking are obtained from the Hayashi database [56].

Three-body reactions used only for He as non-reacting partner, for one reaction Ar is used as He could not be found. N + H<sub>2</sub>  $\longrightarrow$  NH + H is not considered since it requires electronically excited H<sub>2</sub>, which should not be significant due to the atmospheric pressure and low mean electron energy.

The de-excitation of He\* back to He is simplified. In actuality, reaction R9 and R10 do not produce He, but rather He<sub>2</sub>\* or He<sub>2</sub><sup>+</sup> [50]. These dimers later relax back to He through collisional relaxation such as He<sub>2</sub>\* + M  $\longrightarrow$  2 He + M or charge transfer reactions. These relaxation processes are generally very fast. Hence, the model is simplified by considering as He\* + 2 He  $\longrightarrow$  He<sub>2</sub>\* + He  $\longrightarrow$  3 He.

Table A.1: Volume processes, where the gas temperature  $T_g$  is given in K, the electron temperature  $\hat{T}_e$  is given in eV, and the reference temperature  $T_0 = 300$  K.

#	reaction	rate coefficient / $\text{cm}^3\text{s}^{-1}$ , $\text{cm}^6\text{s}^{-1}$	reference
Electron induced reactions			
R1	$e^- + \text{H}_2 \longrightarrow e^- + 2\text{H}$	$f(E/N)$	[55]
R2	$e^- + \text{N}_2 \longrightarrow e^- + 2\text{N}$	$f(E/N)$	[55]
R3	$e^- + \text{He} \longrightarrow e^- + \text{He}^*(=2\ ^3\text{S})$	$f(E/N)$	[54]
R4	$e^- + \text{NH} \longrightarrow e^- + \text{N} + \text{H}$	$5.0 \times 10^{-8} \cdot \hat{T}_e^{0.5} \cdot e^{-8.6/\hat{T}_e}$	[31]
R5	$e^- + \text{NH}_2 \longrightarrow e^- + \text{N} + \text{H}_2$	$5.0 \times 10^{-8} \cdot \hat{T}_e^{0.5} \cdot e^{-7.6/\hat{T}_e}$	[31]
R6	$e^- + \text{NH}_2 \longrightarrow e^- + \text{NH} + \text{H}$	$5.0 \times 10^{-8} \cdot \hat{T}_e^{0.5} \cdot e^{-7.6/\hat{T}_e}$	[31]
R7	$e^- + \text{NH}_3 \longrightarrow e^- + \text{NH} + \text{H}_2$	$f(E/N)$	[56]
R8	$e^- + \text{NH}_3 \longrightarrow e^- + \text{NH}_2 + \text{H}$	$f(E/N)$	[56]
2 body Neutral-neutral reactions			
R9	$\text{He}^* + 2\text{He} \longrightarrow 3\text{He}$	$2 \cdot 10^{-34}$	[50]
R10	$2\text{He}^* \longrightarrow 2\text{He}$	$1.5 \cdot 10^{-9}$	[50]
R11	$\text{He}^* + \text{N}_2 \longrightarrow \text{He} + 2\text{N}$	$5 \cdot 10^{-11}$	[50]
R12	$\text{He}^* + \text{N}_2 + \text{He} \longrightarrow 2\text{N} + 2\text{He}$	$3.3 \cdot 10^{-30}$	[64]
R13	$\text{N} + \text{H}_2 \longrightarrow \text{NH} + \text{H}$	$4 \cdot 10^{-10} \cdot (T_g/T_0)^{0.5}$	[138]
R14	$\text{N} + \text{NH} \longrightarrow \text{H} + \text{N}_2$	$5 \cdot 10^{-11}$	[29]
R15	$\text{H} + \text{NH} \longrightarrow \text{N} + \text{H}_2$	$5.4 \cdot 10^{-11} \cdot e^{-165/T_g}$	[29]
R16	$\text{NH} + \text{NH} \longrightarrow \text{H}_2 + \text{N}_2$	$5 \cdot 10^{-10} \cdot (T_g/T_0)$	[29]
R17	$\text{NH} + \text{NH} \longrightarrow \text{N}_2 + 2\text{H}$	$8.5 \cdot 10^{-11}$	[29]
R18	$\text{NH} + \text{NH} \longrightarrow \text{N} + \text{NH}_2$	$1.7 \cdot 10^{-12} \cdot (T_g/T_0)^{1.5}$	[29]
R19	$\text{H} + \text{NH}_2 \longrightarrow \text{H}_2 + \text{NH}$	$6.6 \cdot 10^{-11} \cdot e^{-1840/T_g}$	[29]
R20	$\text{N} + \text{NH}_2 \longrightarrow \text{N}_2 + \text{H}_2$	$1.2 \cdot 10^{-10}$	[29]
R21	$\text{H}_2 + \text{NH}_2 \longrightarrow \text{NH}_3 + \text{H}$	$5.4 \cdot 10^{-11} \cdot e^{-6492/T_g}$	[29]
R22	$\text{NH} + \text{NH}_2 \longrightarrow \text{NH}_3 + \text{N}$	$1.66 \cdot 10^{-12}$	[29]
R23	$\text{H} + \text{NH}_3 \longrightarrow \text{NH}_2 + \text{H}_2$	$8.4 \cdot 10^{-14} \cdot (T_g/T_0)^{4.1} \cdot e^{-4760/T_g}$	[29]
3 body Neutral-neutral reactions			
R24	$\text{H} + \text{H} + \text{Ar} \longrightarrow \text{H}_2 + \text{Ar}$	$6.4 \cdot 10^{-33} \cdot (T_g/T_0)^{-1}$	[186]
R25	$\text{N} + \text{N} + \text{He} \longrightarrow \text{N}_2 + \text{He}$	$2.5 \cdot 10^{-32} \cdot (T_g/T_0)^{0.33}$	[64]
R26	$\text{H} + \text{N} + \text{M} \longrightarrow \text{NH} + \text{M}$	$10^{-33}$	[29]
R27	$\text{N} + \text{H}_2 + \text{M} \longrightarrow \text{NH}_2 + \text{M}$	$1 \cdot 10^{-34}$	[29]
R28	$\text{H} + \text{NH} + \text{M} \longrightarrow \text{NH}_2 + \text{M}$	$1 \cdot 10^{-32}$	[29]
R29	$\text{H} + \text{NH}_2 + \text{M} \longrightarrow \text{NH}_3 + \text{M}$	$5.5 \cdot 10^{-30}$	[29]
R30	$\text{NH} + \text{H}_2 + \text{M} \longrightarrow \text{NH}_3 + \text{M}$	$2.5 \cdot 10^{-35} \cdot (T_g/T_0)^1 \cdot e^{1700/T_g}$	[29]

Table A.2: ER- and LH-reaction constants. The sticking coefficient for metal  $s_{metal}$  and Al<sub>2</sub>O<sub>3</sub>  $s_{Al_2O_3}$ , surface diffusion energy barriers  $E_{diff}$  and activation barriers  $E_{act}$  in eV from table 5 in [32] and sticking coefficient for SiO<sub>2</sub> from [187].

#	ER-reaction	$s_{metal}$	$s_{Al_2O_3}$	$s_{SiO_2}$
S1	$N + S_f \longrightarrow N_s$	1	0.1	
S2	$H + S_f \longrightarrow H_s$	1	0.01	
S3	$NH + S_f \longrightarrow NH_s$	1	0.01	
S4	$NH_2 + S_f \longrightarrow NH_{2s}$	1	0.01	
S5	$N + N_s \longrightarrow N_2 + S_f$	$6e - 3$	$6 \cdot 10^{-5}$	$2 \cdot 10^{-4}$
S6	$H + H_s \longrightarrow H_2 + S_f$	0.005	$1.5 \cdot 10^{-6}$	$3 \cdot 10^{-5}$
S7	$N + H_s \longrightarrow NH_s$	0.01	0.001	
S8	$NH + H_s \longrightarrow NH_{2s}$	0.01	0.001	
S9	$NH_2 + H_s \longrightarrow NH_3 + S_f$	0.01	0.001	
S10	$H + N_s \longrightarrow NH_s$	$8 \cdot 10^{-3}$	$8 \cdot 10^{-4}$	
S11	$H + NH_s \longrightarrow NH_{2s}$	$8 \cdot 10^{-3}$	$8 \cdot 10^{-4}$	
S12	$H + NH_{2s} \longrightarrow NH_3 + S_f$	$8 \cdot 10^{-3}$	$8 \cdot 10^{-4}$	
S13	$H_2 + NH_s \longrightarrow NH_3 + S_f$	$8 \cdot 10^{-5}$	$8 \cdot 10^{-5}$	
S17	$N_2 + 2 S_f \longrightarrow 2 N_s$	$\gamma_{N_2}$	$10^{-3} \gamma_{N_2}$	
S18	$H_2 + 2 S_f \longrightarrow 2 H_s$	$10^{-3}$	$10^{-5}$	
#	LH-reaction	$E_{act}$	$E_{diff,metal}$	$E_{diff,dielectric}$
S14	$N_s + H_s \longrightarrow NH_s + S_f$	1.099	0.2	0.5
S15	$NH_s + H_s \longrightarrow NH_{2s} + S_f$	0.3	0.2	0.5
S16	$NH_{2s} + H_s \longrightarrow NH_3 + 2 S_f$	0.2	0.2	0.5

# Bibliography

- [1] H. Nazir, C. Louis, S. Jose, et al., “Is the H<sub>2</sub> economy realizable in the foreseeable future? Part I: H<sub>2</sub> production methods”, *International Journal of Hydrogen Energy* **45**, 13777–13788 (2020).
- [2] M. M. Hossain Bhuiyan and Z. Siddique, “Hydrogen as an alternative fuel: A comprehensive review of challenges and opportunities in production, storage, and transportation”, *International Journal of Hydrogen Energy* **102**, 1026–1044 (2025).
- [3] A. Pineau, N. Kanari, and I. Gaballah, “Kinetics of reduction of iron oxides by H<sub>2</sub>”, *Thermochimica Acta* **447**, 89–100 (2006).
- [4] S. Ristig, M. Poschmann, J. Folke, et al., “Ammonia Decomposition in the Process Chain for a Renewable Hydrogen Supply”, *Chemie Ingenieur Technik* **94**, 1413–1425 (2022).
- [5] R. Dunn, K. Lovegrove, and G. Burgess, “A Review of Ammonia-Based Thermochemical Energy Storage for Concentrating Solar Power”, *Proceedings of the IEEE* **100**, 391–400 (2012).
- [6] M. Akiyama, K. Aihara, T. Sawaguchi, et al., “Ammonia decomposition to clean hydrogen using non-thermal atmospheric-pressure plasma”, *International Journal of Hydrogen Energy* **43**, 14493–14497 (2018).
- [7] A. Afif, N. Radenahmad, Q. Cheok, et al., “Ammonia-fed fuel cells: a comprehensive review”, *Renewable and Sustainable Energy Reviews* **60**, 822–835 (2016).
- [8] K. H. R. Rouwenhorst, P. M. Krzywda, N. E. Benes, et al., “Chapter 4 - Ammonia Production Technologies”, in *Techno-Economic Challenges of Green Ammonia as an Energy Vector*, edited by A. Valera-Medina and R. Banares-Alcantara (Academic Press, Jan. 2021), pp. 41–83.
- [9] Z. Kirova-Yordanova, “Exergy-based estimation and comparison of urea and ammonium nitrate production efficiency and environmental impact”, *Energy* **140**, 158–169 (2017).
- [10] M. Reda Galih Pangestu and U. Zahid, “Techno-economic analysis of integrating methane pyrolysis and reforming technology for low-carbon ammonia”, *Energy Conversion and Management* **322**, 119125 (2024).
- [11] S. Shiva Kumar and H. Lim, “An overview of water electrolysis technologies for green hydrogen production”, *Energy Reports* **8**, 13793–13813 (2022).

- [12] B. A. Spoor, *We don't need the fossil industry for a fossil-free future*, Section: News, Mar. 2024.
- [13] S. Jenke, *Österreich: Eröffnung erster Anlage zur Methan-Elektrolyse*, Oct. 2023.
- [14] J. Hanke, *Turquoise Hydrogen via Methane Plasmalysis*, seminar, Geleen, the Netherlands, Oct. 2025.
- [15] R. K. Sharma, H. Patel, U. Mushtaq, et al., “Plasma Activated Electrochemical Ammonia Synthesis from Nitrogen and Water”, *ACS Energy Letters* **6**, 313–319 (2021).
- [16] K. H. R. Rouwenhorst, F. Jardali, A. Bogaerts, et al., “From the Birkeland–Eyde process towards energy-efficient plasma-based  $\text{NO}_x$  synthesis: a techno-economic analysis”, *Energy & Environmental Science* **14**, 2520–2534 (2021).
- [17] M. Gromov, Y. Gorbanev, E. Vervloessem, et al., “Electrification of fertilizer production via plasma-based nitrogen fixation: a tutorial on fundamentals”, *RSC Sustainability* **3**, 757–780 (2025).
- [18] A. Bogaerts and E. C. Neyts, “Plasma Technology: An Emerging Technology for Energy Storage”, *ACS Energy Letters* **3**, Publisher: American Chemical Society, 1013–1027 (2018).
- [19] Y. Gorbanev, Y. Engelmann, K. van't Veer, et al., “ $\text{Al}_2\text{O}_3$ -Supported Transition Metals for Plasma-Catalytic  $\text{NH}_3$  Synthesis in a DBD Plasma: Metal Activity and Insights into Mechanisms”, *Catalysts* **11**, 1230 (2021).
- [20] R. Brandenburg, “Dielectric barrier discharges: progress on plasma sources and on the understanding of regimes and single filaments”, *Plasma Sources Science and Technology* **26**, Publisher: IOP Publishing, 053001 (2017).
- [21] T. Mizushima, K. Matsumoto, H. Ohkita, et al., “Catalytic Effects of Metal-loaded Membrane-like Alumina Tubes on Ammonia Synthesis in Atmospheric Pressure Plasma by Dielectric Barrier Discharge”, *Plasma Chemistry and Plasma Processing* **27**, 1–11 (2007).
- [22] K. H. R. Rouwenhorst and L. Lefferts, “Plasma-catalytic Ammonia Synthesis via Eley-Rideal Reactions: A Kinetic Analysis”, *ChemCatChem* **15**, e202300078 (2023).
- [23] R. De Meyer, Y. Gorbanev, R.-G. Ciocarlan, et al., “Importance of plasma discharge characteristics in plasma catalysis: Dry reforming of methane vs. ammonia synthesis”, *Chemical Engineering Journal* **488**, 150838 (2024).
- [24] P. Mehta, P. Barboun, F. A. Herrera, et al., “Overcoming ammonia synthesis scaling relations with plasma-enabled catalysis”, *Nature Catalysis* **1**, Number: 4 Publisher: Nature Publishing Group, 269–275 (2018).
- [25] C. Ndayirinde, Y. Gorbanev, R.-G. Ciocarlan, et al., “Plasma-catalytic ammonia synthesis: Packed catalysts act as plasma modifiers”, *Catalysis Today* **419**, 114156 (2023).
- [26] M. Šimek, “Optical diagnostics of streamer discharges in atmospheric gases”, *Journal of Physics D: Applied Physics* **47**, 463001 (2014).

- [27] P. Bílek, M. Šimek, and Z. Bonaventura, “Electric field determination from intensity ratio of  $N_2^+$  and  $N_2$  bands: nonequilibrium transient discharges in pure nitrogen”, *Plasma Sources Science and Technology* **28**, 115011 (2019).
- [28] P. Bílek, L. Kuthanová, T. Hoder, et al., “Atmospheric pressure Townsend discharge in pure nitrogen—a test case for  $N_2(a^3\Sigma_u^+, v)$  kinetics under low E/N conditions”, *Plasma Sources Science and Technology* **31**, 084004 (2022).
- [29] B. Gordiets, C. M. Ferreira, M. J. Pinheiro, et al., “Self-consistent kinetic model of low-pressure - flowing discharges: I. Volume processes”, *Plasma Sources Science and Technology* **7**, 363 (1998).
- [30] B. Gordiets, C. M. Ferreira, M. J. Pinheiro, et al., “Self-consistent kinetic model of low-pressure - flowing discharges: II. Surface processes and densities of N, H, species”, *Plasma Sources Science and Technology* **7**, 379–388 (1998).
- [31] E. Carrasco, M. Jiménez-Redondo, I. Tanarro, et al., “Neutral and ion chemistry in low pressure dc plasmas of  $H_2/N_2$  mixtures: routes for the efficient production of  $NH_3$  and  $NH_4^+$ ”, *Physical Chemistry Chemical Physics* **13**, Publisher: The Royal Society of Chemistry, 19561–19572 (2011).
- [32] J. Hong, S. Pancheshnyi, E. Tam, et al., “Kinetic modelling of  $NH_3$  production in  $N_2-H_2$  non-equilibrium atmospheric-pressure plasma catalysis”, *Journal of Physics D: Applied Physics* **50**, 154005 (2017).
- [33] T. Silva, S. Bera, C. D. Pintassilgo, et al., “Unraveling NO Production in  $N_2-O_2$  Plasmas with 0D Kinetic Modeling and Experimental Validation”, *The Journal of Physical Chemistry A* **128**, 7235–7256 (2024).
- [34] Y. Engelmann, K. Van 'T Veer, Y. Gorbaney, et al., “Plasma Catalysis for Ammonia Synthesis: A Microkinetic Modeling Study on the Contributions of Eley–Rideal Reactions”, *ACS Sustainable Chemistry & Engineering* **9**, 13151–13163 (2021).
- [35] L. Lefferts, “Leveraging Expertise in Thermal Catalysis to Understand Plasma Catalysis”, *Angewandte Chemie International Edition* **63**, e202305322 (2024).
- [36] M. F. J. Vos, G. van Straaten, W. M. M. E. Kessels, et al., “Atomic Layer Deposition of Cobalt Using  $H_2$ -,  $N_2$ -, and  $NH_3$ -Based Plasmas: On the Role of the Co-reactant”, *The Journal of Physical Chemistry C* **122**, Publisher: American Chemical Society, 22519–22529 (2018).
- [37] F. M. Hoffmann, “Infrared reflection-absorption spectroscopy of adsorbed molecules”, *Surface Science Reports* **3**, 107–192 (1983).
- [38] G. Grundmeier, A. von Keudell, and T. de los Arcos, “Fundamentals and Applications of Reflection FTIR Spectroscopy for the Analysis of Plasma Processes at Materials Interfaces”, *Plasma Processes and Polymers* **12**, 926–940 (2015).
- [39] L. J. Lobree, I. Hwang, J. A. Reimer, et al., “An in situ infrared study of NO reduction by  $C_3H_8$  over Fe-ZSM-5”, *Catalysis Letters* **63**, 233–240 (1999).
- [40] K. Hadjiivanov, H. Knözinger, B. Tsyntsarski, et al., “Effect of water on the reduction of  $NO_x$  with propane on Fe-ZSM-5. An FTIR mechanistic study”, *Catalysis Letters* **62**, 35–40 (1999).

- [41] K. I. Hadjiivanov, “Identification of Neutral and Charged  $N_xO_y$  Surface Species by IR Spectroscopy”, *Catalysis Reviews* **42**, 71–144 (2000).
- [42] I. Malpartida, E. Ivanova, M. Mihaylov, et al., “CO and NO adsorption for the IR characterization of  $Fe^{2+}$  cations in ferrierite: An efficient catalyst for NO<sub>x</sub> SCR with NH<sub>3</sub> as studied by *operando* IR spectroscopy”, *Catalysis Today, Catalysis of the XXI Century: Towards a Sustainable Chemistry - XXI Ibero-American Symposium of Catalysis, Málaga-Benalmádena, Spain, 2008* **149**, 295–303 (2010).
- [43] S. Mosallanejad, B. Z. Dlugogorski, E. M. Kennedy, et al., “On the Chemistry of Iron Oxide Supported on gamma-Alumina and Silica Catalysts”, *ACS Omega* **3**, Publisher: American Chemical Society, 5362–5374 (2018).
- [44] M. A. Lieberman and A. J. Lichtenberg, *Principles of Plasma Discharges and Materials Processing*, 2nd (Hoboken : Wiley-Interscience, 2005).
- [45] S. C. Brown, “High-Frequency Gas-Discharge Breakdown”, *Proceedings of the IRE* **39**, 1493–1501 (1951).
- [46] A von Keudell and V Schulz-von der Gathen, “Foundations of low-temperature plasma physics—an introduction”, *Plasma Sources Science and Technology* **26**, 113001 (2017).
- [47] J. Park, I. Henins, H. W. Herrmann, et al., “Gas breakdown in an atmospheric pressure radio-frequency capacitive plasma source”, *Journal of Applied Physics* **89**, 15–19 (2001).
- [48] R. Buschhaus and A. von Keudell, “Secondary electron emission from magnetron targets”, *Plasma Sources Science and Technology* **32**, Publisher: IOP Publishing, 065007 (2023).
- [49] Y. Harada, S. Masuda, and H. Ozaki, “Electron Spectroscopy Using Metastable Atoms as Probes for Solid Surfaces”, *Chemical Reviews* **97**, 1897–1952 (1997).
- [50] W. J. M. Brok, M. D. Bowden, J. van Dijk, et al., “Numerical description of discharge characteristics of the plasma needle”, *Journal of Applied Physics* **98**, 013302 (2005).
- [51] C. Corbella, A. Marcak, T. d. l. Arcos, et al., “Revising secondary electron yields of ion-sputtered metal oxides”, *Journal of Physics D: Applied Physics* **49**, Publisher: IOP Publishing, 16LT01 (2016).
- [52] R. Buschhaus, M. Prenzel, and A. von Keudell, “Ion-induced secondary electron emission of oxidized nickel and copper studied in beam experiments”, *Plasma Sources Science and Technology* **31**, 025017 (2022).
- [53] C. Li, F. Greiner, X. Chen, et al., “Progress in reactions, momentum transfer, and energy transfer processes for nanoparticles in processing non-thermal plasmas”, *Physics Reports* **1135**, 1–73 (2025).
- [54] L. L. Alves, “The IST-LISBON database on LXCat”, *Journal of Physics: Conference Series* **565**, 012007 (2014).
- [55] *Morgan LXCat database*, [www.lxcat.net/Morgan](http://www.lxcat.net/Morgan), June 2023.

- [56] *Hayashi LXCat database*, [www.lxcat.net/Hayashi](http://www.lxcat.net/Hayashi), Feb. 2024.
- [57] A Tejero-del Caz, V Guerra, D Gonçalves, et al., “The LisbOn KInetics Boltzmann solver”, *Plasma Sources Science and Technology* **28**, 043001 (2019).
- [58] A Tejero-del Caz, V Guerra, N Pinhão, et al., “On the quasi-stationary approach to solve the electron Boltzmann equation in pulsed plasmas”, *Plasma Sources Science and Technology* **30**, 065008 (2021).
- [59] J. Golda, J. Held, B. Redeker, et al., “Concepts and characteristics of the ‘COST Reference Microplasma Jet’”, *Journal of Physics D: Applied Physics* **49**, 084003 (2016).
- [60] J. Golda, J. Held, and V. S.-v. d. Gathen, “Comparison of electron heating and energy loss mechanisms in an RF plasma jet operated in argon and helium”, *Plasma Sources Science and Technology* **29**, Publisher: IOP Publishing, 025014 (2020).
- [61] T. Martens, A. Bogaerts, W. J. M. Brok, et al., “The dominant role of impurities in the composition of high pressure noble gas plasmas”, *Applied Physics Letters* **92**, 041504 (2008).
- [62] W. Grünert, W. Kleist, and M. Muhler, *Catalysis at Surfaces* (De Gruyter, July 2023).
- [63] A. Hurlbatt, A. R. Gibson, S. Schröter, et al., “Concepts, Capabilities, and Limitations of Global Models: A Review”, *Plasma Processes and Polymers* **14**, 1600138 (2017).
- [64] Y. He, P. Preissing, D. Steuer, et al., “Zero-dimensional and pseudo-one-dimensional models of atmospheric-pressure plasma jets in binary and ternary mixtures of oxygen and nitrogen with helium background”, *Plasma Sources Science and Technology* **30**, Publisher: IOP Publishing, 105017 (2021).
- [65] E. Hairer and G. Wanner, “Stiff differential equations solved by Runge-Kutta methods”, *Journal of Computational and Applied Mathematics* **111**, 93–111 (1999).
- [66] M. Vass, D. Schulenberg, Z. Donkó, et al., “Energy efficiency of reactive species generation in radio frequency atmospheric pressure plasma jets driven by tailored voltage waveforms in a He/O<sub>2</sub> mixture”, *Plasma Sources Science and Technology* **33**, Publisher: IOP Publishing, 11LT01 (2024).
- [67] M Klich, D Schulenberg, S Wilczek, et al., “Electron dynamics of three distinct discharge modes of a cross-field atmospheric pressure plasma jet”, *Plasma Sources Science and Technology* **34**, 045012 (2025).
- [68] I Orel, N. D. Lepikhin, D Luggenhölscher, et al., “Electric field measurements in a He:N<sub>2</sub> atmospheric pressure RF plasma jet by E-FISH”, *Plasma Sources Science and Technology* **34**, 015016 (2025).
- [69] P. R. Griffiths and J. A. d. Haseth, *Fourier Transform Infrared Spectrometry*, 2nd (John Wiley & Sons, Inc, Hoboken, New Jersey, 2007).
- [70] W. Demtröder, *Laser Spectroscopy 1*, 5th ed. (Springer Berlin, Heidelberg, Heidelberg, 2014).

- [71] C. R. Anderson and D. R. Mattson, “Phase Correction Techniques In Fourier Transform-Infrared (FT-IR)”, in *Multiplex and/or High Throughput Spectroscopy*, Vol. 0191 (Oct. 1979), pp. 101–109.
- [72] A. Nuttall, “Some windows with very good sidelobe behavior”, *IEEE Transactions on Acoustics, Speech, and Signal Processing* **29**, Conference Name: IEEE Transactions on Acoustics, Speech, and Signal Processing, 84–91 (1981).
- [73] N. M. Davies, W. Bell, A. Vance, et al., “Measurement of Fourier transform infrared spectrometer instrument lineshape”, in *Spectroscopic Atmospheric Environmental Monitoring Techniques*, Vol. 3493 (Dec. 1998), pp. 79–87.
- [74] K. Rahmelow and W. Hübner, “Phase correction in Fourier transform spectroscopy: subsequent displacement correction and error limit”, *Applied Optics* **36**, 6678–6686 (1997).
- [75] A. Keens and A. Simon, “Correction of non-linearities in detectors in fourier transform spectroscopy”, pat. US4927269A (May 1990).
- [76] M. C. Abrams, G. C. Toon, and R. A. Schindler, “Practical example of the correction of Fourier-transform spectra for detector nonlinearity”, *Applied Optics* **33**, 6307–6314 (1994).
- [77] L. S. Rothman, R. R. Gamache, A. Goldman, et al., “The HITRAN database: 1986 edition”, *Applied Optics* **26**, 4058–4097 (1987).
- [78] I. E. Gordon, L. S. Rothman, R. J. Hargreaves, et al., “The HITRAN2020 molecular spectroscopic database”, *Journal of Quantitative Spectroscopy and Radiative Transfer* **277**, 107949 (2022).
- [79] B. L. M. Klarenaar, R. Engeln, D. C. M. v. d. Bekerom, et al., “Time evolution of vibrational temperatures in a CO<sub>2</sub> glow discharge measured with infrared absorption spectroscopy”, *Plasma Sources Science and Technology* **26**, 115008 (2017).
- [80] M. A. Damen, L. M. Martini, and R. Engeln, “Temperature evolution in a pulsed CO<sub>2</sub> – N<sub>2</sub> glow discharge measured using quantum cascade laser absorption spectroscopy”, *Plasma Sources Science and Technology* **29**, 065016 (2020).
- [81] Y. Du, T. V. Tsankov, D. Luggenhölscher, et al., “Nanosecond resolved rovibrational CO<sub>2</sub> excitation measurement”, *Journal of Physics D: Applied Physics* **54**, 34LT02 (2021).
- [82] W. Demtröder, *Laser Spectroscopy 2*, 5th ed. (Springer Berlin, Heidelberg, Heidelberg, 2015).
- [83] M. Grofulović, B. L. M. Klarenaar, O. Guaitella, et al., “A rotational Raman study under non-thermal conditions in pulsed CO<sub>2</sub>-N<sub>2</sub> and CO<sub>2</sub>-O<sub>2</sub> glow discharges”, *Plasma Sources Science and Technology* **28**, 045014 (2019).
- [84] B. L. M. Klarenaar, M. Grofulović, A. S. Morillo-Candas, et al., “A rotational Raman study under non-thermal conditions in a pulsed CO<sub>2</sub> glow discharge”, *Plasma Sources Science and Technology* **27**, 045009 (2018).

- [85] S. C. L. Vervloedt, M. Budde, and R. Engeln, “Influence of oxygen on the rovibrational kinetics of a non-equilibrium discharge in CO<sub>2</sub>–O<sub>2</sub> mixtures”, *Plasma Sources Science and Technology* **32**, 015004 (2023).
- [86] D. Steuer, B. Z. Bentz, K. Youngman, et al., “Measurement of atomic oxygen densities using TALIF on a dielectric barrier discharge: insights into the volume above a micro cavity plasma array”, *Plasma Sources Science and Technology* **33**, Publisher: IOP Publishing, 125007 (2024).
- [87] M. Budde, L. M. Martini, M. Ceppelli, et al., “Absolute OH density measurements in a CO<sub>2</sub>–H<sub>2</sub>O glow discharge by laser-induced fluorescence spectroscopy”, *Plasma Sources Science and Technology* **31**, 055002 (2022).
- [88] J. R. Wubs, L. Invernizzi, K. Gazeli, et al., “Validation of THz absorption spectroscopy by a comparison with ps-TALIF measurements of atomic oxygen densities”, *Applied Physics Letters* **123**, 081107 (2023).
- [89] I. Sadiq, A. Puth, G. Kowzan, et al., “Precision spectroscopy of non-thermal molecular plasmas using mid-infrared optical frequency comb Fourier transform spectroscopy”, *Plasma Sources Science and Technology* **33**, 075011 (2024).
- [90] S. Yu, S. C. L. Vervloedt, and A. von Keudell, “Controlled synthesis of NO in an atmospheric pressure plasma by suppressing NO destruction channels by plasma catalysis”, *Journal of Physics D: Applied Physics* **57**, Publisher: IOP Publishing, 245203 (2024).
- [91] S. C. L. Vervloedt and A. von Keudell, “Ammonia synthesis by plasma catalysis in an atmospheric RF helium plasma”, *Plasma Sources Science and Technology* **33**, Publisher: IOP Publishing, 045005 (2024).
- [92] C. Stewig, S. Schüttler, T. Urbanietz, et al., “Excitation and dissociation of CO<sub>2</sub> heavily diluted in noble gas atmospheric pressure plasma”, *Journal of Physics D: Applied Physics* **53**, 125205 (2020).
- [93] W. N. Hansen, “Electric Fields Produced by the Propagation of Plane Coherent Electromagnetic Radiation in a Stratified Medium”, *JOSA* **58**, 380–390 (1968).
- [94] J. D. E. McIntyre and D. E. Aspnes, “Differential reflection spectroscopy of very thin surface films”, *Surface Science* **24**, 417–434 (1971).
- [95] D. J. Griffiths, *Introduction to Electrodynamics*, 4th (Cambridge University Press, Cambridge, 2017).
- [96] J. Smidt, “High frequency permeability”, *Applied Scientific Research, Section B* **1**, 127–134 (1950).
- [97] M. N. Polyanskiy, “Refractiveindex.info database of optical constants”, *Scientific Data* **11**, Publisher: Nature Publishing Group, 94 (2024).
- [98] P. Hollins, “Infrared Reflection–Absorption Spectroscopy”, in *Encyclopedia of Analytical Chemistry* (John Wiley & Sons, Ltd, 2006).
- [99] J. Šebera, J. Zemen, V. Jirásek, et al., “FTIR Measurement of the Hydrogenated Si(100) Surface: The Structure-Vibrational Interpretation by Means of Periodic DFT Calculation”, *The Journal of Physical Chemistry C* **125**, Publisher: American Chemical Society, 9219–9228 (2021).

- [100] R. J. Lippert, B. D. Lamp, and M. D. Porter, “Specular reflection spectroscopy”, in *Modern Techniques in Applied Molecular Spectroscopy* (John Wiley & Sons, Inc, 1998), pp. 83–126.
- [101] C. Smit, R. A. C. M. M. van Swaaij, H. Donker, et al., “Determining the material structure of microcrystalline silicon from Raman spectra”, *Journal of Applied Physics* **94**, 3582–3588 (2003).
- [102] S. Schlücker, “Surface-Enhanced Raman Spectroscopy: Concepts and Chemical Applications”, *Angewandte Chemie International Edition* **53**, 4756–4795 (2014).
- [103] N. V. Richardson, “High resolution electron energy loss spectroscopy”, *Current Opinion in Solid State and Materials Science* **2**, 517–524 (1997).
- [104] W. Erley and H. Ibach, “Vibrational spectra of ammonia adsorbed on Fe(110)”, *Surface Science* **119**, L357–L362 (1982).
- [105] Y. Wang and K. Jacobi, “Vibrational characterization of NH and NH<sub>2</sub> reaction intermediates on the Ru(110) surface”, *Surface Science* **513**, 83–92 (2002).
- [106] S. Yamamoto, T. Kendelewicz, J. T. Newberg, et al., “Water Adsorption on  $\alpha$ -Fe<sub>2</sub>O<sub>3</sub>(0001) at near Ambient Conditions”, *The Journal of Physical Chemistry C* **114**, Publisher: American Chemical Society, 2256–2266 (2010).
- [107] I. Zawisza, G. Wittstock, R. Boukherroub, et al., “PM IRRAS Investigation of Thin Silica Films Deposited on Gold. Part 1. Theory and Proof of Concept”, *Langmuir* **23**, Publisher: American Chemical Society, 9303–9309 (2007).
- [108] D. M. Meier, A. Urakawa, R. Mäder, et al., “Design and performance of a flow-through polarization-modulation infrared reflection-absorption spectroscopy cell for time-resolved simultaneous surface and liquid phase detection under concentration and temperature perturbations”, *Review of Scientific Instruments* **80**, 094101 (2009).
- [109] C. de Alwis, T. R. Leftwich, and K. A. Perrine, “New Approach to Simultaneous In Situ Measurements of the Air/Liquid/Solid Interface Using PM-IRRAS”, *Langmuir* **36**, 3404–3414 (2020).
- [110] D. L. Crintea, U. Czarnetzki, S. Iordanova, et al., “Plasma diagnostics by optical emission spectroscopy on argon and comparison with Thomson scattering”, *Journal of Physics D: Applied Physics* **42**, 045208 (2009).
- [111] D. Steuer, H. van Impel, V. Schulz-von der Gathen, et al., “Spatially and temporally resolved atomic oxygen densities in a micro cavity plasma array”, *Plasma Sources Science and Technology* **32**, 025013 (2023).
- [112] C. Biloiu, X. Sun, Z. Harvey, et al., “An alternative method for gas temperature determination in nitrogen plasmas: Fits of the bands of the first positive system ( $B^3\Pi_g \rightarrow A^3\Sigma_u^+$ )”, *Journal of Applied Physics* **101**, 073303 (2007).
- [113] F. R. Gilmore, R. R. Laher, and P. J. Espy, “Franck–Condon Factors, r-Centroids, Electronic Transition Moments, and Einstein Coefficients for Many Nitrogen and Oxygen Band Systems”, *Journal of Physical and Chemical Reference Data* **21**, Publisher: American Institute of Physics, 1005–1107 (1992).

- [114] P. J. Bruggeman, N. Sadeghi, D. C. Schram, et al., “Gas temperature determination from rotational lines in non-equilibrium plasmas: a review”, *Plasma Sources Science and Technology* **23**, 023001 (2014).
- [115] M. Ceppelli, T. P. W. Salden, L. M. Martini, et al., “Time-resolved optical emission spectroscopy in CO<sub>2</sub> nanosecond pulsed discharges”, *Plasma Sources Science and Technology* **30**, 115010 (2021).
- [116] T. Urbanietz, C. Stewig, M. Böke, et al., “Oxygen Removal from a Hydrocarbon Containing Gas Stream by Plasma Catalysis”, *Plasma Chemistry and Plasma Processing* **41**, 619–642 (2021).
- [117] C. Stewig, T. Urbanietz, L. Chauvet, et al., “Dedicated setup to isolate plasma catalysis mechanisms”, *Journal of Physics D: Applied Physics* **54**, 134005 (2021).
- [118] C. Stewig, L. Chauvet, and A. von Keudell, “Impact of catalysis on n-butane oxidation in an RF atmospheric pressure plasma”, *Plasma Sources Science and Technology* **32**, 105006 (2023).
- [119] N. Peters, L. Schücke, K. Ollegott, et al., “Catalyst-enhanced plasma oxidation of n-butane over  $\alpha$ -MnO<sub>2</sub> in a temperature-controlled twin surface dielectric barrier discharge reactor”, *Plasma Processes and Polymers* **18**, 2000127 (2021).
- [120] T. Vidaković, M. Christov, and K. Sundmacher, “A method for rough estimation of the catalyst surface area in a fuel cell”, *Journal of Applied Electrochemistry* **39**, 213–225 (2009).
- [121] J. Golda, F. Kogelheide, P. Awakowicz, et al., “Dissipated electrical power and electron density in an RF atmospheric pressure helium plasma jet”, *Plasma Sources Science and Technology* **28**, 095023 (2019).
- [122] M. J. Down, C. Hill, S. N. Yurchenko, et al., “Re-analysis of ammonia spectra: Updating the HITRAN <sup>14</sup>NH<sub>3</sub> database”, *Journal of Quantitative Spectroscopy and Radiative Transfer*, HITRAN2012 special issue **130**, 260–272 (2013).
- [123] A. Fried and D. Richter, “Infrared Absorption Spectroscopy”, in *Analytical Techniques for Atmospheric Measurement* (John Wiley & Sons, Ltd, Apr. 2006), pp. 72–146.
- [124] E. Sälli, S. Martiskainen, and L. Halonen, “Computational Study of the Vibrational Structure of the Ammonia Molecule Adsorbed on the fcc (111) Transition Metal Surfaces”, *The Journal of Physical Chemistry C* **116**, 14960–14969 (2012).
- [125] I. N. Kadochnikov, B. I. Loukhovitski, and A. M. Starik, “Kinetics of plasma-chemical processes in the expanding flow of nitrogen plasma”, *Physica Scripta* **88**, Publisher: IOP Publishing, 058306 (2013).
- [126] X.-L. Wang, Y. Liu, and Y.-T. Zhang, “On  $\Omega$  Mode in Radio-Frequency Atmospheric Discharges Controlled by Dielectric Barriers”, *IEEE Transactions on Plasma Science* **45**, 3147–3153 (2017).
- [127] F. R. Gilmore, “Potential energy curves for N<sub>2</sub>, NO, O<sub>2</sub> and corresponding ions”, *Journal of Quantitative Spectroscopy and Radiative Transfer* **5**, 369–IN3 (1965).

- [128] S. De Benedictis and G. Dilecce, “Relaxation of excited species in He/N<sub>2</sub> pulsed RF discharges: kinetics of metastable species”, *Plasma Sources Science and Technology* **4**, 212 (1995).
- [129] L. Bischoff, G. Hübner, I. Korolov, et al., “Experimental and computational investigations of electron dynamics in micro atmospheric pressure radio-frequency plasma jets operated in He/N<sub>2</sub> mixtures”, *Plasma Sources Science and Technology* **27**, Publisher: IOP Publishing, 125009 (2018).
- [130] D. Reiser, A. von Keudell, and T. Urbanietz, “Determining Chemical Reaction Systems in Plasma-Assisted Conversion of Methane Using Genetic Algorithms”, *Plasma Chemistry and Plasma Processing* **41**, 793–813 (2021).
- [131] S. V. Pancheshnyi, S. M. Starikovskaia, and A. Y. Starikovskii, “Collisional deactivation of N<sub>2</sub>(C<sup>3</sup>Π<sub>u</sub>, *v*=0, 1, 2, 3) states by N<sub>2</sub>, O<sub>2</sub>, H<sub>2</sub> and H<sub>2</sub>O molecules”, *Chemical Physics* **262**, 349–357 (2000).
- [132] I. Korolov, M. Leimkühler, M. Böke, et al., “Helium metastable species generation in atmospheric pressure RF plasma jets driven by tailored voltage waveforms in mixtures of He and N<sub>2</sub>”, *Journal of Physics D: Applied Physics* **53**, Publisher: IOP Publishing, 185201 (2020).
- [133] S. Picaud, A. Lakhlifi, and C. Girardet, “NH<sub>3</sub> physisorption on MgO(100) substrate. Potential calculations revisited”, *The Journal of Chemical Physics* **98**, 3488–3495 (1993).
- [134] S. F. Yin, B. Q. Xu, X. P. Zhou, et al., “A mini-review on ammonia decomposition catalysts for on-site generation of hydrogen for fuel cell applications”, *Applied Catalysis A: General* **277**, 1–9 (2004).
- [135] A. Gómez-Ramírez, J. Cotrino, R. M. Lambert, et al., “Efficient synthesis of ammonia from N<sub>2</sub> and H<sub>2</sub> alone in a ferroelectric packed-bed DBD reactor”, *Plasma Sources Science and Technology* **24**, Publisher: IOP Publishing, 065011 (2015).
- [136] S. Li, T. v. Raak, and F. Gallucci, “Investigating the operation parameters for ammonia synthesis in dielectric barrier discharge reactors”, *Journal of Physics D: Applied Physics* **53**, Publisher: IOP Publishing, 014008 (2019).
- [137] F. Gorky, M. A. Carreon, and M. L. Carreon, “Experimental strategies to increase ammonia yield in plasma catalysis over LTA and BEA zeolites”, *IOP SciNotes* **1**, 024801 (2020).
- [138] K. van ‘t Veer, F. Reniers, and A. Bogaerts, “Zero-dimensional modeling of unpacked and packed bed dielectric barrier discharges: the role of vibrational kinetics in ammonia synthesis”, *Plasma Sources Science and Technology* **29**, 045020 (2020).
- [139] V Guerra, E Galiaskarov, and J Loureiro, “Dissociation mechanisms in nitrogen discharges”, *Chemical Physics Letters* **371**, 576–581 (2003).
- [140] G. Dilecce, P. F. Ambrico, and S. De Benedictis, “OODR-LIF direct measurement of N<sub>2</sub>(C<sup>3</sup>Σ<sub>u</sub>, *v*=0–4) electronic quenching and vibrational relaxation rate coefficients by N<sub>2</sub> collision”, *Chemical Physics Letters* **431**, 241–246 (2006).

- [141] J Raud, M Laan, and I Jõgi, “Rotational temperatures of  $N_2(C,0)$  and  $OH(A,0)$  as gas temperature estimates in the middle pressure Ar/ $O_2$  discharge”, *Journal of Physics D: Applied Physics* **44**, 345201 (2011).
- [142] G. Dilecce, P. F. Ambrico, L. M. Martini, et al., “On the determination of the vibrational temperature by optical emission spectroscopy”, *Plasma Sources Science and Technology* **31**, 077001 (2022).
- [143] M. Ruiz-Martín, M. Oliva-Ramírez, A. R. González-Elipe, et al., “Plasma catalysis for gas conversion – Impact of catalyst on the plasma behavior”, *Current Opinion in Green and Sustainable Chemistry* **51**, 100990 (2025).
- [144] S. Vervloedt and A. von Keudell, “Nitrogen Oxidation on A Plasma-Exposed Surface”, *Plasma Chemistry and Plasma Processing* **45**, 1551–1565 (2025).
- [145] S. Samukawa, M. Hori, S. Rauf, et al., “The 2012 Plasma Roadmap”, *Journal of Physics D: Applied Physics* **45**, 253001 (2012).
- [146] T. D. Goldfarb and B. N. Khare, “Infrared Spectra of Solid and Matrix-Isolated  $(CH_3)_3N$ ,  $(CD_3)_3N$ , and  $(SiH_3)_3N$ ”, *The Journal of Chemical Physics* **46**, 3379–3384 (2004).
- [147] M. Cagnasso, V. Boero, M. A. Franchini, et al., “ATR-FTIR studies of phospholipid vesicle interactions with  $\alpha$ -FeOOH and  $\alpha$ -Fe $_2$ O $_3$  surfaces”, *Colloids and Surfaces B: Biointerfaces* **76**, 456–467 (2010).
- [148] L. Xu, D. Kirvassilis, Y. Bai, et al., “Atomic and molecular adsorption on Fe(110)”, *Surface Science* **667**, 54–65 (2018).
- [149] C. P. O’Brien and I. C. Lee, “A detailed spectroscopic analysis of the growth of oxy-carbon species on the surface of Pt/ $Al_2O_3$  during propane oxidation”, *Journal of Catalysis* **347**, 1–8 (2017).
- [150] G. Grundmeier and M. Stratmann, “Influence of oxygen and argon plasma treatments on the chemical structure and redox state of oxide covered iron”, *Applied Surface Science* **141**, 43–56 (1999).
- [151] S. Nasrazadani and A. Raman, “The application of infrared spectroscopy to the study of rust systems—II. Study of cation deficiency in magnetite  $Fe_3O_4$  produced during its transformation to maghemite ( $\gamma$ -Fe $_2$ O $_3$ ) and hematite ( $\alpha$ -Fe $_2$ O $_3$ )”, *Corrosion Science* **34**, 1355–1365 (1993).
- [152] G. W. Poling, “Infrared Reflection Studies of the Oxidation of Copper and Iron”, *Journal of The Electrochemical Society* **116**, Publisher: IOP Publishing, 958–963 (1969).
- [153] J. Raacke, M. Giza, and G. Grundmeier, “Combination of FTIR reflection absorption spectroscopy and work function measurement for in-situ studies of plasma modification of polymer and metal surfaces”, *Surface and Coatings Technology, PSE 2004* **200**, 280–283 (2005).
- [154] M. Mufti Azis, H. Härelind, and D. Creaser, “On the role of  $H_2$  to modify surface  $NO_x$  species over Ag- $Al_2O_3$  as lean  $NO_x$  reduction catalyst: TPD and DRIFTS studies”, *Catalysis Science & Technology* **5**, Publisher: Royal Society of Chemistry, 296–309 (2015).

- [155] K. Hadjiivanov, V. Bushev, M. Kantcheva, et al., “Infrared spectroscopy study of the species arising during nitrogen dioxide adsorption on titania (anatase)”, *Langmuir* **10**, Publisher: American Chemical Society, 464–471 (1994).
- [156] M. Iwasaki and H. Shinjoh, “Analysis of the adsorption state and desorption kinetics of NO<sub>2</sub> over Fe–zeolite catalyst by FT-IR and temperature-programmed desorption”, *Physical Chemistry Chemical Physics* **12**, Publisher: The Royal Society of Chemistry, 2365–2372 (2010).
- [157] N. Y. Acelas, C. Hadad, A. Restrepo, et al., “Adsorption of Nitrate and Bicarbonate on Fe-(Hydr)oxide”, *Inorganic Chemistry* **56**, 5455–5464 (2017).
- [158] G. Mul, J. Pérez-Ramírez, F. Kapteijn, et al., “NO Adsorption on Ex-Framework [Fe,X]MFI Catalysts: Novel IR Bands and Evaluation of Assignments”, *Catalysis Letters* **80**, 129–138 (2002).
- [159] K. Hadjiivanov and H. Knözinger, “Species formed after NO adsorption and NO+O<sub>2</sub> co-adsorption on TiO<sub>2</sub>: an FTIR spectroscopic study”, *Physical Chemistry Chemical Physics* **2**, 2803–2806 (2000).
- [160] J. Pérez-Ramírez, G. Mul, F. Kapteijn, et al., “Elucidation of the Surprising Role of NO in N<sub>2</sub>O Decomposition over FeZSM-5”, *Kinetics and Catalysis* **44**, 639–647 (2003).
- [161] H.-Y. Chen, T. Voskoboinikov, and W. M. H. Sachtler, “Reduction of NO<sub>x</sub> over Fe/ZSM-5 Catalysts: Adsorption Complexes and Their Reactivity toward Hydrocarbons”, *Journal of Catalysis* **180**, 171–183 (1998).
- [162] K.-i. Segawa, Y. Chen, J. E. Kubsh, et al., “Infrared and Mössbauer spectroscopic studies of the interaction of nitric oxide with Fe-Y zeolite”, *Journal of Catalysis* **76**, 112–132 (1982).
- [163] L. J. Lobree, I.-C. Hwang, J. A. Reimer, et al., “Investigations of the State of Fe in H-ZSM-5”, *Journal of Catalysis* **186**, 242–253 (1999).
- [164] G. Spoto, A. Zecchina, G. Berlier, et al., “FTIR and UV–Vis characterization of Fe-Silicalite”, *Journal of Molecular Catalysis A: Chemical* **158**, 107–114 (2000).
- [165] Z.-X. Gao, Q. Sun, and W. M. H. Sachtler, “Adsorption complexes of O<sub>2</sub> on Fe/MFI and their role in the catalytic reduction of NO<sub>x</sub>”, *Applied Catalysis B: Environmental* **33**, 9–23 (2001).
- [166] Q. Sun, Z.-X. Gao, B. Wen, et al., “Spectroscopic Evidence for a Nitrite Intermediate in the Catalytic Reduction of NO<sub>x</sub> with Ammonia on Fe/MFI”, *Catalysis Letters* **78**, 1–5 (2002).
- [167] J. Meichsner and K. Li, “In situ characterisation of thin-film formation in molecular low-temperature plasmas”, *Applied Physics A* **72**, 565–571 (2001).
- [168] G. Lee, C. Yan, W. F. Schneider, et al., “Observation and Characterization of Vibrationally Active Surface Species Accessed with Nonthermal Nitrogen Plasmas”, *ACS Applied Materials & Interfaces* **16**, Publisher: American Chemical Society, 4561–4569 (2024).

- [169] C. Morterra, C. Mirra, and E. Borello, "IR spectroscopic study of pyridine adsorption onto  $\alpha$ -FeOOH (goethite)", *Materials Chemistry and Physics* **10**, 139–154 (1984).
- [170] W. H. Hung, J. Schwartz, and S. L. Bernasek, "Adsorption of H<sub>2</sub>O on oxidized Fe(100) surfaces: comparison between the oxidation of iron by H<sub>2</sub>O and O<sub>2</sub>", *Surface Science* **294**, 21–32 (1993).
- [171] H. A. Al-Abadleh and V. H. Grassian, "FT-IR Study of Water Adsorption on Aluminum Oxide Surfaces", *Langmuir* **19**, 341–347 (2003).
- [172] A. M. Baró and W. Erley, "The adsorption of H<sub>2</sub>O on Fe(100) studied by EELS", *Journal of Vacuum Science and Technology* **20**, 580–583 (1982).
- [173] K. Jacobi, Y. Wang, C. Y. Fan, et al., "Adsorption and thermal dehydrogenation of ammonia on Ru(1121)", *The Journal of Chemical Physics* **115**, 4306–4313 (2001).
- [174] Y. Wang, A. Lafosse, and K. Jacobi, "Stepwise dehydrogenation of NH<sub>3</sub> at the Ru(1120) surface", *Surface Science* **507-510**, 773–777 (2002).
- [175] P. Dementyev, K.-H. Dostert, F. Ivars-Barceló, et al., "Water Interaction with Iron Oxides", *Angewandte Chemie* **127**, 14148–14152 (2015).
- [176] L. Wu, S. Tong, and M. Ge, "Heterogeneous Reaction of NO<sub>2</sub> on Al<sub>2</sub>O<sub>3</sub>: The Effect of Temperature on the Nitrite and Nitrate Formation", *The Journal of Physical Chemistry A* **117**, Publisher: American Chemical Society, 4937–4944 (2013).
- [177] L. Li, Q. shen, J. Cheng, et al., "Catalytic oxidation of NO over TiO<sub>2</sub> supported platinum clusters. II: Mechanism study by in situ FTIR spectra", *Catalysis Today, Perspective on catalysis for sustainable energy and environmental technologies* **158**, 361–369 (2010).
- [178] A. Heyden, N. Hansen, A. T. Bell, et al., "Nitrous Oxide Decomposition over Fe-ZSM-5 in the Presence of Nitric Oxide: A Comprehensive DFT Study", *The Journal of Physical Chemistry B* **110**, Publisher: American Chemical Society, 17096–17114 (2006).
- [179] P. Iyngaran, D. C. Madden, D. A. King, et al., "Infrared Spectroscopy of Ammonia on Iron: Thermal Stability and the Influence of Potassium", *The Journal of Physical Chemistry C* **118**, Publisher: American Chemical Society, 12184–12194 (2014).
- [180] P. Iyngaran, D. C. Madden, D. A. King, et al., "Infrared Spectroscopy of Ammonia on Iron: Adsorption, Synthesis, and the Influence of Oxygen", *The Journal of Physical Chemistry C* **121**, Publisher: American Chemical Society, 24594–24602 (2017).
- [181] B. J. Cha, J. Y. Choi, S. H. Kim, et al., "In Situ Spectroscopic Studies of NH<sub>3</sub> Oxidation of Fe-Oxide/Al<sub>2</sub>O<sub>3</sub>", *ACS Omega* **8**, Publisher: American Chemical Society, 18064–18073 (2023).
- [182] L. R. Winter, B. Ashford, J. Hong, et al., "Identifying Surface Reaction Intermediates in Plasma Catalytic Ammonia Synthesis", *ACS Catalysis* **10**, Publisher: American Chemical Society, 14763–14774 (2020).

- 
- [183] L. Hollevoet, F. Jardali, Y. Gorbanev, et al., “Towards Green Ammonia Synthesis through Plasma-Driven Nitrogen Oxidation and Catalytic Reduction”, *Angewandte Chemie International Edition* **59**, 23825–23829 (2020).
- [184] Y. Zhang, A. Tomita, R. Wakabayashi, et al., “Low-temperature synthesis of  $\text{NH}_3$  via an alternate gas-switching  $\text{NO}_x$  storage-reduction process using a  $\text{BaO/Pt (at)mTiO}_2$  nanocomposite catalyst”, *Journal of Materials Chemistry A* **12**, 8262–8271 (2024).
- [185] D. T. Stibbe and J. Tennyson, “Near-threshold electron impact dissociation of  $\text{H}_2$  within the adiabatic nuclei approximation”, *New Journal of Physics* **1**, 2 (1998).
- [186] R. A. Arakoni, A. N. Bhoj, and M. J. Kushner, “ $\text{H}_2$  generation in  $\text{Ar/NH}_3$  microdischarges”, *Journal of Physics D: Applied Physics* **40**, 2476 (2007).
- [187] Y. C. Kim and M. Boudart, “Recombination of oxygen, nitrogen, and hydrogen atoms on silica: kinetics and mechanism”, *Langmuir* **7**, Publisher: American Chemical Society, 2999–3005 (1991).

# Acknowledgements

The work behind this thesis started on the first of April 2022. At first, I was afraid that it was all a April Fool's joke. Luckily, it was not. I am genuinely grateful for having had the opportunity to attain my PhD at the Ruhr-University Bochum within the SFB1316 research collaborative. This collaborative is an ideal environment for a beginner scientist. You come into contact with other fields of expertise such as chemistry, electro-engineering, and biology. The tri-yearly meetings are a good staging ground to practice your presentation skills and to seek help from fellow PhD students, Postdocs, and PI's. I look back on a great time here in Bochum.

Zur allererst bedanke ich mich bei **Prof. Dr. Achim von Keudell** für die Möglichkeit, meine Dissertation in seine Arbeitsgruppe durchzuführen. His extensive knowledge on plasma physics cannot be missed. He is a prime example of a great scientist. He showed me that as a good scientist, you should always ask the next question and don't dwell too much on a single aspect. He helped me improving my skills for writing, presenting, and, most importantly, experimenting. In addition, he supported me with learning German by giving me the opportunity to follow several *Deutschsprache* courses at the *Bereich Deutsch als Fremdsprache* in Bochum. It was a great honor to have worked with you.

I would like to thank **Prof. Dr. Judith Golda** for agreeing to be my second supervisor. The casual and informative discussions were very much welcomed.

**Prof. Dr. Ir. Jean-Pierre H. van Helden**, I am grateful to you for agreeing to be my second reviewer. Dankjewel.

My work would not have been possible without the support from the chair. **Verena Benach**, thanks a lot for helping me with finding a place in the first months and the necessary administration to get employed and matriculated at the university. **Alicia Gonzalez**, thank you very much for bringing such a positive vibe to the floor and helping me with administrative tasks. **Kai Fiegler**, **Michael Konkowski**, and **Björn Redeker**, thanks for your technical support with designing and manufacturing of the setups. My experiments would never have run without you. **Marc Böke** and **Volker Schulz-von der Gathen**, thanks for always being open to answering questions.

Finishing my thesis would also not have been possible without the friends I have made in Bochum and the colleagues on the floor. **Christoph Stewig**, thanks a lot for introducing me to the lab and our setup. It is always very nice to interact with you. Thanks for all the joking around and the beers. **Dr. Laura Chauvet**, thanks for proof reading my thesis and being my office mate, fruitful discussion partner, and friend. It was always a pleasure to work with you. **Siqi Yu**, thanks for proof reading my thesis and the nice interactions inside and outside the lab. **Soad Mohsenimehr**, and **Fatma-Nur Seferoglu**, thanks for the time in and outside the lab. It was fun

hanging out with you. **Daniel Henze**, thanks for proof reading my thesis, thanks for taking over Laura's desk so that I will never be lonely at the floor, and for the joking around. **Sascha Chur**, thanks for always answering any question I pondered and for the good times after work and during conference trips. The latter naturally holds for the other colleagues as well. **Pia Pottkamper**, with whom I travelled to the FLTPD near Prague. **Jonas Thiel**, thanks for the good time exploring the north-east coast of America.

Before I came to Bochum, I already had the luxury to get a taste on experimenting with plasmas. The people that I met during my master thesis were instrumental in opening the path of doing a PhD and giving a first (very good) example on how science is done. Thanks to **Prof. Dr. Richard Engeln**, **Dr. Maik Budde**, **Dr. Alexander Puth**, **Dr. Antoine Salden**, and **Antoine Post**.

Finally, I am thankful for my friends and family at home. **Papa en mama**, erg bedankt dat jullie me altijd gestimuleerd hebben om te studeren, zonder jullie goede opvoeding was ik hier nooit gekomen. **Ivo**, mijn broertje, je bent natuurlijk ook onmisbaar. Ik wens je nog veel succes met jouw studie. And then we come to **Ayu**, we met in the romantic city of Heidelberg during a conference trip. Thanks a lot with helping me through the most challenging parts of my PhD.

# Curriculum Vitae

Ir. Steijn Cornelis Lambertus Vervloedt

Born on 31 July 1998 in Veldhoven, the Netherlands

## Education

2022–present	<b>PhD in Physics</b> , Ruhr-University Bochum
2020–2022	<b>MSc in Applied Physics</b> , Eindhoven University of Technology
2015–2020	<b>BSc in Applied Physics</b> , Fontys University of Applied Sciences
2010–2015	<b>General Secondary Education</b> , Sint-Joris College, Eindhoven
2002–2010	<b>Primary School</b> , Sint Christoffel School, Waalre

## Professional Experience

2022–present	<b>Doctoral Researcher</b> , Ruhr-University Bochum, Bochum
2022	<b>Research Employee</b> , Eindhoven University of Technology
2019–2021	<b>Technician</b> , Prodrive Technologies B.V., Eindhoven
2018	<b>Software Engineer</b> , SunCycle Technology B.V., Eindhoven

## Publications

- S C L Vervloedt, M Budde, and R Engeln "Influence of oxygen on the ro-vibrational kinetics of a non-equilibrium discharge in CO<sub>2</sub>-O<sub>2</sub> mixtures". *Plasma Sources Science and Technology* **32** 015004 (2023)
- S Yu, S C L Vervloedt, and A von Keudell "Controlled synthesis of NO in an atmospheric pressure plasma by suppressing NO destruction channels by plasma catalysis". *Journal of Physics D: Applied Physics* **57** 245203 (2024)
- S C L Vervloedt and A von Keudell "Ammonia synthesis by plasma catalysis in an atmospheric RF helium plasma". *Plasma Sources Science and Technology* **33** 045005 (2024)
- Antoine Post, Maik Budde, S C L Vervloedt, Richard Engeln, and Tom Huiskamp "Nanosecond repetitively pulsed plasmas with MHz bursts for CO<sub>2</sub> dissociation". *Journal of Physics D: Applied Physics* **57** 305203 (2024)
- Steijn Vervloedt and Achim von Keudell "Nitrogen Oxidation on A Plasma-Exposed Surface". *Plasma Chemistry and Plasma Processing* **45** 1551–1565 (2025)

## Presentations

- **June 2025** - *Surface chemistry at a plasma-surface interface for  $N_2$  fixation*, 26th International Symposium on Plasma Chemistry, Minneapolis (oral)
- **April 2025** - *Surface processes during plasma-based nitrogen fixation*, DPG Spring Meeting, Gottingen (oral)
- **July 2024** - *Investigating  $NH_3$  formation at a plasma exposed-surface*, 6th International Symposium on Plasmas for Catalysis and Energy Materials, Eindhoven (oral)
- **April 2024** - *Ammonia synthesis at a plasma-surface interface*, Frontiers in Low Temperature Plasma Diagnostics XV, Castle Hotel Liblice, Czech Republic (poster)
- **February 2024** - *Ammonia synthesis in an atmospheric catalytic RF plasma*, DPG Spring Meeting, Greifswald (oral)
- **May 2023** -  *$NH_3$  synthesis in a catalytic atmospheric RF discharge*, 25th International Symposium on Plasma Chemistry, Kyoto (poster)
- **April 2023** -  *$NH_3$  synthesis in a catalytic atmospheric pressure RF discharge*, WE-Heraeus-Seminar on Non-Thermal Plasmas for Sustainable Chemistry, Bad Honnef (poster)
- **March 2023** - *Excitation transfer between molecules in transient atmospheric pressure plasmas and its impact on plasma chemistry*, 20th Plasma Technology Conference, Bochum (poster)
- **October 2022** -  *$NH_3$  synthesis in an atmospheric pressure RF discharge*, 25th International Plasma School 'Low Temperature Plasma Physics: Basics and Applications', Bad Honnef (poster)
- **September 2022** - *Influence of oxygen on the ro-vibrational kinetics of a non-equilibrium discharge for  $CO_2$  conversion*, International Symposium Plasma Catalysis for  $CO_2$  recycling, Krakow (oral)